IMAGE: A MAP OF THE STARS OF THE ORION CONSTELLATION

JournalPreview

London Journal of Research in Science: Natural & Formal

Volume 25 | Issue 2 | Compilation 1.0

Great Britain Journals Press

WWW.JOURNALSPRESS.COM

Journal Content
In this Issue

Great Britain Journals Press

The Charge of Electrons from White Dwarf Stars Create the Majority of Black Holes

Ardeshir Irani

ABSTRACT

It was originally believed that only mass could create Black Holes. It is the purpose of this paper to prove that the charge from White Dwarf Stars creates the majority of Black Holes. Stars with mass below 1.44 Solar mass known as the Chandrasekhar Limit create White Dwarf Stars. Using the energy in charge, Energy = $ne^2/(24\pi\epsilon_0 r)$ where n corresponds to the number of electrons, White Dwarfs are responsible for Solar Mass type or smaller Black Holes with charge. Stars bigger than 1.44 Solar Mass create bigger size Black Holes without charge such as those from Neutron Stars or those located at the center of a galaxy using the energy of mass, Energy = mc^2. Since there are more stars smaller in size than the sun, a majority of charged Black Holes are created by White Dwarf Stars. We calculate the size of the Schwarzschild Radius of the White Dwarf as R = $ne^2/(12\ \pi\epsilon_0 m_e c^2)$ where n corresponds to the number of electrons drawn from the White Dwarf and sent into the Black Hole created. Only White Dwarf Stars can create Black Holes with Mass, Angular Momentum, and Charge, albeit these Black Holes will be smaller in size than those created by mass.

Keywords: white dwarf stars, electron degeneracy pressure, charged black holes, Schwarzschild radius, chandrasekhar limit, radius calculations.

Classification: LCC Code: QB843.B55

Language: English

Great Britain Journals Press

LJP Copyright ID: 925611
Print ISSN: 2631-8490
Online ISSN: 2631-8504

London Journal of Research in Science: Natural & Formal

Volume 25 | Issue 2 | Compilation 1.0

The Charge of Electrons from White Dwarf Stars Create the Majority of Black Holes

Ardeshir Irani

ABSTRACT

It was originally believed that only mass could create Black Holes. It is the purpose of this paper to prove that the charge from White Dwarf Stars creates the majority of Black Holes. Stars with mass below 1.44 Solar mass known as the Chandrasekhar Limit create White Dwarf Stars. Using the energy in charge, Energy = $ne^2/(24\pi\epsilon_0 r)$ where n corresponds to the number of electrons, White Dwarfs are responsible for Solar Mass type or smaller Black Holes with charge. Stars bigger than 1.44 Solar Mass create bigger size Black Holes without charge such as those from Neutron Stars or those located at the center of a galaxy using the energy of mass, Energy = mc^2. Since there are more stars smaller in size than the sun, a majority of charged Black Holes are created by White Dwarf Stars. We calculate the size of the Schwarzschild Radius of the White Dwarf as R = $ne^2/(12\ \pi\epsilon_0 m_e c^2)$ where n corresponds to the number of electrons drawn from the White Dwarf and sent into the Black Hole created. Only White Dwarf Stars can create Black Holes with Mass, Angular Momentum, and Charge, albeit these Black Holes will be smaller in size than those created by mass.

Keyterms: white dwarf stars, electron degeneracy pressure, charged black holes, Schwarzschild radius, chandrasekhar limit, radius calculations.

Author: Downey Research Institute, Downey, California, USA.

I. INTRODUCTION

Charge is more effective on a microscopic level while mass is more effective on a macroscopic level. Therefore, charge creates smaller sized Black Holes while mass creates larger sized Black Holes.

E = mc^2 produces bigger Black Holes without charge.

E = $\{q^2/(24\pi\epsilon_0 r)\}x\{\theta\ \phi\ + \gamma^2\theta\ \phi\ + \gamma^2\theta\ + (\gamma^2 - 1)x(\theta\ + \theta\ \phi\ )\}$ which can be written as E = $q^2/(24\pi\epsilon_0 r)$ for γ =1 (Reference 1), produces smaller size charged Black Holes.

The material in a White Dwarf no longer undergoes fusion reactions, so the Star has no source of energy. As a result, it cannot support itself by the heat generated by fusion against gravitational collapse, but it is supported only by electron- degeneracy pressure, causing it to become extremely dense. Physics of degeneracy yields a maximum Mass for a White Dwarf Star, the Chandrasekhar Limit approximately 1.44 times the Mass of the Sun beyond which a White Dwarf Star cannot be created. The charge of electrons from the White Dwarf are responsible for creating all the charged Black Holes. For Black Holes created by the bigger Stars using their mass, the electrons are tied to their individual atoms, and so all the mass: the neutrons, protons and electrons are bound together within the atom, and act as one unit being drawn in by the Black Hole they create, even if the atoms are converted to neutrons, positive ions and electrons by the gravity of the Black Hole. Since there is no net charge in matter, a charged Black Hole cannot be created by the neutral matter of these bigger Stars.

London Journal of Research in Science: Natural & Formal

The inward force due to gravity that is not being cancelled by the outward force of fusion heat energy changes the Carbon-Oxygen (C-O) atoms in the White Dwarf into a plasma of C-O ions and electrons. Since electrons are lighter than the C-O nuclei they accelerate much faster under the gravitational force to reach relativistic velocities. The inward gravitational force pushes the more massive C-O nuclei toward the center of the White Dwarf Star while the electrons bouncing off the heavier material accelerate remaining closer to its outer surface. The energy of the charge of electrons near the surface of a White Dwarf creates space-time curvature around it. The faster electrons located near the surface will enter the curved space-time into the potential well created by the White Dwarf Star. Once their number equals n, the electrons will create a Black Hole of radius R = $n\mathscr{e}^2/(12\ \pi\epsilon_0 m_e c^2)$.

If more Energy (more electrons) from the White Dwarf goes into creating a bigger Black Hole, then the remaining net positive Energy being greater will blow up as a Supernovae. If less Energy (fewer electrons) from the White Dwarf goes into creating a smaller Black Hole, then the remaining net positive Energy being smaller will blow up as a Novae. An explosion is only possible if a Black Hole is created. If not, then the electrons will be drawn back into the White Dwarf by its net positive charge to stabilize the White Dwarf by making its total charge neutral.

R(max) < 4.25 km for the Chandrasekhar Limit of 1.44 Solar Mass and n(max.) < $4.54\text{x}10^{18}$ where n corresponds to the number of electrons drawn in from the White Dwarf to create the Black Hole. Smaller White Dwarf Stars near the Chandrasekhar Limit will create the larger sized Black Holes and larger explosions with R closer to R(max) and n closer to n(max), while larger White Dwarf Stars at the opposite end of the graph will create smaller sized Black Holes and smaller explosions.

The size of the Schwarzschild Radius for charge is given by R(q) = $n\mathscr{e}^2/(12\ \pi\epsilon_0 m_e c^2)$ which is the corresponding equation for mass given by R(M) = $2GM/c^2$ for creating Black Holes. Since E = $ne^2/(24\ \pi\epsilon_0 r)$ for "n" electrons at rest (K.E.=0), the Potential Energy (P.E.) of a White Dwarf will be $ne^2/(24\ \pi\epsilon_0 r)$. From Conservation of Energy $1/2m_e v^2 - ne^2/(24\pi\epsilon_0 r) = 0$ at the location of the Schwarzschild radius, with r = R and v = c, and R(q) = $n\mathscr{e}^2/(12\ \pi\epsilon_0 m_e c^2)$. We use the same method as was used to calculate R for mass M noting that GM has now been replaced by $n\mathscr{e}^2/24\pi\epsilon_0 m_e$.

R(e)/R(m_e) = $6.93\text{x}10^{41}$ for a single electron or for n electrons, and that is the reason the charge of electrons can create Black Holes while the mass of electrons cannot.

Setting R(e) = R(M), $\mathscr{e}^2/(12\ \pi\epsilon_0 m_e c^2) = 2GM/c^2$ and M = $\mathscr{e}^2/(24\ \pi\epsilon_0 G m_e) = k\mathscr{e}^2/6Gm_e = 6.32\text{x}10^{11}$kg. This is mainly due to the big difference in the values of k and G, the constants of electric charge and gravitational mass. The formula above implies that the charge of a single electron, $1.6\text{x}10^{-16}$C, is equivalent to a mass of $6.32\text{x}10^{11}$kg to create a Black Hole of the same Schwarzschild Radius R. Hence the charge of electrons in the White Dwarf Star are clearly superior to the mass of electrons at creating Black Holes. This is the same reason that on a microscopic level charge dominates over mass since F(charge)/F(gravity) = $2\text{x}10^{39}$ for the force exerted between a proton and an electron due to its dependence on k/G.

Most Stars end their lives as White Dwarfs (Reference 3). Hence most Black Holes from White Dwarfs that are created with charge are plentiful. All Solar Masses beyond the Chandrasekhar Limit will create

Neutron Stars and neutral Black Holes with only Mass and Angular Momentum, but these are in a minority since there exist more stars with mass less than the sun than greater than the sun.

Graph of radius–mass relations for a model White Dwarf (Reference 2).

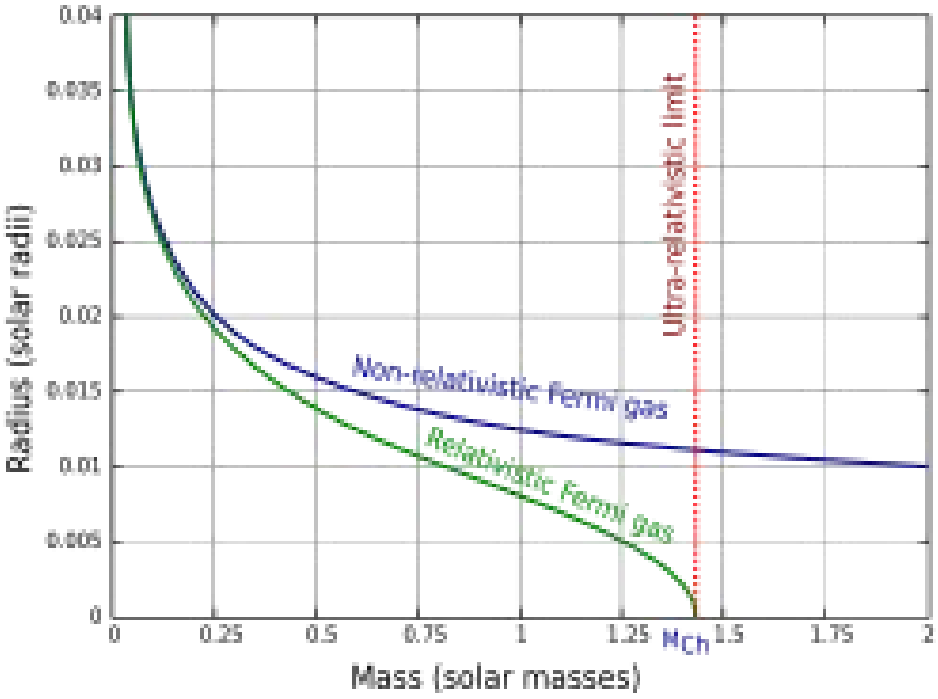

Case 1: At the Chandrase*From the Graph:*

khar Limit, the radius of the White Dwarf Star is 0 and therefore it cannot create a Black Hole. R(max) < 4.25 km and n(max.) < 4.54×10^{18}.

Case 2: A White Dwarf size of 1.25 (Solar Mass) = 0.005 (Solar Radius) = 3.5×10^{6}m, Density = 1.39×10^{12} kg/m^3, R = 3.69 km, n = 3.94×10^{18}.

Case 3: The majority of White Dwarfs have a size of 0.6 (Solar Mass) = 0.0125 (Solar Radius) = 8.7×10^{6} m for the Relativistic Fermi gas case. Density = 4.18×10^{8} kg/m^3, R = 1.77 km, n = 1.89×10^{18}.

Case 4: A White Dwarf size of 0.125 (Solar Mass) = 0.025 (Solar Radius) = 1.75×10^{7}m, Density = 1.11×10^{7} kg/m^3, R = 369 m, n = 3.94×10^{17}.

Case 5: In the extreme situation, a White Dwarf size of 0.04 (Solar Mass) = 0.04 (Solar Radius) = 2.8×10^{7}m, Density = 8.66×10^{5} kg/m^3, R = 118 m, n = 1.26×10^{17}.

The three stages of creating a Black Hole that are portals to the fourth spatial dimension are:

Through a White Dwarf's charge to create the smallest sized Black Holes with mass, angular momentum, and charge.

Through a Neutron Star's mass between 1.44 and 5 Solar Masses to create medium sized Black Holes with mass and angular momentum. Neutron Stars have a radius of 4.25 km at the lower end and about 15 km at the larger end beyond which the Neutron Star will turn into a Black Hole.

Directly through the mass of Stars bigger than 5 Solar Masses with a radius R between 15 km and 2.95x 10^{11}km (100 billion Solar Mass Black Hole known as Phoenix A) to create the largest known size Black Hole with mass and angular momentum.

II. CONCLUSION

While it takes the Sun's Mass of 1.99x10^{30}kg to create a Black Hole with R = 2.95 km, it takes the charge of 3.15x10^{18} electrons or 0.5 Coulombs (mass 2.87x10^{-12} kg of electrons) from a White Dwarf to create the same size Black Hole of R = 2.95 km. It is not the Sun's mass but rather the charge of the White Dwarf electrons that creates the Black Hole of this size. Hence our Sun must go through the stages of becoming a Red Giant and then a White Dwarf before it can become a Black Hole.

Energy in charge will always dominate Black Hole creation over Energy in mass unless the Star is larger as in the case of Stars above the Chandrasekhar Limit of 1.44 Solar Masses. These larger stars do not become White Dwarf Stars but rather they become Neutron Stars or bigger sized Black Holes.

APPENDIX

Radius Calculations:

Starting with the radius of the electron = 4.68x10^{-16}m (Reference 4) and the radius of the electron neutrino = 2x 10^{-21}m (Reference 5) and the mass of the electron = 0.511 MeV/$c^2$and the mass of the electron neutrino = 2.2 eV/c^2 from the Standard Model of Particle Physics, we see that the ratio of their radius is equal to the ratio of their masses. $r_e/r_{\nu_e} = m_e/m_{\nu_e}$ = 4.68x10^{-16}/2x10^{-21} = 0.511x10^6/2.2 = 2.3x10^5. We use this equality ratio of the radius and mass to calculate the radius of the proton, the neutron, and the Up and Down Quarks.

For the Proton: $r_p/r_e = m_p/m_e$, r_p = (938.27/0.511) x 4.68x10^{-16} = 8.593x10^{-13}m 8.59x10^{-13}m.

For the Neutron: $r_n/r_e = m_n/m_e$, r_n = (939.57/0.511) x 4.68x10^{-16} = 8.605x10^{-13}m 8.61x10^{-13}m.

For the Up Quark: $r_{Up}/r_e = m_{Up}/m_e$, r_{Up} = (2.3/0.511) x 4.68x10^{-16} = 2.1x10^{-15}m.

For the Down Quark: $r_{Down}/r_e = m_{Down}/m_e$, r_{Down} = (4.8/0.511) x 4.68x10^{-16} = 4.4x10^{-15}m.

Using this same ratio of radius to mass, the radius of the Carbon nucleus would be 1.02x10^{-11}m and its Density would be 4.51x10^6 kg/m^3. The Densities of all stable nuclei from Hydrogen to Lead varies from 6.30x10^8 kg/m^3 to 1.51x10^4 kg/m^3 (Reference 6) which clearly contradicts what exists in Physics College Books that all Nuclei have the same Density of 2.3x10^{17} kg/m^3 (Reference 7) based on the wrong assumption that the radius of most nuclei is proportional to $A^{\frac{1}{3}}$ where A is their Mass Number.

REFERENCE

1. Irani, A. (2021) Matter-Antimatter Annihilation. Journal of High Energy Physics, Gravitation and Cosmology, 7, 474-477. https://doi.org/10.4236/jhepgc.2021.72027
2. From the Internet: Wikipedia.com; White Dwarf Star: Mass-Radius Relationship.

3. Bradley Carroll and Dale Ostlie, An Introduction to Modern Astrophysics, Page 572, Cambridge University Press (2017), University of Cambridge.
4. Irani, A. (2024) Calculations of the Electron Radius. Journal of High Energy Physics, Gravitation and Cosmology, 10, 724-725. doi: 10.4236/jhepgc.2024.102044.
5. Irani, A. (2024) Estimates of the Charges and Size of the Three Types of Neutrinos. *Journal of High Energy Physics, Gravitation and Cosmology*, **10**, 1467-1469. doi: 10.4236/jhepgc.2024.104082.
6. Irani, A. (2024) Unpublished Report on the Radius and Density of Nuclei of the Periodic Table.
7. Serway & Faughn, College Physics, Fifth Edition, Page 960, Harcourt College Publishers, Orlando, FL 32887-6777.

This page is intentionally left blank

Cellular Generation Number as an Invariant Measure of Biological Time in Relativistic Systems: Biological Systems do Not Experience Time Dilation

Domenico Maglione

ABSTRACT

This work presents a thought experiment where the number of cellular duplications or generations (G) is used as a biological clock to investigate the effects of relativistic environments on biological time. We demonstrate that, although physical clocks in different reference systems measure varying times due to relativistic time dilation, biological time remains invariant and corresponds to the 'proper' time. This invariance holds not only across inertial reference frames but also extends to non-inertial, accelerated, and gravitational reference systems. The invariance arises because G is defined as the ratio of the growth time to the duplication time, ensuring that any relativistic effects influencing these time intervals cancel out.

These findings challenge the classic interpretation of Einstein's twin paradox, which suggests differential ageing due to relativistic velocities. In reality, while physical clocks indicate differing times, biological time, and thus the biological age of living organisms, remains unaffected, aligning consistently with the proper time.

Keywords: biological time, biological clock, time dilation, relativistic effects, proper time, invariant ageing, twin paradox.

Classification: LCC Code: QA274

Language: English

Great Britain Journals Press

LJP Copyright ID: 925612
Print ISSN: 2631-8490
Online ISSN: 2631-8504

London Journal of Research in Science: Natural & Formal

Volume 25 | Issue 2 | Compilation 1.0

Cellular Generation Number as an Invariant Measure of Biological Time in Relativistic Systems: Biological Systems do Not Experience Time Dilation

Domenico Maglione

ABSTRACT

This work presents a thought experiment where the number of cellular duplications or generations (G) is used as a biological clock to investigate the effects of relativistic environments on biological time. We demonstrate that, although physical clocks in different reference systems measure varying times due to relativistic time dilation, biological time remains invariant and corresponds to the 'proper' time. This invariance holds not only across inertial reference frames but also extends to non-inertial, accelerated, and gravitational reference systems. The invariance arises because G is defined as the ratio of the growth time to the duplication time, ensuring that any relativistic effects influencing these time intervals cancel out.

These findings challenge the classic interpretation of Einstein's twin paradox, which suggests differential ageing due to relativistic velocities. In reality, while physical clocks indicate differing times, biological time, and thus the biological age of living organisms, remains unaffected, aligning consistently with the proper time. Although bacterial cultures were used as a model in this study, the results are generalisable to all cellular systems, provided identical growth conditions are maintained. This study provides new insights into the interplay between biological processes and relativistic effects, establishing G as a reliable and invariant measure of biological time across all reference frames.

Keywords: biological time, biological clock, time dilation, relativistic effects, proper time, invariant ageing, twin paradox.

Author: Independent Researcher, Former Postdoctoral Fellow at the Institute of Genetics and Biophysics Adriano Buzzati-Traverso, Naples, Italy.

I. INTRODUCTION

In special relativity, 'proper' time refers to the time interval measured by a clock moving alongside an object, effectively at rest relative to the events being timed. This measurement remains invariant across all inertial reference frames. According to relativity, time appears to slow down for objects moving at relativistic speeds, a phenomenon experimentally confirmed for subatomic particles such as muons. When muons are produced in the upper atmosphere by cosmic ray interactions, they travel toward the Earth's surface at speeds approaching that of light. Due to their short half-life, one would expect that very few of them would reach the Earth's surface. However, observations indicate a significant number of muons reaching sea level, a result explained by relativistic time dilation affecting muons travelling at relativistic velocities.

London Journal of Research in Science: Natural & Formal

The proper time of the muons, measured in their rest frame, remains constant. However, in the Earth's rest frame, the time is dilated due to their high speed. In atmospheric muons, this effect allows them to travel greater distances before they decay, as shown by Rossi and Hall (1941). Similarly, in a controlled synchrotron environment, time dilation significantly extends the apparent lifetime of muons, as demonstrated by Bailey et al. (1977). More recently, Botermann et al. (2014) have confirmed relativistic time dilation in lithium-ion beams, providing further evidence for this fundamental prediction of Einstein's theory.

Whereas relativity has had a significant impact on many areas of physics and technology, there remains a notable gap in the scientific literature regarding both experimental and theoretical studies on biological clocks about relativistic effects. Recent studies, such as Maestrini et al. (2018) and Ajdžanović, V.Z. et al. (2023), have examined ageing through concepts loosely inspired by relativity, such as notions of time dilation and contraction. However, these models do not involve systems at relativistic speeds or accelerations in the physical sense (m/s²). Instead, they focus on biological ageing rates affected by pathological conditions like cancer and chronic inflammation. In this context, 'acceleration' is used metaphorically, referring to biological factors speeding cellular deterioration. Such processes compress what can be seen as 'biological time', leading to faster ageing but without any connection to actual relativistic velocities or physical accelerations.

In this study, we use bacterial growth as a 'biological clock' to demonstrate that biological time, represented by the number of bacterial generations (G), is invariant across all inertial frames. Thus, G is a biological timekeeper independent of relativistic time dilation.

To further explain why G better represents biological aging, consider a simple example: two cultures of the same bacterial species, grown under different experimental conditions such that one has an average doubling time of 1 hour, while the other has an average doubling time of 0.5 hours. After 2 hours of growth, both have experienced the same elapsed physical time. However, in biological terms, the first culture has $G_1 = \frac{2\,h}{1h} = 2$, while the second has $G_2 = \frac{2\,h}{0.5\,h} = 4$. This means that the second culture, in the same 2-hour growth period, has biologically aged more than the first. Although simplistic, this example clearly indicates why G is a better measure of biological aging: it reflects the generational progression, which directly correlates with the biological processes underlying aging.

This study proposes a thought experiment with two identical bacterial cultures: one situated on Earth (System T) and the other onboard a spacecraft moving at relativistic speed v relative to Earth (System A). All culture conditions, such as temperature, nutrient medium composition, and oxygenation, are kept the same in both systems. This setup allows us to isolate the effects of proper time on biological growth, helping to validate the invariance of G as a measure of biological time across inertial systems.

The twin paradox describes a scenario where one twin remains on Earth while the other travels at relativistic speed and later returns. According to special relativity, each twin observes the other's clock running slower due to time dilation. This symmetry creates a paradox: each twin observes the other aging more slowly relative to themselves.

The resolution of the paradox is that the travelling twin undergoes phases of acceleration and deceleration during their journey, which disrupt the symmetry of the situation. These phases involve transitions between inertial reference frames, distinguishing the travelling twin from the one who remains on Earth. As a result, the travelling twin experiences less elapsed time throughout of the journey, consistent with the predictions of relativity.

In this study, we intentionally exclude the acceleration and deceleration phases of the travelling twin's journey to focus exclusively on inertial systems. This approach allows us to analyse the effects of

relativistic time dilation on biological processes in a simplified context, isolating its impact within purely inertial frames.

The anticipated result of this thought experiment is that biological time, as measured by the number of bacterial generations (*G*), remains invariant in both reference frames despite the relativistic effects observed in physical clocks. Moreover, this invariance is not limited to inertial reference frames; it also applies to non-inertial systems, including those that are uniformly accelerated or within gravitational fields. This invariance occurs because biological time is represented by G, which is defined as the ratio of the growth time to the duplication time. Any relativistic effects, mathematically represented by the relativistic gamma factor, influence these two time intervals equally and cancel each other out. This ensures that G remains invariant across all reference frames (see Chapter 3.2).

Therefore, in the famous twin paradox (Einstein, 1905), while the times measured by physical clock on Earth and on the spacecraft differ, the biological ages of the two twins remain the same.

II. RESULTS

In biological formulas, used to describe population growth or similar processes, such as the logistic equation, it is typically unnecessary to distinguish between proper time and relative time, as these formulas generally refer to a stationary reference frame (commonly the "laboratory" frame or, more broadly, the "Earth" frame). However, in this study, we address relativistic effects. Therefore, throughout the manuscript, we will explicitly specify whether we are referring to "proper time" or "relative time" whenever such distinctions are relevant.

2.1 Invariance of Bacterial Duplication Number Across Inertial Reference Frames

The number of bacterial duplications or generations *G* is invariant across all inertial reference frames, as it is measured relative to the proper time of the respective system. Thus, the number of duplications *G* is a consistent measure of biological time progression independent of the reference frame. In other words, if we determine the number of duplications under specific and same culture conditions on Earth or on spacecraft travelling at a relativistic velocity v, we will use a clock synchronized with the system in which the study is conducted (either on Earth or aboard the spacecraft), which will measure the proper time. Consequently, the number of duplications will be identical in both systems, provided that growth conditions are the same. This means that the bacterial duplication number is 'invariant' with respect to any inertial reference frame. Such invariance highlights the consistency of biological processes across different contexts. From this follows that biological time, represented by the number of generations *G*, does not depend on the relativistic effects experienced by physical measuring instruments, as we will demonstrate later.

The following section details the experimental setup and calculations designed to test the invariance of G across inertial frames.

2.2 Description of the Thought Experiment and Calculations

In special relativity, proper time τ (measured within the reference system) and relative time t (measured by an observer external to the moving system) are related by the formula:

$$t = \tau \cdot \gamma_{inertial} = \frac{\tau}{\sqrt{1-\frac{v^2}{c^2}}} \quad (1)$$

Where t represents the relative time measured by an observer moving at velocity v relative to the object, τ is the proper time experienced by the object, c is the speed of light in vacuum and $\gamma_{inertial}$ is described in the section named "A*bbreviations and Glossary*".
The thought experiment is designed as follows:

- *System T (on Earth):* A bacterial culture grows with a doubling or generation time equal to τ hours of proper time.

- *System A (on a spacecraft moving at speed v relative to Earth):* An identical Earth bacterial culture grows at the same doubling rate τ, measured with respect to the spacecraft's proper time. To ensure identical conditions in both experiments, the spacecraft laboratory simulates an acceleration equivalent to Earth's gravity ($1g$), eliminating potential variations in bacterial growth due to differing gravitational forces. This setup controls for both the relativistic and the biochemical effects of gravity on bacterial growth.

Furthermore, to avoid growth differences due to acceleration as the spacecraft reaches velocity v:

- The experiment starts once the spacecraft reaches a constant velocity v.
- It is conducted entirely at this constant relativistic speed (v).

The experiment duration, denoted as the growth period τ_{growth}, is identical in both systems and measured as proper time within each system. At the end of this growth period τ_{growth}, the cultures are frozen to preserve the bacterial count and prevent further division. This allows for a direct comparison based solely on each system's proper time.

2.2.1 System on Earth as Observed from the Spacecraft's Reference Frame (System A)

For an observer on the spacecraft, the proper time τ_{growth} on Earth becomes:

$$t'_{growth} = \frac{\tau_{growth}}{\sqrt{1-\frac{v^2}{c^2}}} \tag{2}$$

Where t'_{growth} is the relative growth time measured with respect to the spacecraft reference frame, and τ_{growth} represents the proper time duration of the experiment, which is the same for both systems.
From the spacecraft perspective, the relativistic doubling time of the bacterial culture on Earth is as follows:

$$t' = \frac{\tau}{\sqrt{1-\frac{v^2}{c^2}}} \tag{3}$$

Where t' is the relative duplication time measured with respect to the spacecraft reference frame, and τ denotes the proper time in which the bacteria double in number, which is also equal for both systems.

Over a period observed on Earth, the number of bacterial generations (G) is given by:

$$G' = \frac{t'_{growth}}{t'} = \frac{\tau_{growth} \cdot \sqrt{1-\frac{v^2}{c^2}}}{\tau \cdot \sqrt{1-\frac{v^2}{c^2}}} = \frac{\tau_{growth}}{\tau} \tag{4}$$

Consequently, an observer on the spacecraft will see that the bacteria on Earth double exactly $\frac{\tau_{growth}}{\tau}$ times.

2.2.2 System on the spacecraft as seen from Earth (System T)

For the observer on Earth, the proper time τ_{growth} in the spacecraft corresponds to the following:

$$t_{growth} = \frac{\tau_{growth}}{\sqrt{1-\frac{v^2}{c^2}}} \tag{5}$$

From the terrestrial perspective, the relative doubling time of the bacterial culture in the spacecraft becomes:

$$t = \frac{\tau}{\sqrt{1-\frac{v^2}{c^2}}} \tag{6}$$

During this relative time, the number of bacterial generations (G) is given by:

$$G = \frac{t_{growth}}{t} = \frac{\tau_{growth}}{\sqrt{1-\frac{v^2}{c^2}}} \bullet \frac{\sqrt{1-\frac{v^2}{c^2}}}{\tau} = \frac{\tau_{growth}}{\tau} \tag{7}$$

Thus, the observer on Earth finds that the bacterial generation number is $G = \frac{\tau_{growth}}{\tau}$, identical to that of the culture on the spacecraft (see Eq. 4).
In fact:

$$G = G' = \frac{\tau_{growth}}{\tau} \tag{8}$$

This result is highly significant, demonstrating that the bacterial generation number G, under identical culture conditions, remains invariant across all inertial reference frames. Consequently, G is a reliable measure of biological time, consistently corresponding to the proper time of the reference system, regardless of the time dilation observed between different systems.

2.2.3 Freezing and Final Result Using an Exponential or Logistic Growth Model

At the end of the growth period τ_{growth} in each system, the cultures are frozen to prevent further bacterial divisions and preserve the final count. Assuming an exponential growth model, the final number of bacteria is given by:

$$N_{final} = N_0 \bullet 2^{\frac{\tau_{growth}}{\tau}} \tag{9}$$

Where N_0 is the initial number of bacteria.

The final count remains identical in both systems, as the observed number of doublings ($G = \frac{\tau_{growth}}{\tau}$) are invariant with respect to the proper time. Freezing preserves this count, enabling an accurate comparison between the two systems without the influence of the spacecraft's deceleration. The identical count confirms that the biological time elapsed for the two cultures is the same, as indicated by G, which serves as the true measure of biological time.

Even when employing a different growth model, such as a more realistic logistic model, the final count remains identical in both systems, as well as the general equation for G remaining unchanged (see Appendix A) .

We derive below the logistic growth equation in a relativistic context, showing that the final bacterial count remains invariant across inertial reference frames. Starting with the general logistic equation, we introduce relativistic modifications to the growth rate r and the elapsed time t, highlighting their relationship to the relativistic factor γ.

The logistic growth equation describing population dynamics in environments with limited resources was proposed by Verhulst. It is the following:

$$N_t = \frac{K}{1+\left(\frac{K-N_0}{N_0}\right)e^{-rt}} \tag{10}$$

Where N_0 is the initial population size, N_t is the population size at time t, K represents the carrying capacity of the environment (maximum sustainable population), r indicates the growth rate measured in units of $time^{-1}$ and t, the elapsed time, corresponds to t_{growth}.

This equation captures the balance between exponential growth during the early phase and the eventual stabilisation of the population as it approaches the carrying capacity K. In a relativistic framework, both the elapsed time t and the growth rate r are affected by time dilation, which varies depending on the relative velocity between the observer and the growing system. The proper growth t_{growth}, measured in the inertial frame of the bacteria, appears dilated to an external observer, and can be expressed as below (see also Eq.5):

$$t_{growth} = \tau_{growth} \cdot \gamma = \frac{\tau_{growth}}{\sqrt{1-\frac{v^2}{c^2}}} \tag{11}$$

Since r is defined as the inverse of time (see legend of Eq.10) it must also be treated in relativistic terms, therefore we have:

$$r = \frac{r_{proper}}{\gamma} = \frac{r_{proper}}{\frac{1}{\sqrt{1-\frac{v^2}{c^2}}}} = r_{proper} \bullet \sqrt{1-\frac{v^2}{c^2}} \tag{12}$$

Where r_{proper} is the growth rate r measured in the inertial frame at rest relative to the growing population, and γ indicates $\gamma_{inertial}$.

Substituting these relativistic forms of t (Eq.11) and r (Eq.12) into the logistic growth equation above, we obtain:

$$N_t = \frac{K}{1+\left(\frac{K-N_0}{N_0}\right)\bullet e^{-\left(\frac{r_{proper}}{\gamma}\cdot \tau_{growth}\cdot\gamma\right)}}$$

Simplifying further, the relativistic factors cancel γ out, leaving:

$$N_t = \frac{K}{1+\left(\frac{K-N_0}{N_0}\right)e^{-\left(r_{proper}\bullet\tau_{growth}\right)}} \tag{13}$$

Equation 13 clearly demonstrates that, under identical environmental and cultivation conditions, the final bacterial count depends only on the proper growth parameters r_{proper} and τ_{growth}, which are measured in the inertial frame of the population. Therefore, the final bacterial count is invariant across frames. This result highlights that, even in relativistic contexts, the population size at the end of the growth period remains the same for all observers, reinforcing the conclusion that, even in more realistic growth models such as the logistic model, biological time remains unaffected by time dilation, and therefore, the two cultures age by the same amount.

Clearly, any bacterial or cellular culture undergoing logistic growth can be considered a biological clock only during its exponential phase. This is because, in the terminal growth phase, bacteria essentially cease to replicate. Consequently, *G*, the number of generations in this phase, tends to zero as the proper doubling time (τ) approaches infinity. Specifically:

$$\lim_{\tau\to\infty}\left(G = \frac{\tau_{growth}}{\tau}\right) = 0$$

2.3 Numerical Examples Using Exponential Growth Model

Consider an example with 1,000 initial bacteria (N_0) for both cultures, a proper growth time τ_{growth} of 2 hours, a mean doubling time of τ equal to 0.5 hours, and a spacecraft travelling at a velocity of 0.9*c*. Using the formula for relativistic time dilation, both the growth time and duplication time are found to be dilated relative to the other reference frame.

2.3.1 Numerical Example Exponential Model: System on the Spacecraft as Seen from Earth (System T)

For an observer on Earth, the proper growth time $\tau_{growth} = 2\ hours$ on the spacecraft appears dilated by an amount calculable using Eq.5:

$$t_{growth} = \frac{\tau_{growth}}{\sqrt{1-\frac{v^2}{c^2}}} = \frac{2}{\sqrt{1-0.9^2}} \cong 4.588\ hours \tag{14}$$

Using Eq.6, we can determine the doubling time of the culture on the spacecraft as observed from Earth:

$$t = \frac{\tau}{\sqrt{1-\frac{v^2}{c^2}}} = \frac{0.5}{\sqrt{1-0.9^2}} \cong 1.147\ hours \tag{15}$$

During this growth period (4.588 hours, Eq.14), and based on the generation number calculated using Eq.15 (1.147 hours), we can determine how many times the bacteria on the spacecraft double:

$$G = \frac{t_{growth}}{t} = \frac{4.588}{1.147} = 4\ times \tag{16}$$

Thus, the observer on Earth observes that the bacteria on the spacecraft double four times during the course of the experiment.

2.3.2.Numerical Example: System on Earth as Seen from the Spacecraft (System A)

Below, we repeat the same calculations as before, but from the perspective of the spacecraft.

For an observer on the spacecraft, the proper growth time $\tau_{growth} = 2\ hours$ on Earth can be calculated using Equation 2:

$$t'_{growth} = \frac{\tau_{growth}}{\sqrt{1-\frac{v^2}{c^2}}} = \frac{2}{\sqrt{1-0.9^2}} \cong 4.588\ hours \tag{17}$$

Using Eq.3, we can determine the doubling time of the culture on Earth as observed from the spacecraft:

$$t' = \frac{\tau}{\sqrt{1-\frac{v^2}{c^2}}} = \frac{0.5}{\sqrt{1-0.9^2}} \cong 1.147\ hours \tag{18}$$

Thus, the observer in the spacecraft sees that the bacteria on Earth double exactly in:

$$G' = \frac{t'_{growth}}{t'} = \frac{4.588}{1.147} = 4\ times \tag{19}$$

Thus, the bacteria on the spacecraft double precisely 4 times, identical to the doubling observed in the Earth culture.

The final bacterial count in each system is then calculated using Eq.9, based on the identical result from Eq.16 and Eq.19, confirming four doublings.

$$N_{final} = N_0 \bullet 2^{\frac{\tau_{growth}}{\tau}} = 1,000 \cdot 2^4 = 16,000 \tag{20}$$

Consequently, both the total bacterial count and the bacterial generation number G remain the same in the two inertial reference frames considered. This indicates that, unlike relative time, the elapsed biological time measured by G remains unchanged across both systems. In other words, the two cultures have 'aged' by the same amount.

Based on the numerical example, here is a table showing the data for proper and relative times in the two systems (Earth and spacecraft) for bacterial growth rates.

Table 1: Example of the Invariance of Bacterial Generation Number (G) Across Inertial Reference Frames Using an Exponential Growth Model.

System	Proper Growth Time (τ_{growth})	Relative Growth Time (t_{growth})	Proper Doubling Time (τ)	Relative Doubling Time (t)	Generations Number (G)	Final Number of Bacteria
Spacecraft (v = 0.9c)	2 hours	4.588 hours	0.5 hours	1.147 hours	4	16,000
Earth	2 hours	4.588 hours	0.5 hours	1.147 hours	4	16,000

2.4 Numerical Example Using Logistic Growth Model

As demonstrated earlier, the equation describing the logistic growth model results invariant across all inertial reference frames. This invariance ensures that the final bacterial count is the same for any observer, regardless of their frame of reference.

In this section, we provide a numerical example to calculate the number of bacteria resulting after 2 hours of proper growth time. The calculation is performed using the previously derived logistic equation (Eq.13). For this example, we will use the following parameters:

- Carrying capacity: $K = 10^9$
- Initial population: $N_0 = 1,000$
- Proper growth rate: $r_{proper} = 1.39\ hours^{-1}$
- Proper growth time: $\tau_{growth} = 2\ hours$

From which we have:

- $r_{proper} \bullet \tau_{growth} = 1.39 \cdot 2 = 2.78$

Based on these values, we calculate that in every reference frame considered, the final number of bacteria is approximately 16,199. In fact:

$$N_{final} = \frac{K}{1+\left(\frac{K-N_0}{N_0}\right)e^{-\left(r_{proper}\bullet\tau_{growth}\right)}} = \frac{10^9}{1+\left(\frac{10^9-1000}{1000}\right)e^{-2.78}} \cong 16,119$$

This value is practically the same as that obtained with the exponential model, indicating that in both cases, using the parameters above, the bacteria are in the exponential growth phase.

III. DISCUSSION

This thought experiment shows that, although physical clocks in different inertial systems measure different times due to relativistic time dilation, biological time, indicated by the bacterial generation number *G*, remains invariant and corresponds to the 'proper' time. The bacterial generation number G is identical in the two inertial frames considered here and remains constant across any other inertial frame.

In this study, we used bacteria. However, the same results would be obtained using any other microorganism or eukaryotic cells in culture, as long as the growth conditions are the same in both inertial systems.

The bacterial culture, through the number of generations *G*, represents a true "biological clock" that is invariant and capable of measuring biological aging. As previously illustrated, we have already presented an example demonstrating this principle. Here, we propose a similar example, but with different numerical values, to reinforce the fundamental idea that G serves as a universal biological measure of aging. Let us consider, for example, two bacterial cultures, A and B, of the same species but grown under different conditions. In culture A, the bacteria have a mean duplication time of 0.5 hours, while in culture B, the mean duplication time is 1 hour. Both cultures are allowed to grow for a total of 10 hours, measured by a physical clock.

Calculating the number of generations *G* for each culture, we obtain:

- For culture A: $G_{(A)} = 10/0.5 = 20$ generations.

- For culture B: $G_{(B)} = 10/1 = 10$ generations.

Although 10 hours of physical clock time have passed for both cultures, culture A is biologically twice as "old" as culture B since it has undergone twice the number of generations.

This example clearly highlights that biological time, as measured by the biological clock *G*, is not directly correlated to the time measured by physical clocks and is, in fact, what quantifies biological aging. For these reasons, the same principle can be applied to more complex organisms, such as humans. In conclusion, while physical clocks are subject to relativistic time dilation, biological aging, as measured by the biological clock *G*, remains invariant for all living organisms, including the most complex ones, such as humans, confirming its universal nature and independence from the chosen reference frame.

Another fundamental measure of biological aging in eukaryotic cells, including higher organisms, is telomere shortening, which occurs with each cell division and is widely recognized as a marker of physiological aging, the natural aging process independent of pathological conditions (Oeseburg et al., 2010; Vaiserman, A., & Krasnienkov, D., 2021).

Since telomere length is directly linked to the number of cell divisions, it follows that telomere shortening is inherently proportional to the number of generations *G*. This further confirms that it is not just an abstract measure but a fundamental biological clock that tracks the passage of biological time.

If *G* remains invariant across reference frames, then telomere shortening, being directly dependent on *G*, must also be invariant. This strengthens the argument that biological time, as measured by *G*, progresses independently of relativistic time dilation. Given that telomere shortening is a well-established marker of aging in eukaryotic cells, this relationship reinforces the validity of using *G* as a universal measure of biological time.

This result revisits the classic interpretation of Einstein's twin paradox, which posits that the twin travelling at relativistic speeds ages more slowly compared to the twin who remains on Earth, as indicated by physical clocks. In reality, both twins would have the same biological ageing at the end of their journeys despite the differing times displayed by the physical clocks in the two systems. Thus, biological time aligns with the proper time of each system and remains unaffected by the relativistic time dilation impacting physical measuring devices.

3.1 Deriving the Time Dilation Equation in a Centrifuge with Radius "r" and Acceleration "a"

In this chapter, we derive the equation for the time dilation experienced by an object in a rotating system, specifically within an ultracentrifuge. The premise for this derivation is that, according to the equivalence principle of general relativity, an acceleration causes time dilation that is the same as that produced by an equivalent gravitational field (Misner, Thorne, & Wheeler, 1973, Chapter 16). Therefore, a time dilation effect should manifest due to the strong centripetal accelerations generated during the operation of these ultracentrifuges. For the following derivation, we will use Newtonian gravitational formulas, as they are more than sufficient for our analysis.
We start with the equation for time dilation in a gravitational field:

$$t = \tau \cdot \gamma_{gravitational} = \frac{\tau}{\sqrt{1-\frac{2KM}{rc^2}}} \tag{21}$$

Where t is the time measured by an observer far from the mass, τ is the proper time measured in proximity to the mass, K is the universal gravitational constant, M is the mass of the body generating the gravitational field, r is the distance from the centre of the mass, and c is the speed of light in a vacuum.

According to the equivalence principle, a gravitational field is equivalent to a uniformly accelerated system. In other words, a uniformly accelerating system replicates the effects of a gravitational field. Therefore, we can transform the term $\frac{KM}{r^2}$ into terms of acceleration.

Newton's law of universal gravitation states that the gravitational force between two objects of masses M and m, separated by a distance r, is given by the following equation:

$$F = \frac{KMm}{r^2} \tag{22}$$

According to Newton's second law, the force can also be expressed as:

$$F = ma \tag{23}$$

where a is acceleration.
Equating the two previous expressions (Eq.22 and 23) for force F, we obtain:

$$ma = \frac{KMm}{r^2} \tag{24}$$

By eliminating m from both sides, we find the acceleration a:

$$a = \frac{KM}{r^2} \Rightarrow \frac{KM}{r} = ar \tag{25}$$

Substituting $\frac{KM}{r}$ of eq.25 into equation 21 allows us to rewrite the gravitational time dilation t in terms of acceleration, obtaining:

$$t = \frac{\tau}{\sqrt{1-\frac{2ar}{c^2}}} \tag{26}$$

From Eq.26, we determine the time dilation factor $\left(\frac{t}{\tau}\right)$ due to centripetal acceleration over a distance r.

$$\frac{t}{\tau} = \frac{1}{\sqrt{1-\frac{2ar}{c^2}}} \tag{27}$$

If $\frac{t}{\tau} = 1$, there is no time dilation, and time flows the same way in both systems.

If $\frac{t}{\tau} > 1$, it means that for an external observer, time appears 'dilated' or flows more slowly in the accelerated system.

While the thought experiment previously described demonstrates, at least theoretically, the invariance of biological time in inertial systems, it is also essential to explore how biological processes might behave in relativistic accelerated or gravitational systems.

Studies indicate that microorganisms exposed to accelerations of thousands of g experience significant biological alterations in growth compared to cultures maintained under non-accelerated conditions. Notably, a study has examined the resilience of prokaryotic life under extreme gravitational forces,

revealing surprising findings regarding their ability to grow and survive even under conditions vastly exceeding Earth's gravity. Deguchi et al. (2011) investigated the growth patterns of various microorganisms, such as *Escherichia coli*, *Paracoccus denitrificans*, and *Shewanella amazonensis*, under hyper accelerative conditions in centrifuges, reaching accelerations as high as 403,627 × *g*.

At 403,627 × *g*, *E. coli* shows highly suppressed growth after 60 hours of incubation, while *Paracoccus denitrificans* exhibits significantly slowed growth, although cell proliferation continues under these extreme conditions.
To reach 403,627 × *g*, the authors reported using a Beckman XL-80 ultracentrifuge (Deguchi et al., 2011). One of the rotors capable of achieving these accelerations is the *Type 90 Ti*, which has a maximum radius of 7.6 cm.

Using Eq.27, we calculate the extent of the time dilation observed relative to the bacteria under these accelerations.

$$\frac{t}{\tau} = \frac{1}{\sqrt{1-\frac{2a \bullet r}{c^2}}} = 1.000\ 0000000033436 \tag{28}$$

This result suggests that the effects of time dilation at these high accelerations are negligible for biological processes; therefore, the significant differences in growth observed by Deguchi et al. (2011) cannot be attributed to relativistic effects. However, due to the profound biological effects caused by the strong accelerations required to observe relativistic effects, the type of experiment proposed in this study may not be feasible for investigating potential relativistic effects on biological time in non-inertial systems.

3.2 Invariance of Bacterial Duplication Number in Non-Inertial Reference Frames

As previously noted, studying the potential relativistic effects on biological time in non-inertial systems is experimentally challenging. However, in this chapter, we demonstrate mathematically that biological time, measured through *G*, remains invariant even in non-inertial reference frames, such as gravitational and uniformly accelerated systems.

G is defined as the ratio of the proper growth time to the proper duplication time. In relativistic reference frames, both inertial and non-inertial, these two times can undergo an identical dilation equal to the gamma factor. Consequently, the relativistic gamma factor mathematically cancels out, rendering *G*, the biological time, invariant.

This concept is demonstrated through the simple mathematical steps shown below:

$$G = \frac{\tau_{growth} \bullet \gamma}{\tau \cdot \gamma} = \frac{\tau_{growth}}{\tau}$$

Where γ, in this case, represents the gravitational relativistic factor.
In summary, in an accelerated reference frame, *G* is given by:

$$G = \frac{t_{growth}}{t} = \frac{\tau_{growth}}{\sqrt{1-\frac{2ar}{c^2}}} \bullet \frac{\sqrt{1-\frac{2ar}{c^2}}}{\tau} = \frac{\tau_{growth}}{\tau} \tag{29}$$

and, in a gravitational reference frame:

$$G = \frac{t_{growth}}{t} = \frac{\tau_{growth}}{\sqrt{1-\frac{2KM}{rc^2}}} \bullet \frac{\sqrt{1-\frac{2KM}{rc^2}}}{\tau} = \frac{\tau_{growth}}{\tau} \quad (30)$$

Thus, in a generic non-inertial reference frame, *G* remains identical to its value in an inertial reference frame (see Eq.8).

In conclusion, this study highlights the invariance of biological time, as represented by the cellular generation number *G*, across both inertial and non-inertial reference frames. While relativistic time dilation influences physical clocks, *G* remains unaffected due to its mathematical definition as the ratio between the growth time and the duplication time, which ensures the cancellation of any relativistic effects on these intervals.

This invariance underscores the fundamental connection between biological processes and proper time, offering a universal metric for measuring biological time regardless of relativistic conditions. By establishing *G* as a reliable and invariant measure, this work provides a theoretical framework that could be extended to diverse biological systems, including more complex multicellular structures or tissues.

Abbreviations and Glossary

***c**:* The speed of light in a vacuum is approximately 300,000 km/s.

***Equivalence principle**:* A principle enunciated by Einstein stating that all effects of a uniform gravitational field are identical to those generated by a uniform acceleration of the coordinate system. This principle generalises a result of Newtonian gravitational theory, where a uniform acceleration of the coordinate system gives rise to a gravitational field.

g: Acceleration due to gravity at the surface of the Earth, approximately 9.81 m/s².

G: Number of bacterial generations or duplications.

***K:** (Gravitational constant):* The constant of proportionality in Newton's law of universal gravitation, with a value of $6.67430 \cdot 10^{-11} m^3 kg^{-1} s^{-2}$

Proper time (τ)**:** Time measured by a clock in the same reference frame, whether inertial (a reference frame that is stationary or moving at a constant relative velocity) or non-inertial (a reference frame that is uniformly accelerated or in a gravitational field). In both cases, it corresponds to the time measured by a clock that is stationary with respect to the reference frame.

Relative time (t): Time measured by an observer in a different frame of reference from the event being observed. It is affected by factors such as relative motion (special relativity) or gravitational fields (general relativity). (*Oxford Reference: A Dictionary of Physics*).

Time dilation: Time dilation is a phenomenon predicted by Einstein's theories of relativity, where time passes at different rates depending on relative motion and gravitational fields. In special relativity, an observer moving at high speeds relative to another will perceive time as passing more slowly. In general relativity, time runs slower in stronger gravitational fields; for example, a clock closer to a massive object like Earth or a black hole will tick more slowly compared to one further away. This means that time is not absolute but varies with speed and gravity. The relativistic gamma factor (γ) quantifies this effect and is calculated differently depending on whether the system is inertial or influenced by gravity.

Gamma factor (γ)*:* In inertial systems, the gamma factor is expressed by the following equation:

$$\gamma_{inertial} = \frac{1}{\sqrt{1-\frac{v^2}{c^2}}}$$

In gravitational systems, it is given by:

$$\gamma_{gravitational} = \frac{1}{\sqrt{1-\frac{2KM}{rc^2}}}$$

APPENDIX A

DERIVATION OF THE GENERAL EQUATION TO CALCULATE THE NUMBER OF GENERATIONS *G*

In general, population growth is governed by the following differential equation:

$$f(N) = \frac{dN}{dt}$$

In the relativistic framework, we must replace *t* with τ, the proper time:

$$f(N) = \frac{dN}{d\tau}$$

From this, we isolate τ:

$$d\tau = \frac{dN}{f(N)} \tag{A.1}$$

Integrating the left-hand side from 0 to τ_{growth} (the total growth time) and the right-hand side from N_0 to $N_{\tau(growth)}$, we have:

$$\int_0^{\tau(growth)} d\tau = \int_{N_0}^{N_{\tau(growth)}} \frac{dN}{f(N)}$$

$$\tau_{growth} = \int_{N_0}^{N_{\tau(growth)}} \frac{dN}{f(N)}$$

Using equation A.1 again, but this time integrating the left-hand side from 0 to τ (the time it takes for the population to double) and the right-hand side from N_0 to $2N_0$, we derive the general equation for calculating the doubling time of a population:

$$\int_0^{\tau} d\tau = \int_{N_0}^{2N_0} \frac{dN}{f(N)}$$

$$\tau = \int_{N_0}^{2N_0} \frac{dN}{f(N)}$$

From these equations, we derive the general formula to calculate *G*, regardless of the growth model:

$$G = \frac{\tau_{growth}}{\tau} = \frac{\int_{N_0}^{N_{\tau(growth)}} \frac{dN}{f(N)}}{\int_{N_0}^{2N_0} \frac{dN}{f(N)}}$$

In relativistic term τ_{growth} and τ, as seen by an observer moving at relativistic speeds, are dilated by the same amount, equal to the relativistic factor γ. Therefore, even when using the general equation to calculate G, it remains invariant with respect to any reference frame because γ cancels out mathematically.

Indeed:

$$G = \frac{\gamma \cdot \int_{N_0}^{N_{\tau(growth)}} \frac{dN}{f(N)}}{\gamma \cdot \int_{N_0}^{2N_0} \frac{dN}{f(N)}} = \frac{\tau_{growth}}{\tau}$$

REFERENCES

1. Ajdžanović, V.Z. et al. (2023). Biologia Futura: Does the Ageing Process Contribute to the Relativity of Time? *Biologia Futura*, 74, 137–143. https://doi.org/10.1007/s42977-023-00167-2.
2. Bailey, J., et al. (1977). 'Measurements of relativistic time dilation for positive and negative muons in a circular orbit.' *Nature*, 268(5618), 301-305. https://doi.org/10.1038/268301a0
3. Botermann, B., et al. (2014). 'Measurement of Time Dilation Using Stored Li^+ and Li^- Beams.' *Physical Review Letters*, 113(12), 120405. DOI: 10.1103/PhysRevLett.113.120405
4. Deguchi, S., Shimoshige, H., Tsudome, M., Mukai, S.-A., Corkery, R. W., Ito, S., & Horikoshi, K. (2011). Microbial growth at hyper accelerations up to 403,627 × g. *Proceedings of the National Academy of Sciences*, 108(19), 7997-8002. https://doi.org/10.1073/pnas.1018027108
5. Einstein, A. (1905). 'On the Electrodynamics of Moving Bodies.' *Annalen der Physik*, 322(10), 891-921. https://doi.org/10.1002/andp.19053221004.
6. Maestrini, D., Di Tullio, M., Castellano, C., & Rossi, F. (2018). Ageing in a Relativistic Biological Space-Time. *Frontiers in Cell and Developmental Biology*, 6:55. https://doi.org/10.3389/fcell.2018.00055.
7. Misner, C. W., Thorne, K. S., & Wheeler, J. A. (1973). *Gravitation (Section 7.4: Gravitational Redshift as Evidence for the Principle of Equivalence)*. W. H. Freeman and Company.
8. Oeseburg, H., et al. (2010). *Telomere biology in healthy aging and disease*. Pflügers Archiv - European Journal of Physiology, 459(2), 259–268. https://doi.org/10.1007/s00424-009-0728-1
9. Rossi, B., & Hall, D. B. (1941). 'Variation of the Rate of Decay of Mesotrons with Momentum.' *Physical Review*, 59(3), 223-228. https://doi.org/10.1103/PhysRev.59.223
10. Vaiserman, A., & Krasnienkov, D. (2021). *Telomere Length as a Marker of Biological Age: State-of-the-Art, Open Issues, and Future Perspectives*. Frontiers in Genetics, 11, 630186. https://doi.org/10.3389/fgene.2020.630186

Acknowledgments

The author expresses sincere gratitude to Dr Frans Jacobs for his fundamental advice in extending the results to general biological growth models. The author is also deeply thankful to the anonymous referee for their valuable suggestions and insightful comments, which significantly improved the quality of the manuscript.

Funding

This research did not receive any specific grant from funding agencies in the public, commercial, or not-for-profit sectors.

Declaration of competing interest

The author declares that there are no competing interests.

Data availability

No data were collected for this study.

Evaluating the Most Plausible Sm-Nd Isotopic Parameters for the Solar System/Planet Earth

Satya P Gargi

University of Houston-Downtown

ABSTRACT

These sets of isotopic parameters basically fall into two broad groups based on their values. The values of the parameters of various sets in each group are quite similar to each other but distinctly different from those of the other group. These parameters are also related to the Rb-Sr isotopic parameters because the latter are partly derived from the Sm-Nd isotopic parameters. As for instance but for the correlation between 87Sr/86Sr and 143Nd/144Nd ratios of recent oceanic basalts the present-day 87Sr/86Sr ratio couldn't be determined. So the most apt or plausible set of Sm-Nd isotopic parameters has to be not only internally consistent but also has to be consistent with the Rb-Sr isotopic parameters. In this paper I have shown how to distinguish internally consistent sets of Sm-Nd isotopic parameters and then how to pick up the one from those which is consistent with the Rb-Sr isotopic parameters as well. The one test of the internal consistency is that in which the measured present-day Nd isotope ratio matches very closely with the one computed from the other reference values. Then from the internally consistent sets, the one which is also consistent with the Rb-Sr isotopic parameters is considered to be the most plausible set of Sm-Nd isotopic parameters. The values of parameters are, 0.50677, 0.512636, and 0.1936 for the initial $^{143}Nd/^{144}Nd$ ratio, the present-day $^{143}Nd/^{144}Nd$ and the present-day $^{147}Sm/^{144}Nd$ ratios, respectively.

Keywords: Sm-Nd isotopic parameters, Rb-Sr isotopic parameters, chondrites, achondrites, juvinas.

Classification: LCC Code: QE501

Language: English

Great Britain Journals Press

LJP Copyright ID: 925613
Print ISSN: 2631-8490
Online ISSN: 2631-8504

London Journal of Research in Science: Natural & Formal

Volume 25 | Issue 2 | Compilation 1.0

Evaluating the Most Plausible Sm-Nd Isotopic Parameters for the Solar System/Planet Earth

Satya P Gargi

ABSTRACT

These sets of isotopic parameters basically fall into two broad groups based on their values. The values of the parameters of various sets in each group are quite similar to each other but distinctly different from those of the other group. These parameters are also related to the Rb-Sr isotopic parameters because the latter are partly derived from the Sm-Nd isotopic parameters. As for instance but for the correlation between 87Sr/86Sr and 143Nd/144Nd ratios of recent oceanic basalts the present-day 87Sr/86Sr ratio couldn't be determined. So the most apt or plausible set of Sm-Nd isotopic parameters has to be not only internally consistent but also has to be consistent with the Rb-Sr isotopic parameters. In this paper I have shown how to distinguish internally consistent sets of Sm-Nd isotopic parameters and then how to pick up the one from those which is consistent with the Rb-Sr isotopic parameters as well. The one test of the internal consistency is that in which the measured present-day Nd isotope ratio matches very closely with the one computed from the other reference values. Then from the internally consistent sets, the one which is also consistent with the Rb-Sr isotopic parameters is considered to be the most plausible set of Sm-Nd isotopic parameters. The values of parameters are, 0.50677, 0.512636, and 0.1936 for the initial $^{143}Nd/^{144}Nd$ ratio, the present-day $^{143}Nd/^{144}Nd$ and the present-day $^{147}Sm/^{144}Nd$ ratios, respectively.

Keywords: Sm-Nd isotopic parameters, Rb-Sr isotopic parameters, chondrites, achondrites, juvinas.

Author: University of Houston-Downtown, Department of Natural Sciences, One Main Street, Houston, TX 77002, USA.

HIGHLIGHTS

- Why the discrepancy in the values of the parameters from two broad groups of sets of Sm-Nd isotopic parameters.
- What two conditions a set of Sm-Nd parameters has to meet to be regarded as the most plausible.
- What is internal consistency and how the internal consistency of a set of parameters is determined.
- What is the role of the internally consistent Rb-Sr isotopic parameters in determining the aptness of a set of Sm-Nd isotopic parameters.
- How the internally consistent set of Rb-Sr isotopic parameters is determined.

I. INTRODUCTION

The values of the parameters in each group are quite similar to each other but distinctly different from those of the other group.. The moot question - which is the best or the most appropriate set of Sm-Nd isotopic parameters for the Planet Earth cannot be answered in isolation from the Rb-Sr isotopic parameters as the latter are partly derived from the former and the two isotopic systems are thus interrelated and interdependent with each other. One thing that will determine which set of the parameters is the most appropriate does not depend on how precisely the isotopic ratios were measured but how the isotopic parameters of both the isotopic systems were determined – that is, by what method and from what source material, and how well they satisfy the internal.

II. DETERMINING SM-ND ISOTOPIC PARAMETERS FROM CHONDRITES OR ACHONDRITES

The chondritic meteorites, of all the meteorites, are the most primitive and undifferentiated planetary objects. Naturally, these should be considered the best representatives of the Solar Nebula. Their importance also lies in the fact that these are the only primitive planetary objects and almost of the same age as the Earth, on which we can lay our hands and analyze them. Obviously chondritic meteorites should be used to define the Sm-Nd isotopic evolution of the Solar Nebula. But most of the chondrites were subjected to severe shocks and brecciation (Cf. Minster et al., 1982) soon after they were formed, and that has disturbed their isotopic system. Also many of the chondrites show signs of secondary alteration by the action of water (Ebihara et al., 1982; Macdougal et al., 1984). Because of this, they do not yield well defined Rb-Sr or Sm-Nd isochrons. The achondrites, on the other hand though highly differentiated objects, yield very precise isochrons both for Rb-Sr and Sm-Nd systems. As the Sm/Nd ratio of achondrite Juvinas (0.3072) (Lugmair et al., 1975c) is comparable to that of the chondrites (0.3081) (Masuda et al., 1973; Masuda, 1975), and their Sm–Nd isochron age also is very similar to that of the Earth (Lugmair, 1974), the isotopic characteristics of Juvinas, therefore, could be used to define the isotopic parameters of the Solar System/Planet Earth.

2.1. Sm-Nd isotopic parameters from the continental rocks and the achondrite Juvinas

DePaolo and Wasserburg (1976a, 1976b) showed that initial Nd isotopic ratios of old intrusive continental rocks of various lithologies, mostly silicic rocks, ranging in age from 3.8 Gyr to 1.00 Gyr and young continental basalts with few exceptions fall within error on the chondritic evolution line. This indicates that continental silicic rocks throughout the geologic history appear to have been derived from a single uniform widespread reservoir having REE characteristics of ordinary chondrites. They termed this reservoir as chondritic uniform reservoir, CHUR, which in their opinion resides most probably in the mantle. They consider CHUR an important reservoir and representative of the Planet Earth, whose Sm-Nd isotopic characteristics closely proximate that of the Juvinas achondrite.

DePaolo and Wasserburg (1976a, 1976b), therefore, claim to use the isotopic characteristics of the Juvinas achondrite to define the Sm-Nd isotopic parameters of CHUR. However, they used the values of 0.1936 for the $^{147}Sm/^{144}Nd$ ratio, 0.50598±10 for the initial ratio (I_{JUV}) and 0.511836 for the present day $^{143}Nd/^{144}Nd$ ratio ($I_{CHUR}(0)$). They asserted that these values are based on the isotopic characteristics of Juvinas (Lugmair, 1974, pers. comm.; Lugmair et al., 1975 b). They contended that this $I_{CHUR}(0)$ value is much lower than, and differs significantly from what was reported by Lugmair (1974, pers. comm.); and is considered as the best revised estimate for the $^{143}Nd/^{144}Nd$ ratio ($I_{CHUR}(0)$) of the Juvinas as per the personal communication of Lugmair (1974) to them. However, he in his paper (Lugmair, 1974) reported only the initial $^{143}Nd/^{144}Nd$ ratio (I_{JUV}), and the age of the Juvinas, which are 0.50687±10, and 4.56±0.08 Ga, respectively. He derived these values from the internal isochron of Juvinas; and there is no reference to the Nd isotopic ratio, or the $^{147}Sm/^{144}Nd$ ratio of Juvinas. Lugmair and Scheinin (1976c) reported a very similar initial$^{143}Nd/^{144}Nd$ ratio from Angra dos Reis achondritic meteorites. They analyzed various mineral fractions of the meteorite and obtained an initial ratio of 0.50682 ± 0.0005, and an isochron age of 4.55 ± 0.04 Gyr which are very similar to those of Juvinas as determined by Lugmair (1974).

Further, no reference of the initial or the present-day $^{143}Nd/^{144}Nd$ values as used by DePaolo and Wasserburg (1976a) is found in any of the subsequent publications of Lugmair (Cf. Lugmair et al., 1975a; Lugmair et al., 1975b; Lugmair et al., 1975c; Lugmair et al., 1976a, Lugmair et al., 1976 b). The initial ratio, and the measured Nd isotopic ratio of the Juvinas as reported by Lugmair et al. (1975b, 1975c) are significantly different from those suggested by DePaolo and Wasserburg (1976). Later,

Lugmair et al. (1976a) gave revised values for the initial $^{143}Nd/^{144}Nd$ (I_{JUV}) ratio, and the measured $^{143}Nd/^{144}Nd$ ratio by dating the bulk sample of Juvinas, which respectively is 0.50677±0.00010, and 0.512636±0.000040. They stated that these are updated values and are a little lower than the ones given earlier by Lugmair et al. (1975b, 1975c). The value of the present-day $^{143}Nd/^{144}Nd$ ratio of Juvinas seems to be revised again as Stosch et al. (1984) used a little lower value of 0.512566 for this ratio. However, all the values for the Sm-Nd isotopic parameters obtained by dating the Juvinas by Lugmair and his associates are quite different from those used by DePaolo and Wasserburg (1976a) in their model.

2.2. Sm-Nd isotopic parameters from chondrites and Juvinas achondrite

Subsequently, Jacobsen and Wasserburg (1980) analyzed five chondrites and Juvinas achondrites for their $^{143}Nd/^{144}Nd$, and $^{147}Sm/^{144}Nd$ ratios. These samples defined an isochron which indicated an initial ratio of 0.505828±9 at 4.6 Ga. Based on this data, they suggested a new set of present-day Sm-Nd isotopic parameters for CHUR. Those values are 0.511836 for $(^{143}Nd/^{144}Nd)_{CHUR}(0)$, and 0.1967 for $(^{147}Sm/^{144}Nd)$. It may be noticed that the values of two of the parameters are slightly different from those used by DePaolo and Wasserburg (1976a). The value for the present-day Nd isotopic ratio is same, whereas the value for the initial Nd isotopic ratio is slightly lower, and that for the present-day $(^{147}Sm/^{144}Nd)$ ratio is slightly higher. They also stressed that they consider these parameters to be self-consistent. Jacobsen and Wasserburg (1984) analyzed five more chondrites and the chondrites Moama and Angra dos Reis for investigating their Sm-Nd isotopic systematics. They reported that the isotopic data obtained from these meteorites is consistent with the previously reported reference values for CHUR of $(^{143}Nd/^{144}Nd)_{CHUR}(0) = 0.511847$, $(^{147}Sm/^{144}Nd)_{CHUR}(0) = 0.1967$. However, the value of 0.511847 for the $(^{143}Nd/^{144}Nd)_{CHUR}(0)$ ratio reported here is slightly higher than the one previously reported by them (Jacobsen and Wasserburg,1980). Also this set of values for the Sm-Nd isotopic parameters for the CHUR/Planet Earth based on the analysis of chondrites by Jacobsen and Wasserburg (1980, 1984) are quite different from those derived from the achondrite Juvinas by Lugmair (1974) and Lugmair et al. (1975b, 1975c). This gives the impression that chondrites are somewhat different from the achondrites with respect to their Sm-Nd isotopic evolultion. However, this is not the case as shown by the work of Benjamin et al. (1987) on chondrites. They dated some chondrites by the Sm-Nd method of dating. They showed that chondrites define an isochron corresponding to an age of 4.55±0.45 Ga with an initial Nd isotopic ratio of 0.5067±5, which is very much consistent with the initial ratio of Juvinas (0.506705 for a 4.56 Ga age). Also, Amelin and Rotenberg (2004) reported almost identical results from their Sm – Nd isotopic investigation of chondrites. They analyzed 34 samples of phosphate fractions and chondrules from six ordinary chondrites and one carbonaceous chondrite for studying their Sm-Nd systematics. These samples defined an isochron which yielded a date of 4588 ± 100 Myr, and an initial $^{143}Nd/^{144}Nd$ ratio of 0.50665 ± 0.00014. They also suggested a median $^{147}Sm/^{144}Nd$ ratio of 0.1964 + 0.0003/ - 0.0007 based on the compilation of the published data of chondritic whole rock Sm – Nd analysis. From this value and the Sm – Nd isochron, they derived the present-day CHUR $^{143}Nd/^{144}Nd$ value of 0.512637 + 0.000009/ - 000021.

III. TEST OF THE INTERNAL CONSISTENCY OF THE SM-ND ISOTOPIC PARAMETERS

It appears that the results of Sm-Nd isotopic analysis for the chondrites from the two sets of laboratories are quite different. So what is the reason for the results from the two sets of laboratories to be so different? The most likely reason for this is the inter-laboratory bias because of the different ways of carrying out analysis for Nd isotopic compositions (Faure, 1986; Faure and Mensing, 2004). This inter-laboratory bias has rendered the comparison of Sm-Nd isotopic data from different laboratories very difficult. Ideally, no matter what method is used for analysis, the end result should be the same.

However, it is not the case. Therefore, the important point here is which of the two sets of reference values should be considered credible for the Planet Earth isotopic parameters. In order for any set of Sm-Nd reference values to be considered feasible, it is important to see that not only they are internally consistent but they also should satisfy the constraint imposed by the present-day Sr isotopic ratio. Jacobsen and Wasserburg (1980) had contended that the reference values that they have proposed for the Sm-Nd Planet Earth parameters are self-consistent. But they did not show how and on what basis these values were considered to be self-consistent. One test to check the self-consistency of the reference values, in other words, to see how well they satisfy their internal constraints, involves comparing the measured Nd isotopic ratios with those computed from the other reference values as shown in the table below. However, this test by itself should not be considered as the sole criterion for judging the plausibility of the parameters because they also have to satisfy the constraints imposed by the Rb-Sr isotopic parameters. But it excludes those from consideration which do not satisfy the internal constraints.

The following table shows the computed and measured Nd isotopic ratios from the data of Jacobsen and Wasserburg (1984), DePaolo and Wasserburg (1976a), Lugmair et al. (1976a) and Amelin and Rotenberg (2004).

Table showing the difference between the measured and computed Present-day Nd isotopic ratios

	Jacobsen and Wasserburg (1984)	DePaolo and Wasserburg (1976a)	Lugmair et al. (1976a)	Amelin and Rotenberg (2004)
Present-day $^{143}Nd/^{144}Nd$ ratio (measured):	0.511847	0.511836	0.512636	0.512637
Initial $^{143}Nd/^{144}Nd$ ratio:	0.505828	0.50598	0.50677	0.50665
Present-day $^{147}Sm/^{144}Nd$ ratio	0.1967	0.1936	0.1936	0.1964
Decay constant:	6.54E-12/Yr	6.54E-12/Yr	6.54E-12/Yr	6.54E-12/Yr
Time elapsed:	4560000000	4560000000	4560000000	4560000000
Initial $^{147}Sm/^{144}Nd$ ratio (Computed):	0.20265441	0.19946057	0.19946057	0.202345331
$^{143}Nd/^{144}Nd$ produced in 4.56 Gyr (Computed):	0.00595441	0.005860570.	00586057	0.005945331
Present-day $^{143}Nd/^{144}Nd$ ratio (Computed):	.51178241	0.511782412	0.51263057	0.512595331
Diff. between the computed. and measured ratios:	0.000064588	0.000004570	0.000005430	0.000041669

The above table shows that the present-day Nd isotopic ratios computed from the reference values proposed by Jacobsen and Wasserburg's (1984), and Amelin and Rotenberg (2004) are much smaller than their measured ratios which means that the difference between the two ratios is very high. Whereas in the case of those proposed by Lugmair et al. (1976a), and DePaolo and Wasserburg (1976a), the computed and measured ratios are quite similar. The difference between the two ratios in the former case is almost ten times greater than that in the latter ratios. This shows that the Nd isotopic parameters proposed by Jacobsen and Wasserburg (1984), and by Amelin and Rotenberg (2004) are not internally consistent as they do not satisfy their internal constraints. So this leaves the reference values suggested by Lugmair et al. (1976a), and by DePaolo and Wasserburg (1976a) in contention for the viability as both seem to satisfy their internal constraints.

IV. RELATIONSHIP BETWEEN THE PRESENT-DAY ND AND SR ISOTOPIC RATIOS OF RECENT ROCKS

In fact the most important point in evaluating the aptness of the Sm-Nd isotopic parameters is the relationship of the Nd and Sr isotopic ratios of recent rocks. So before considering any reference values for the Sm-Nd isotopic parameters for the Planet Earth, the relationship between the Nd and Sr isotopic ratios of recent rocks have to be evaluated first.

The Rb-Sr isotopic parameters for the Planet Earth, unlike the Sm-Nd parameters, cannot be determined directly from the meteorites – chondrites or achondrites, because they have been subjected to differentiation and/or alteration after their accretion from the Solar Nebula which has caused the fractionation of volatile elements such as Rb and Sr. As a result, Rb-Sr isotopic evolution in meteorites has deviated from their normal evolutionary course. Because of this, meteorites in general are not considered as very good representatives of the Solar Nebula with respect to the Rb-Sr isotopic evolution. However, it is the relationship of the present-day Sr isotopic ratios with Nd isotopic ratios of Recent oceanic basalts which has helped in deducing the Rb-Sr isotopic parameters for the Planet Earth/Solar Nebula. Richard et al. (1976) showed that in Recent oceanic basalts, $^{87}Sr/^{86}Sr$ isotopic ratios have an inverse correlation with their corresponding $^{143}Nd/^{144}Nd$ isotopic ratios. DePaolo and Wasserburg (1976b, 1977) showed a similar inverse correlation between initial Nd and Sr isotopic ratios of young volcanic rocks (zero age) from both oceans and continents. These rocks included MOR tholeiitic basalts, continental flood basalts, oceanic island basalts and a few other volcanics from the continent. However, on the correlation diagram, Nd isotopic ratios were shown as normalized to the present-day Nd isotopic ratio of Juvinas (0.511836) (DePaolo and Wasserburg, 1976a). According to them the strong correlation between the initial Nd and Sr isotopic ratios of young basalts indicates that the Rb-Sr and Sm-Nd fractionation events are correlative and caused by the same process. Therefore, they took the $^{87}Sr/^{86}Sr$ ratio corresponding to the present-day $^{143}Nd/^{144}Nd$ ratio of Juvinas of 0.511836 on this correlation diagram as the present-day $^{87}Sr/^{86}Sr$ ratio of the Planet Earth. They thus suggested 0.7045 as the present-day $^{87}Sr/^{86}Sr$ ratio of the Planet Earth. Using this ratio and BABI (0.69899) (Pappanastassiou and Wasserburg, 1969) as the isotopic ratio of the Planet Earth at the time of its formation, and the decay constant λ_{Rb} of 1.39 E-11 Yr-1, they calculated the present-day Rb/Sr ratio of the unfractionated mantle/Planet Earth to be 0.029. They further estimated the present-day $^{87}Rb/^{86}Sr$ ratio of the Planet Earth to be 0.0839.

All`egre et al. (1979) viewed the correlation between Nd and Sr isotopic ratios of the Recent oceanic basalts as of geochemical significance because it could be used to deduce the present-day Sr isotopic parameters for the Planet Earth. They maintained that as the Earth has chondritic REE distribution, and as the Juvinas achondrites have nearly unfractionated Sm/Nd ratio, the Sr isotopic ratio corresponding to the present-day Nd isotopic ratio of the Juvinas achondrite on this relation, therefore, should closely proximate the Planet Earth/planetary value. Following on this assumption, they suggested that the $^{87}Sr/^{86}Sr$ ratio of 0.70478 ± 0.00008 corresponding to the present-day $^{143}Nd/^{144}Nd$ value of 0.511836 of Juvinas achondrite (DePaolo and Wasserburg, 1976a) on this relation, should be regarded as the planetary value. They further added that this value along with the initial Sr isotopic ratio of 0.69899, and λ_{Rb} of $(1.42\pm0.01)10^{-11}y^{-1}$ corresponds to the present-day Rb/Sr ratio of 0.031 and $^{87}Rb/^{86}Sr$ of 0.090 for the Planet Earth.

Later, All`egre (1982) referred to the inverse correlation between the Sr and Nd isotopic ratios of recent oceanic island basalts and ridge basalts as the reference array for the whole Earth. Further, he used the value of 0.51264 (Lugmair, 1976a) instead of 0.511836 (Cf. DePaolo and Wasserburg, 1976a; Cf. Jacobsen and Wasserburg, 1980) for the present-day $^{143}Nd/^{144}Nd$ ratio for deducing the present-day Sr isotopic ratio of the Planet Earth from this relation. This led to a slight revision of his previously suggested value of 0.70478 for this parameter. His new revised reference value for this parameter is 0.7047 ± 0.00008, which corresponds to the present-day $^{87}Rb/^{86}Sr$ ratio of 0.09 for the Planet Earth.

V. ND ISOTOPIC EVOLUTION FROM THE INITIAL ND ISOTOPIC RATIOS OF ARCHEAN ROCKS

O'Nions et al. (1979) observed that the Nd isotopic evolution in continental rocks as inferred from the initial $^{143}Nd/^{144}Nd$ ratios of Archean rocks such as Isua metavolcanics, Onverwacht lavas, Bulawayan

volcanics, and Lewisian gneisses (Hamilton et al. 1977, 1978a,b,c) is consistent with the view that the Planet Earth evolved with chondritic Sm/Nd. This observation of theirs is in accord with that of DePaolo and Wasserburg (1976a, 1976b). However, according to them, Planet Earth evolved with Sm-Nd similar to that of Angra dos Reis achondrites. Therefore, they assumed the Sm/Nd ratio for the Planet Earth to be similar to the chondritic average value of 0.308 (Nakamura et al. 1976). So according to them the $^{143}Nd/^{144}Nd$ ratio for the Planet Earth at the time of its formation 4.55 Gyr ago should be 0.50682 (Cf. Lugmair & Marti, 1977). Its present-day $^{143}Nd/^{144}Nd$ ratio based on these values was estimated to be 0.51262. They also showed the existence of a strong inverse relationship between the $^{143}Nd/^{144}Nd$ and $^{87}Sr/^{86}Sr$ ratios of Recent oceanic ridge basalts and oceanic island basalts, which in their view signifies that these isotopes have fractionated coherently during differentiation of the magma. Therefore, $^{87}Sr/^{86}Sr$ ratio corresponding to the present-day $^{143}Nd/^{144}Nd$ ratio on this relation should be taken as the present-day Planet Earth ratio. From this relation, they thus obtained 0.7047 as the present-day Sr isotopic ratio for the Planet Earth. However, for this they used the value of 0.51265 as the present-day Nd isotopic ratio as against the value of 0.511836 used by DePaolo and Wasserburg (1976a, 1976b). From this they deduced the present-day Rb/Sr ratio of the Planet Earth to be approximately 0.03. However, O'Nions et al. (1977) had earlier estimated the present-day $^{87}Sr/^{86}Sr$ and Rb/Sr ratios of 0.705, and 0.032 respectively for the Planet Earth from the inverse correlation formed by the Sr and Nd isotopic ratios of Recent oceanic basalts from the Mid Atalantic Ridge, Atlantic Islands, Reykjanes Ridge, and Iceland. But they also noticed that the oceanic basalts from the Hawaiian Islands from the Pacific Ocean do not show any such correlation between their Sr and Nd isotopic ratios.

Gargi (2012) came out with a novel computer model (herein referred to as SG Model) to infer the isotopic characteristics of the source reservoirs of igneous rocks using Rb/Sr and $^{87}Rb/^{86}Sr$ ratios only. This model makes it possible to determine the Rb-Sr isotopic characteristics of a source reservoir with respect to its $^{87}Rb/^{86}Sr$ as well as $^{87}Sr/^{86}Sr$ isotopic ratio. However, the SG model also contains other relations by which the model age and the beginning Sr isotopic ratio of a rock can be determined without requiring the direct input of $^{87}Sr/^{86}Sr$ ratio, or the decay constant, λ_{Rb}. The SG model is a purely theoretical model, and is internally consistent as it is not dependent on any data from meteorites or terrestrial rocks; and the model is derived using hypothetical rocks of various ages.

The SG model is based on the relationship of Rb/Sr and $[(Rb/Sr)/(^{87}Rb/^{86}Sr)]$ ratios. The basic premise of the model is that the two cosmic ratios, Rb/Sr and $^{87}Rb/^{86}Sr$, have been evolving with time because of the decay of ^{87}Rb, and the resulting accumulation of ^{87}Sr since the time ^{87}Rb nuclides first manifested in the universe about 542 Gyr ago (Cf, Gargi, 1987; Cf. Gargi, 2005; Gargi 2019). Similarly it was further assumed that no ^{87}Rb was produced by nucleosynthesis in the interior of the stars, and all of the ^{87}Rb nuclides in the Universe manifested in space-time. Therefore, the isotopic evolutions of ^{87}Rb and ^{87}Sr have always been complementary and integral to each other since the time ^{87}Rb first appeared in the universe. Stated otherwise, it means that all of the ^{87}Sr nuclides in the universe are of radiogenic origin, that is, they owe their origin solely to the decay of ^{87}Rb, and no ^{87}Sr was ever produced by any means other than the decay of ^{87}Rb (Cf. Gargi, 2005, Gargi 2019), such as by nucleosynthesis in the interior of the stars as is commonly believed by many astrophysicists. It follows then that at a certain point of time in the past the $^{87}Sr/^{86}Sr$ ratio must have been null. Because of the continuous decay of ^{87}Rb into its daughter isotope of ^{87}Sr, the $^{87}Rb/^{86}Sr$, Rb/Sr and $^{87}Sr/^{86}Sr$ ratios have been evolving continually with time. These ratios evolving with time form the basis of the SG's model for characterizing the source reservoir of igneous rocks and for determining the model age and the beginning Sr isotopic ratio of rocks. The evolution of these ratios through time was calibrated by plotting Rb/Sr ratio against $[(Rb/Sr)/(^{87}Rb/^{86}Sr)]$ ratio of hypothetical rocks of various ages on the X-Y plot.

In order to formulate this model, initially, values of certain parameters, such as the Rb-Sr isotopic parameters of the Planet Earth, age of the Earth, and the decay constant, λ_{Rb}, etc. had to be presumed which were later modified by using the interplay of the constraints imposed by the various parameters on each other. The presumed values were within the range of the values found in literature. The interplay of the mutual constraints made it possible to define the final values of the parameters. To see the effect of the mutual constraints on the various parameters a relation was required in which all those parameters which have a bearing on the cosmic Rb-Sr isotopic evolution are involved. As was mentioned earlier, that the $^{87}Rb/^{86}Sr$ and $^{87}Sr/^{86}Sr$ ratios are not random ratios resulting from the nucleosynthesis but are complementary to each other because of the decay of ^{87}Rb and the resulting accumulation of ^{87}Sr since the time ^{87}Rb first manifested in the Universe. So as per this premise, before any ^{87}Rb had manifested in the Universe, there should not have been any ^{87}Sr. Therefore, in a relation where the X entity is dependent on the $^{87}Rb/^{86}Sr$ ratio and the Y entity is dependent on the $^{87}Sr/^{86}Sr$ ratio, the linear array formed by two such entities in an X-Y plot should go to the point of origin, that is, the value of the Y-intercept should be NULL because if there is no ^{87}Rb, there cannot be any ^{87}Sr. Such a relation was provided by the Ruh relation in the SG model (See Figure 1). The significance of this relation is that it is the only relation in which all those parameters which have a bearing on the Rb-Sr isotopic evolution are involved. Because the SG model is in fact a single computer program based on the MS Excel Spreadsheet program, therefore, any change in any of the parameters affects the whole spreadsheet and all the relations it comprises. In order to determine the final values of the various parameters their values were changed by hit and trial method and their effect was observed on the linear array of the Ruh relation. This was done until the linear array formed a NULL Y-Intercept or was as close as possible to the NULL value. That is how the final values of the various parameters were determined.

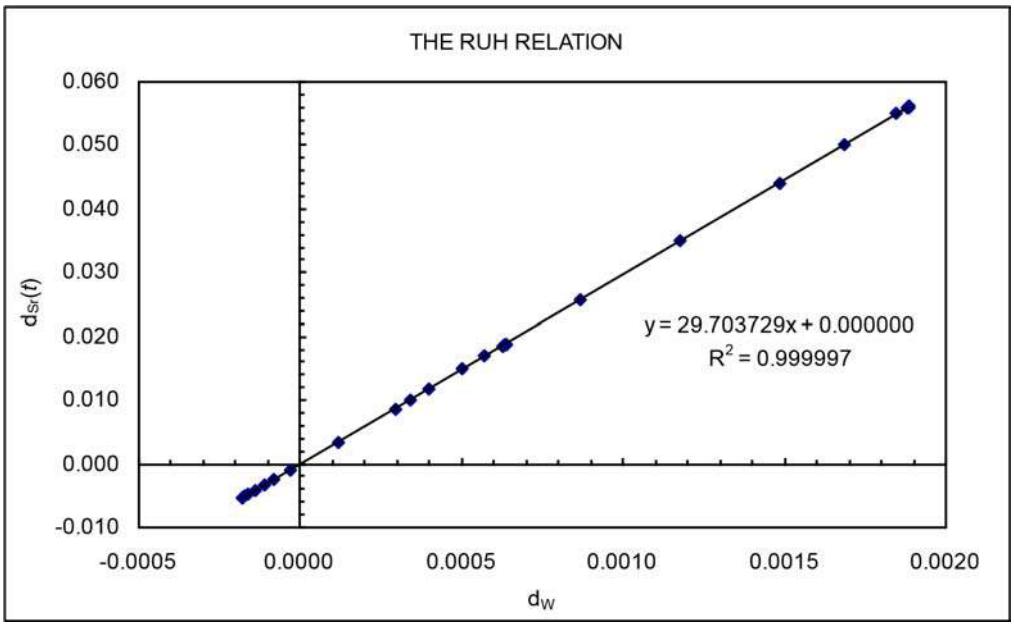

Figure 1: Shows the Ruh relation formed by plotting d_w ratio on the X-axis against the $d_{Sr}(t)$ ratio on the Y-axis. The X-axis entity d_w is dependent on the $^{87}Rb/^{86}Sr$ ration and the Y-axis entity d_{Sr} (t) is dependent on the $^{87}Sr/^{86}Sr$ ratio. The linear array formed by this correlation passes through the point of origin.

VI. TEST OF THE INTERNAL CONSISTENCY OF THE RB-SR ISOTOPIC PARAMETERS

However, the confirmation about these Rb-Sr isotopic parameters as being apt and plausible comes from the fact that the model yields the age and initial Sr isotopic ratio of well dated meteorites and

rocks from the youngest to the oldest that match very closely with their published results. Values of the parameters from no other set than those used in this model produce such results. The validity and authenticity of the Rb-Sr isotopic parameters as given by the SG model is further confirmed by the test of the internal consistency in which the difference between the measured and the computed values of the present-day $^{87}Sr/^{86}Sr$ from the various sets of Rb-Sr parameters is compared. The table below shows that of all the sets of parameters, the difference between the computed and measured present-day $^{87}Sr/^{86}Sr$ ratios is the least only in the case of the SG model. Thus the reference values of the various parameters as used in this model are internally consistent, and satisfy all the internal and external constraints.

Table showing the differences between the measured and computed Present-day $^{87}Sr/^{86}Sr$ isotopic ratios

Gargi (2012)	DePaolo and Wasserburg (1976b)		All`egre (1982)
Present-day $^{87}Sr/^{86}Sr$ ratio (measured)	0.704698	0.7045	0.7047
Initial $^{87}Sr/^{86}Sr$ ratio:	0.69878	0.69899	0.69898
Present-day $^{87}Rb/^{86}Sr$ ratio	0.089442	0.084	0.09
Decay constant used:	1.408E-11/Yr	1.39E-11/Yr	1.42E-11/Yr
Time elapsed:	4550000000	4550000000	4550000000
Initial $^{87}Rb/^{86}Sr$ ratio (Computed):	0.09535954	0.08948418	0.096006862
$^{87}Sr/^{86}Sr$ produced in 4.55 Gyr (Computed):	0.00591754	0.00548418	0.006006862
Present-day $^{87}Sr/^{86}Sr$ ratio (Computed):	0.704697539	0.704474175	0.704986862
Diff. between the comptd. and measured ratios:	0.000000461	0.000025826	-0.000286862

The values of the Rb-Sr isotopic parameters for the Planet Earth such as the beginning $^{87}Sr/^{86}Sr$ ratio, present-day $^{87}Sr/^{86}Sr$ ratio, $^{87}Rb/^{86}Sr$ ratio, and Rb/Sr ratio, as proposed by Gargi (2012), are 0.69878, 0.704698, 0.089442, and 0.031, respectively. Gargi's (2012) model, and the parameters used to define the model are consistent with the decay constant, λ for ^{87}Rb, and the age of the Earth being equal to 1.408 EXP-11/Yr, and 4.55 Gyr, respectively.

However, for the discussion here, the parameter of interest is the present-day $^{87}Sr/^{86}Sr$ ratio as it has been derived from the present-day $^{143}Nd/^{144}Nd$ ratio of the Earth. Both All`egre et al. (1982), and O'Nions et al. (1979) proposed the value of 0.7047 as the present-day $^{87}Sr/^{86}Sr$ ratio for the Planet Earth. They deduced this value from the inverse correlation of $^{143}Nd/^{144}Nd$ with $^{87}Sr/^{86}Sr$ ratios of recent oceanic basalts. To derive this value, All`egre (1982) used the value of 0.51264 for the present-day $^{143}Nd/^{144}Nd$ ratio (Cf. Lugmair, 1976a), whereas O'Nions et al. (1979) used the value of 0.51265, which also is very similar to that of Lugmair (1976) value.

As the present-day Sr isotopic ratio for the Planet Earth obtained by using the present-day $^{143}Nd/^{144}Nd$ ratio suggested by Lugmair (1976) matches very closely with the one given by the SG model, the reference values for the Sm-Nd isotopic parameters for the planet Earth suggested by Lugmair (1976), therefore, should be considered as the most appropriate and plausible parameters.

VII. CONCLUSION

For any set of the Sm-Nd isotopic parameters to be considered the most appropriate and plausible it has to be internally consistent as well as it also has to be consistent with the Rb-Sr isotopic parameters as these are partly derived from the former. I have shown in this paper how to pick the internally consistent sets of Sm-Nd isotopic parameters from amongst the several such sets in vogue, and then how to pick the one from amongst these sets which is also consistent with the Rb-Sr isotopic parameters. So based on this analysis, the set of the Sm-Nd isotopic parameters given by Lugmair

(1976) is considered to be the most plausible and appropriate. The values of these parameters are, 0.50677, 0.512636, and 0.1936 for the initial 143Nd/144Nd ratio, the present-day 143Nd/144Nd and the present-day 147Sm/144Nd ratio, respectively. These values are consistent with the present-day 87Sr/86Sr ratio of 0.704698 as given by Gargi (2012). It further shows that the decay constant λ for 87Rb of 1.408E-11/Yr given by Gargi (2012, 2019) is the most plausible decay constant. It also shows that achondrites yield better results than chondrites for the Sm-Nd isotopic parameters. Thus the values of the most plausible set of Sm-Nd isotopic parameters are, 0.50677, 0.512636, and 0.1936 for the initial $^{143}Nd/^{144}Nd$ ratio, the present-day $^{143}Nd/^{144}Nd$ and the present-day $^{147}Sm/^{144}Nd$ ratio, respectively.

Note: This work was not supported by any Grant or funds from any source.

REFERENCES CITED

1. All`egre, C.J., 1982. Chemical geodynamics. Tectonophysics 81, 109-132.
2. All`egre, C.J., Othman, D.B. Polve, M., Richard, P., 1979. The Nd-Sr isotopic correlation in mantle materials and geodynamic consequences. Phys. Earth Planet. Inter. 19, 293-306.
3. Amelin, Y., and Rotenberg, E., 2004. Sm-Nd systematics of chondrites. Earth Planet. Sci. Lett. 223, 267-282.
4. Benjamin, J.C., Podosek, F.A., and Lugmair, G.W., 1987. Initial Sr-87/Sr-86 and Sm-Nd chronology of chondritic meteorites. Lunar and Plaenet. Sci. Conf. 18th, Houston, TX, Proceedings (A89–10851 01-91), Cambridge Univ. Press / Lunar and Planetary Institute, 555-564.
5. DePaolo, D.J. and Wasserburg, G. J., 1976a. Nd isotopic variations and petrogenetic models. Geophys. Res. Lett. 3, 249-252.
6. DePaolo, D.J. and Wasserburg, G. J., 1976b. Inferences about magma sources and mantle structure from variations of $^{143}Nd/^{144}Nd$. Geophys. Res. Lett. 3, 743-746.
7. DePaolo, D.J. and Wasserburg, G. J., 1977. The sources of island arcs as indicated by Nd and Sr isotopic studies. Geophy. Res. Lett. 4, 465-468.
8. Ebihara, M., Wolf, R. and Anders, E., 1982. Are C1 chondrites chemically fractionated? A trace element study. Geochimica et Cosmochimica Acta, 46, 1849 – 1861.
9. Faure, G., 1986. Principles of Isotope Geology, 2nd ed. John Wiley & Sons, New York, p. 589.
10. Faure, G. and Mensing, Teresa M., 2004. Isotopes: Principles and Applications, 3rd ed. John Wiley & Sons, New Yourk, p. 928.
11. Gargi, Satya P., 1987. An isotopic model for the age and origin of the cosmos (ABSTRACT). EOS Trans. AGU 68, Fall Meeting Suppl., 1515.
12. Gargi, S.P., 2005. Towards the theory of the age, origin and demise of the universe – A geochemical/Isotopic perspective (ABSTRACT). EOS Trans. AGU 86 (52).
13. Gargi, S.P., 2012. Characterizing source reservoirs of igneous rocks: A new perspective. Fractionation of radiogenic isotopes: A new tool for petrogenesis. Chemie der Erde 72, 323-332.
14. Gargi, S.P., 2019. Measuring the decay constant of 87Rb: Is the decay in radioisotopes linear? Manifestation and disintegration of the matter in space-time, and age of the Universe. Solid Earth Sciences. 4, 12-26
15. Jacobsen, S.B., and Wasserburg, G.J., 1980. Sm-Nd isotopic evolution of chondrites. Earth Planet. Sci. Lett. 50, 139-155.
16. Jacobsen, S.B., and Wasserburg, G.J., 1984. Sm-Nd isotopic evolution of chondrites and achondrites, II. Earth Planet. Sci. Lett. 67, 137-150.
17. Lugmair, G.W., 1974. Sm – Nd ages: A new dating method. Meteoritics 9. 369.
18. Lugmair, G.W., and Marti, K., 1977. Sm – Nd – Pu timepieces in the Angra dos Reis meteorite. Earth Planet. Sci. Lett. 36, 273-284.

19. Lugmair, G .W., and Scheinin, N.B., 1976. Sm – Nd systematics of Angra dos Reis. Meteoritics 11, 322 - 323.
20. Lugmair, G.W., Marti, K., Kurtz, J.P. & Scheinin, N. B., 1976a. History and genesis of lunar troctolite 76535 or How old is old. In: Lunar Sci. Conf., 7th, Houston, TX, Proceedings. 2 (A77 – 34651, 15-91), New York, Pergamon Press, Inc., 2009. – 2033.
21. Lugmair, G.W., Kurtz, J.P., Marti, K., and Scheinin, N. B., 1976b. The low Sm/Nd regions of the moon: Evolution and history of a troctolite and KREPP basalt (ABSTRACT). In: Lunar Science VII, 509-511, The Lunar Science Institute, Houston, TX.
22. Lugmair, G.W., Scheinin, N. B., and Marti K., 1975a. Sm – Nd age of Apollo 17 basalt 75075: Two-stage igneous process in mare basalt genesis (Abstract). Lunar Sci. Conf. VI, Lunar Sci. Inst., Houston, 531 - 533.
23. Lugmair, G.W., Scheinin, N. B., and Marti K., 1975b. Search for extinct ^{146}Sm, 1. The isotopic abundance of ^{142}Nd in the Juvinas meteorite. Earth Planet. Sci. Lett. 27, 79-84.
24. Lugmair, G.W., Scheinin, N. B., and Marti K., 1975c. Sm – Nd age and history of Apollo 17 basalt 75075: Evidence for early differentiation of the lunar exterior. Proc. Lunar Sci. Conf. 6th. 1419 – 1429.
25. Macdougall, J,D,, Lugmair, G.W., and Kerridge, J.F., 1984. Early solar system aqueous activity: Sr isotope evidence from the Orgueil C1 meteorite. Nature 307, 249 – 251.
26. Masuda, A., Nakamura, N., Tenaka, T., 1973. Fine structures of mutually normalized rare-earth patterns of chondrites. Geochim. Cosmochim. Acta 37, 239-248.
27. Masuda, A., 1975. Abundances of monoisotopic REE, consistent with Leedey chondrite values. Geochem. J. 9, 183-184.
28. Minster, J.F., Birch, J.L., All`egre, C.J., 1982. Absolute age of formation of chondrites studied by ^{87}Rb/^{87}Sr method. Nature (London) 300, 414-419.
29. Nakamura N., Tatsumoto, M., Nunes, P.D., Unruh, D.M., Schwab, A.P., Wildeman, R.R., 1976. 4.4 b.y. old clast in Boulder 7, Apollo 17: a comprehensive chronological study by U-Pb, Rb-Sr, and Sm-Nd methods. Proc. Lunar Sci. Conf. 7th 7, 2107-29.
30. O'Nions, R.K., Carter, S.R., Evensen, N.M. and Hamilton, P.J., 1979. Geohemical and cosmochemical applications of Nd isotope analysis. Ann. Rev. Earth Planet. Sci. Lett. 7, 11-38.
31. O'Nions, R.K., Hamilton, P.J., Evensen, N.M., 1977. Variations in ^{143}Nd/^{144}Nd and ^{87}Sr/^{86}Sr ratios in oceanic basalts. Earth Planet. Sci. Lett. 34, 13-22.
32. Richard, P., Shimizu, N., and All`egre, C.J., 1976. ^{143}Nd/146Nd , A natural tracer: An application to oceanic basalts. Earth Planet. Sci. Lett. 31, 269-278.
33. Stosch H.-G., and Lugmair, G.W. 1984. Evolution of the lower continental crust: granulite facies xenoliths from the Eifel, West Germany. Nature 311, 368-370.

GRAPHICAL ABSTRACT

A PERSPECTIVE ON THE PREFERRED Sm-Nd ISOTOPIC PARAMETERS FOR THE PLANET EARTH

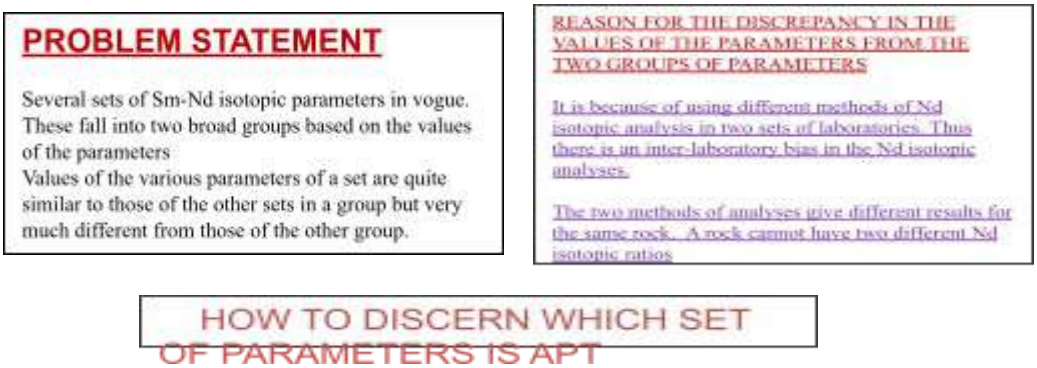

A set of parameters to be considered viable has to meet TWO CONDITIONS

The first condition is that its parameters have to be internally consistent.

The internal consistency involves comparing the measured Nd isotopic ratio of a rock with the one computed from the other reference values. The set of parameters which shows the least difference between the measured ratio and the computed ratio is considered to be internally consistent.

Secondly, that set also has to satisfy the constraints imposed by the present-day Sr isotopic ratio because the latter is derived from the correlation of Nd isotope and Sr isotope ratios of Recent oceanic volcanic rocks.

Similarly from the different sets of Rb-Sr isotopic parameters, the one which is internally consistent is selected.

Thus from amongst the internally consistent sets of Sm-Nd isotopic parameters, the one whose corresponding $^{87}Sr/^{86}Sr$ isotopic ratio matches very closely with the $^{87}Sr/^{86}Sr$ ratio of the independently determined internally consistent set of Rb-Sr isotopic parameters is considered to be the most plausible set of the Sm-Nd isotopic parameters.

CONCLUSION

The values of the most plausible set of Sm-Nd isotopic parameters are, 0.50677, 0.512636, and 0.1936 for the initial $^{143}Nd/^{144}Nd$ ratio, the present-day $^{143}Nd/^{144}Nd$ and the present-day $^{147}Sm/^{144}Nd$ ratio, respectively.

This page is intentionally left blank

Rheological Evidence for a Probable Rarefied Crust and Fracture Characterization under Northern Harrat Rahat, Sw Saudi Arabia: Its Significance for Geothermal Prospects

Manoj Mukhopadhyay, Basab Mukhopadhyay, Saad Mogren & Elkhedr Ibrahim

PNG University of Technology

ABSTRACT

We analysed the geothermal potential in the Northern Harrat Rahat (NHR), SW Saudi Arabia, where, a 'Low-Gravity-Zone' (LGZ) follows the eastern vent axis and also corresponds to a Low Resistive Zone (LRZ) at 10 to 15 km depth. Anomalous crustal rheological parameters (Vp, Vp/Vs, Density, Poisson's ratio, Young's modulus and Acoustic-Impedance) are noticed on 2.5 km depth-slices underlying the LRZ which are based on receiver-function results from 13 seismic stations distributed within an area of 120 x 128 km². Based on these, we inspect crustal rheology under an ENE-WSW traverse taken across the LGZ that unravels finer details of a Low Velocity Zone (LVZ), a Low Density Zone (LDZ), and Low Poisson ratio (σ) and Young's modulus (E) zones in the depth direction over a lateral extent of 120 km at depths between 5 and 17.5 km. Further down, (i) the lower extent of LVZ and LDZ dips eastward from 17.5 to 25 km, suggesting a rarefied crust underneath, and (ii) both Vp and density depth sections illustrate appreciable gradient as they increase from east and west towards the central area beneath the REF seismic stations RH01 and RH14.

Keywords: northern harrat rahat, transitional crust, elastic constants, rheological properties, low-velocity and density zone, geothermal favorability.

Classification: LCC Code: QE509

Language: English

Great Britain Journals Press

LJP Copyright ID: 925614
Print ISSN: 2631-8490
Online ISSN: 2631-8504

London Journal of Research in Science: Natural & Formal

Volume 25 | Issue 2 | Compilation 1.0

Rheological Evidence for a Probable Rarefied Crust and Fracture Characterization under Northern Harrat Rahat, Sw Saudi Arabia: Its Significance for Geothermal Prospects

Manoj Mukhopadhyay[α], Basab Mukhopadhyay[σ], Saad Mogren[ρ] & Elkhedr Ibrahim[Ↄ]

ABSTRACT

We analysed the geothermal potential in the Northern Harrat Rahat (NHR), SW Saudi Arabia, where, a 'Low-Gravity-Zone' (LGZ) follows the eastern vent axis and also corresponds to a Low Resistive Zone (LRZ) at 10 to 15 km depth. Anomalous crustal rheological parameters (Vp, Vp/Vs, Density, Poisson's ratio, Young's modulus and Acoustic-Impedance) are noticed on 2.5 km depth-slices underlying the LRZ which are based on receiver-function results from 13 seismic stations distributed within an area of 120 x 128 km². Based on these, we inspect crustal rheology under an ENE-WSW traverse taken across the LGZ that unravels finer details of a Low Velocity Zone (LVZ), a Low Density Zone (LDZ), and Low Poisson ratio (σ) and Young's modulus (E) zones in the depth direction over a lateral extent of 120 km at depths between 5 and 17.5 km. Further down, (i) the lower extent of LVZ and LDZ dips eastward from 17.5 to 25 km, suggesting a rarefied crust underneath, and (ii) both Vp and density depth sections illustrate appreciable gradient as they increase from east and west towards the central area beneath the REF seismic stations RH01 and RH14. The LVZ, LDZ and Low Poisson Ratio (σ) and Young's Modulus (E) zones under NHR probably owe its origin to a raised geotherm in fractured crust that alters the crustal rheology and shows correspondence to vent axes. Compartmentalization of geophysical properties by orthogonal fractures/faults is used to propose a probable geologic model of heat transfer in the NHR.

Keywords: northern harrat rahat, transitional crust, elastic constants, rheological properties, low-velocity and density zone, geothermal favorability.

Author α σ: PNG University of Technology, Lae, Morobe Province, Papua New Guinea.
σ: Mission III, Geological Survey of India, 29 J. L. Nehru Road, Kolkata – 700016, India.
ρ: King Saud University, P.O. Box 2455, Riyadh 11451, Kingdom of Saudi Arabia.
Ↄ: King Saud University, P.O. Box 2455, Riyadh 11451, Kingdom of Saudi Arabia.

I. INTRODUCTION

The Arabian Shield along the Red Sea Margin (AS-RSM) in SW Saudi Arabia (Figure 1) is tectonically active. It has an average width of 150 km from Red Sea coast and formed by three distinct morphological units: (i) the low-lying coastal plains of median width of 40 km that sustain an elevation up to 100 m, (ii) further inland appears the foothills of the Hijaz-Asir Escarpment Zone (HAEZ), having elevation nearly 500 m and beyond which, (iii) the HAEZ steeply rises to an altitude of 3 km. The area between the shoreline and the HAEZ is occupied irregularly in a wide strip by the basaltic fields (also called harrats) (Brown, 1980). The dominant NNW alignment of the volcanic fields sub-parallel to the regional Red Sea axis were produced by magmatic activity triggered by lithospheric extension. Seismic studies using broadband stations (Tang et al., 2016, 2019) and IRIS seismic profiles (Gettings et al., 1986) identified a low-velocity upper mantle. This low-velocity upper mantle is presumably sourced the magma in the basaltic fields and has a connection with the Afar plume activity (Chang et al., 2011; Lim

et al., 2020; Kaviani et al., 2020; Mukhopadhyay et al., 2022). The intrusive and extrusive magmatic phases that occurred during Tertiary time in SW Saudi Arabia are recognized as the final tectono-magnetic events in the study area (Bohannon, 1989). The AS-RSM is segregated by many regional sutures and faults of different ages (Stern & Johnson, 2010, 2019) and divided AS-RSM into three broad geologic divisions; North Red Sea Margin (NRSM), Central Red Sea Margin including the Jeddah Terrane (CRSM & JT), and South Red Sea Margin (SRSM). However, such divisions are mainly speculated on geological grounds rather than concrete geophysical signatures. The large-scale volcanism along the shield edge in SW Saudi Arabia has presumably altered the elastic constants of crustal rocks. A chronicle in the evolution of the geological framework in the region is: (i) the crust has undergone large-scale extension, (ii) the crust experienced extensive regional volcanism to form the harrats, (iii) non-uniform distribution of volcanic fields; the volcanism is conspicuously absent for 400 km in the central part of AS-RSM, and (iv) consequently, there are expected differences in lithology between the upper and lower crust along such discontinuous volcanic belts spread across the region.

The seismic anisotropy in the AS-RSM transitional crust reveals that the rheological character of the crust underneath the AS-RSM is heterogenous. Here the elastic properties vary both laterally and vertically, exhibiting sharp changes between the magma-infested crustal columns. Seismic attributes (wavelet phases and amplitudes) are related to physical properties of the imaged crustal rocks such as Vp, density (ρ), Poisson's ratio (σ), and acoustic-impedance (AI) etc., as they provide meaningful data for an insight to geothermal prospectivity. It is conjectured that "a lack of magmatic activity does not necessarily imply a lack of geothermal systems" (IGA Service GmbH, 2014). Often deep crustal faults and crust-penetrative fracture zones can also transport heat in a thinned crust like the AS-RSM. Geophysical methods, in particular, seismic, magneto-telluric, and gravity have found wide applications in the search of geothermal systems even within a deep crust (Heise et al., 2007; IGA Services GmbH, 2014).

Geothermal productivity at the AS-RSM in Saudi Arabia has gained importance mostly during the last four decades. The prospectivity is distributed amongst its petrographic divisions (Demange, 1984; Al-Dayel, 1988). This happened mainly because of factors like the uplifted Moho at the extensional margin, high-temperature gradient, enhanced heat flow regime under the basaltic harrats, fractured crust, faults and vent axes (refer below). One such recent publication dealt with the 'geothermal favorability map' for Saudi Arabia where the authors integrated the relevant spatial data on Curie depth, temperature gradient, heat flow, fault density, volcanic field density, and seismic event density (Aboud et al., 2021). The Harrat Rahat (marked as 7 in Figure 1) has a near-surface geothermal magmatic system and was investigated by Aboud et al. (2022, 2023) using the MT survey and gravity–magnetic data. The Northern Harrat Rahat (NHR), the northernmost part of Harrat Rahat, presumably has more geothermal potential. In the present study, we investigate the probable correspondence between the crustal rheological parameters and gravity for NHR and try to locate its potential geothermal zones.

Several site-specific variables that are regarded as quite characteristic of geothermal systems are (a) the mechanical properties of rocks, (b) the nature and depth of the heat source, whether magmatic or non-magmatic; (c) distribution of permeability and porosity; (d) the dominant heat transfer mechanism, whether convection or conduction; (e) chemistry of fluid/rock; and (f) fluid recharge rate/source (Chapter 2 in IGA Service GmbH, 2014). Owing to constraints on the data availability, the scope of the present study is confined to only the areas under (a) and (b). Here our objectives are four folds: (i) to present and analyze the rheological parameters for NHR based on the available REF results, (ii) to infer the probable composition of rock prevalent in the upper and lower crust underlying their respective areas for NHR, (iii) to interpret the gravity anomaly mapped over the NHR, by taking a cue from both the REF results as well the MT survey results which have detected a Low Resistivity Zone

(LRZ) at the mid-crust underlying the NHR, and (iv) integrate these results to examine their applicability in gaining an insight into the geothermal system under NHR.

II. GEOLOGY OF NORTHERN HARRAT RAHAT (NHR)

The Harrat Rahat (marked as 7 in Figure 1) covering ~20,000 km² area is the major volcanic field in western Saudi Arabia whose characteristic features are reviewed here for ready reference to the readers. The volcanic field is nearly 300 km long and has a maximum width of ~ 75 km (Camp & Roobol, 1989, 1991). Actually, four volcanic fields together constitute the Harrat Rahat, namely; Harrat Ar Rukhq, Harrat Turrah, Harrat Bani Abdullah, and Harrat Rashid from south to north. The northernmost volcanic field is the Harrat Rashid / Harrat Al-Madinah / Northern Harrat Rahat (NHR) (Figure 2). Studies by Down et al (2028, 2019) provide an initial estimate on the volumetric percentage of the various basalts erupted within them: Harrat Rahat contains majority as tholeiitic basalt (~62%), followed by alkali basalt (~21%), hawaite (~13%), and mugearite, benmoreite, trachyte (~4%) in diminishing proportion, where the axial part of the field is significantly occupied by a large number of vents containing mugearite and hawaite. In an earlier study, Brown (1980) had also identified three ages of volcanic rocks: (i) basaltic flow of the Tertiary age, (ii) basaltic flow of the Tertiary and Quaternary ages, and (iii) basaltic flow of the Holocene age. It is of interest to note that the identified rocks have prevalent mantle affinity (Murcia et al., 2016).

In NHR, the eruption is through fissures, tuff ridges, shields and pyroclastic cones. The last known eruptive event occurred near Al Madinah at 1256 AD (Camp et al., 1987; Kereszturi et al., 2016). The identified 900+ volcanic vents (Downs et al., 2019) are aligned along two prominent vent axes, western and eastern, with a separation of nearly 10 km in between having a structural trend of N10°W to N25°W (Runge et al., 2014, 2015) (Figure 2). Field mapping by Downs et al. (2018 and 2019) demonstrate identifiable sequences in eruption and subsequent compositional changes associated with it as a part of evolutionary process in NHR. Their sequence being: (i) Tholeiitic basalts with minor amount of alkali basalts erupted in the first phase, (ii) in Pliocene period, the dominant eruptive phase is alkali basalts, and (iii) since the Pleistocene, alkali basalts are accompanying with hawaiite, mugearite, Benmoreite, and trachyte. The flow of the lava flow is rather fast and even reached 100 km from the vent or eruption side in the downslope direction. From the 10 – 15% increase of shear-wave velocity between 15 and 25 km depth, the interface between the andesitic upper crust and the mafic lower crust was identified in the Arabian Shield (Civilini et al., 2019). The average velocities of the upper and lower crust below Harrat Rahat were estimated through Rayleigh waves as 3.64 and 3.95 km/s, and using Love waves as 3.53 and 4.16 km/s (Civilini et al., 2019). From the above analysis, Civilini et al., (2019) concluded that a crustal magma chamber is absent in the region. Hence, it may be prudent to infer from all other evidence cited above that the magma is coming from a deeper source, probably from the elevated Moho region or from the upper mantle. Due to high thermal flow from the source region, high density of structural and fracture planes within crust and suitable fractured eruptive rock types present, the NHR possess a good geothermal potential. In this regard, the readers are referred to a recent compilation on the subject by Al-Amri et al. (2020).

III. MATERIALS AND METHODS

REF data for the 13 numbers of seismic stations (RH01 to RH11, RH13 to RH15) located on NHR (base data: location of station, Vp, Vs, Vp/Vs along 2.5 km depth, Moho depth) are extracted from Tang et al. (2016, 2019) up to a depth of 40 km with a depth interval of 2.5 km. These data are used here to compute the rheological constants (Density (ρ), Lame's First Constant (λ), Shear Modulus (μ), Poisson's Ratio (σ), Young's Modulus (E), Bulk Modulus (K) and Acoustic-Impedance (AI)) using the following equations for the underlying crust. The results are tabulated (Table 1).

The following equations are used for calculation (Brocher, 2005; Telford et al., 1976; Anderson,1989), where V_P is the P wave velocity and V_S is the S wave velocity.

$$\rho = 1.6612V_p - 0.4721V_p^2 + 0.0671V_p^3 - 0.0043V_p^4 + 0.000106V_p^5 \quad (1)$$

$$\lambda = \rho (V_P^2 - 2V_S^2) \quad (2)$$

$$\mu = Vs^2\rho \quad (3)$$

$$K = \lambda + 2/3(\mu) \quad (4)$$

$$E = \mu(3\lambda+2\mu) / (\lambda+ \mu) \quad (5)$$

$$\sigma = 0.8835 - 0.315V_p + 0.0491V_p^2 - 0.0024V_p^3 \quad (6)$$

$$AI = V_p*\rho \quad (7)$$

The crustal thickness for upper and lower crust for the 13 seismic stations located on NHR are taken from Tang et al. (2016, 2019). We have computed the average values of all rheological parameters based on the thickness data of upper and lower crust. The results are tabulated (Table 2).

IV. RESULTS

4.1. General relationship between the rheological parameters in NHR

The primary features of the rheological parameters and their mutual relationships for NHR up to a depth of 40 km (Table 1) is discussed below.

(i) The regression relationship between Vp and Vs is linear and positive, following the regression equation Vs = 0.5714Vp + 0.0001 (R^2 = 1). No relationship can be established between Vp and Vp/Vs. The relationship between Vp and density (ρ) is linear and positive where ρ = 0.2459Vp + 1.2443 (R^2 = 0.985). The regression relation between Vs and density (ρ) is also linear and positive with equation ρ = 0.4303Vs + 1.2443 (R^2 = 0.985).

(ii) Poisson's ratio (σ) usually corresponds to rock deformation developed by static or dynamic stresses at crustal depth. Here we examine the correlation of σ with other relevant elastic properties like; Vp, Vs, Vp/Vs and ρ. The relationship between Vp and σ is linear and positive, σ = 0.0164 Vp + 0.1451 (R^2 = 0.968). The Poisson's ratio attains a value of 0.25 at mid-crustal depth underneath the NHR. The regression relationship between Vs and σ follows a linear and negative pattern, σ = 0.0287 Vs – 0.1451 (R^2 = 0.968). No relationship is seen between Vp/Vs and σ, whereas, the relation between ρ and σ is linear and positive: σ = 0.0671ρ + 0.0613 (R^2 = 0.983).

(iii) A linear relationship is demonstrated by the λ and Vp, λ = 16.28Vp – 63.596 (R^2 = 0.983). The regression relation between Vs and λ is also found to be linear and negative, λ = 28.491Vs – 63.6 (R^2 = 0.983). The relationship between μ and λ is distinctly linear and positive, λ = 0.9411 μ + 0.0027 (R^2 = 1). The same is true for the relationship between μ and ρ for NHR, ρ = 0.0011μ + 0.2092 (R^2 = 0.988). Likewise, the relationship between ρ and λ is linear and negative, λ = 66.3ρ – 146.23 (R^2 = 0.999).

4.2. Rheological properties and inferred crustal rocks under NHR

The variation in Vp/Vs ratio on a regional scale indicates a change in crustal composition. In the crust, an increase in Vp/Vs with depth is directly proportional to a decrease in silica content. In the North American craton, Vp/Vs variation is utilized to map the lithological variation in the crust with depth in two crustal provinces: Grenville Province (average Vp/Vs = 1.81) and the Appalachian Province (average Vp/Vs = 1.73) (Musacchio et al., 1997). Vp/Vs for NHR ranges from 1.740 to 1.750 in the

upper crust and from 1.749 to 1.750 in the lower crust. The Vp versus Vp/Vs relationship is used to identify the rock compositions at 2 and 10 Kba pressures respectively (Musacchio et al., 1997). We infer that the rock composition is mostly uniform and felsic in the upper crust under 2 Kba pressure and mafic in the lower crust under 10 Kba pressure.

The distribution of Poisson's Ratio (σ) values has been used by workers to infer the probable rock types mostly prevalent in the upper and lower crust (Gercek, 2007). The σ value in the upper crust ranges from 0.2357 – 0.2495 and that for the lower crust is from 0.2422 to 0.2748, their corresponding plot on the Gercek diagram infers the prevalence of granodiorite to diorite in the upper crust to a gabbroic lower crust (Figure 3), where the rocks are probably less hydrous (cf. Christensen, 1996).

Ji et al. (2010) have reported a comprehensive database demonstrating the relationships between Vp, Vs and ρ for crustal rocks at 600 MPa based on 401 samples (amphibolite (N=31), peridotite (N=38), serpentinized peridotite (N=15), eclogite (N=54), gabbro, diabase, mafic gneiss and mafic granulite (N=118), granodiorite, diorite, felsic gneiss, intermediate gneiss and meta-sediments (N=145), anorthosite (N=8), basalt (N=21) and limestone/marble (N=29)). When we compare and correlate the plots of Vp – λ, Vs – λ, and ρ - λ of the present study on NHR and that to the regression plot and rock types published in Ji et al. (2010) (Figure 4). We infer a felsic upper crust (with felsic to intermediate gneiss and diorite) and a mafic lower crust (mafic gneiss, amphibolite, gabbro and diabase rocks) underlying the NHR.

The Acoustic Impedance (AI) in rocks when plotted against the depth has proven to indicate the presence of a possible seismic discontinuity in the continental crust. Diaferia and Cammarano (2017) have utilized AI for the case of a three-layered crustal model to understand the source of seismic discontinuity in terms of compositional changes that occurred due to the transition of different mineral phases at depths. Accordingly, the average AI values corresponding to a two-layered crust (after Gettings et al., 1986) in the NHR are plotted (Figure 5). Notice that there are distinct shifts in average AI in four zones (A to D, Figure 5) below NHR.

- A rapid change in average AI from surface to 5 km depth (zone A) is attributed to the basaltic flow rocks and diabase dike sheets within silicic crust.
- Change in average AI at 12 km is the junction between the upper and lower crust (Zone B). The upper mostly silicic crust is ~10 – 12 km thick.
- From 12 km to 32 km (zone C) is the lower crust. The rapid change of AI between the upper and lower crust is possibly due to a phase transition of the quartz. The high-temperature gradient in the NHR favours the transition of α quartz to β quartz, plagioclase breakdown and formation of clinopyroxene, which triggers a sudden increase in AI and also Vp/Vs ratio (cf. Rudnick & Gao, 2014; Diaferia & Cammerano, 2017). Here the inferred rock types are gabbro and mafic gneiss.
- Zone D is the lithospheric mantle with possible high-grade mafic granulite and eclogite.

4.3. Rheological variation in the concentric zones around the low resistive zone in NHR

Four concentric circles are visualized circumventing the peak 'Low Resistive Zone' (LRZ, after Aboud et al., 2023) beneath NHR (Figure 6), centered at 24°20'N, 39°50'E. The LRZ is mapped based on the MT survey (Aboud et al., 2023). The radial concentric zones centered at 24°20'N, 39°50'E, denoted as a – d of Figure 6, have respective radii values up to 10, 40, 55 and 100 km and contain 13 REF seismic stations situated in the NHR (source Tang et al., 2019). The NHR is traversed by NW-trending faults/lineaments. The LRZ orients NE are almost orthogonal to the regional tectonic trend. The inverted model given by Aboud et al. (2023) identifies a main magma chamber at 10 – 15 km depth, with very low resistivity in its interior (3 Ωm). The thermal reservoir is estimated to have a large area extent of ~1000 km² based on gravity-magnetic data analysis (Aboud et al., 2022). The variation of

rheological parameters within the radial zones a - d circumventing the LRZ is analyzed. The upper crust (10 – 15 km thick) has low values of Vp/Vs, density (ρ) and AI within the 10 km zone (Figure 7). The parameters (Vp/Vs, density (ρ) and AI) remain almost constant away from LRZ up to 100 km. Whereas, in the lower crust, an increase in density (ρ) and decrease in Poisson's ratio (σ) is observed away from the LRZ up to 100 km radial distance zone. This is due to the presence of a large magma chamber with more than 1000 km² area extent surrounding LRZ, and accompanied by a high heat flow. The LRZ is associated with a distinct lowering in Vp/Vs, ρ, σ and AI-values compared to surrounding seismic stations. This leads us to inspect the rheological variation in 2.5 km depth slices for the crustal columns in the following section.

4.4. Distribution of crustal rheological parameters and gravity in the region of the vent axes of NHR

4.4.1. Contoured Maps of selective rheological parameters in 2.5 and 5 km depth slices

This is undertaken here by presenting contoured maps of selective rheological parameters (Figures 8 and 9). In the 2.5 km depth slice (Figure 8), the parameters [Vp, Vs, Vp/Vs ratio, Density (ρ), Poisson's ratio (σ), and Acoustic Impedance (AI)] show comparatively a broad arcuate low-value zone trending ENE-WSW to N-S below seismic stations RH13, RH1, RH14, RH9 and RH11 (Figure 8). The broad low-value zones recover with comparatively higher values on both sides towards SE and NW (Figure 8). The arcuate anomalous zone of rheological parameters indicates a highly fractured basement with less density and high-temperature melt zones below NHR. Broadly it refers to the properties of the crustal column beneath NHR. We infer that the crustal column is enriched in mafic content, amenable to deform with moderate/less resistance, and changes its volume under high shear-strain conditions produced by magmatic intrusions from the subcrustal level. The contoured maps of the same rheological parameters at 5 km level (Figure 9) show more restricted low value anomalies encompassing three seismic stations (RH01, RH14 and RH15) below NHR and its extension in the northern part up to RH09. The 'Low Resistive Zone' (LRZ) (Aboud et al., 2023) around seismic station RH1 also coincides with low-value zones of all rheological parameters indicating the presence of high-temperature melt within a 5 km depth zone. The restricted nature of Vp and density (ρ) anomalies along the top 5 km in NHR prompted us to analyse its continuation further down depth along a traverse discussed in the following sections.

4.4.2 The Bouguer anomaly and its relationship with low velocity, low density and low resistivity zones in NHR

The Bouguer anomaly map of NHR (Figure 10) is reported by Langenheim (2018); the map is based on terrain-corrected anomaly for 302 gravity stations. Most conspicuous feature present on the B.A. map is an axial gravity low running in NNW-SSE direction through the NHR with flanking gravity highs. The Axial Gravity Low also extends northward over the surrounding Proterozoic basement rocks outside the harrat, suggesting its deep crustal origin (Langenheim et al., 2019). Figure 10 illustrates an intimate correspondence of the Axial Gravity Low with the eastern vent axis, though this correlation is less clear for the western vent.

We further explore the connection between the gravity anomalies with the distribution of four rheological parameters Vp, density, Poisson Ratio (σ) and Young's Modulus (E) to a depth of 40 km along a traverse A-A' perpendicular to the central low gravity zone (see location of A – A' section in Figure 10). The distribution of Vp, density, σ, and E along depth (up to 40 km) for five seismic stations (RH05, RH13, RH01, RH14 and RH02) in the ENE-ESE direction are illustrated along with gravity profile for traverse A-A' (Figures 11 & 12). The zone of low gravity unravels a Low Velocity Zone (LVZ), a Low Density Zone (LDZ), a Low Poisson Ratio (σ) and Young's Modulus (E) zones at crustal depths of

5 to 17.5 km; all these are based on 2.5 km depth slices (Figure 11 & 12). The lower extent of LVZ, LDZ, Low Poisson Ratio (σ) and Young's Modulus (E) zones dips eastward from 17.5 km to 25 km across a lateral extent of 120 km underlying the traverse where gravity low is envisaged for 90 km between RH13 and RH2. This result also implies that the eastern vent axis is more deep-rooted than the western vent axis in NHR. Broadly it refers to the properties of the crustal column which is highly fractured beneath the low gravity zone. The low Poisson Ratio (σ) and Young's Modulus (E) are places where the rocks are hydraulically fractured due to high strain and transmit the heat to raise geotherm (see also Lees and Wu, 2000; Head et al. 2021). The lower crust here is with low silica and high mafic contents, and deforms in moderate/low resistance with volume changes under high-strain produced from intrusions of magmatic dykes from mantle. Thus, the fractured crustal column is dyke-invaded and carries magmatic material through deep-seated faults from a magma chamber probably residing in deep crust. The faults with multiple channels on the upper part of the crustal column produce the LVZ, LRZ (with very low resistivity 3 Ωm in its interior as documented by Aboud et al., 2023) and LDZ. These faults in turn have produced vents on the top surface to outpour basaltic magmas. In this scenario, the vent axes coincide with the low gravity anomaly (Figures 10, 11 and 12). The magma to our understanding is produced by partial melting in the mafic crust and is presumably related to Afar plume activity. We opined earlier also that the gravity axial low zone in NHR is regarded as the probable locale for fractured dyke invaded crust which acts as a feeder zone; where a raised thermal regime heralded gross compositional changes in the lower crust in consequence of crust-mantle interaction (Mogren et al., 2021).

V. DISCUSSION

5.1. Rheological properties, gravity and its relation to the geothermal system in NHR

The tectonically active crust under the Arabian Shield Edge along the Red Sea Margin (AS-RSM) in SW Saudi Arabia has gained attention in recent years due to its geothermal potential. Of particular interest in the region is NHR, where two NNW-trending parallel vent axes separated by a distance of ~10 km are mapped (Figure 2). Earlier studies have reported a prominent LGZ (Figure 10) which follows the eastern vent axis, although this correlation is less clear for the western vent axis. The low gravity zone displays moderate to fair correspondence to a LRZ previously detected by MT surveys under NHR at 10-15 km depth. The average velocities are low for both Raleigh (3.64 -3.95 km/s) and Love (3.53 - 4.16 km/s) waves from the upper to lower crust which supports a low-velocity zone underneath the Large Igneous Province (LIP) in Saudi Arabia.

In the earlier sections, we inspected the LGZ by using the rheological parameters of 13 REF seismic stations data and found that the distribution of average rheological parameters in upper and lower crustal columns does not discriminate the crust underneath the low gravity zone as compared to the surrounding crust out-to-a-radial-zone of 100 km circumventing it. This inference radically improves when the rheological properties are inspected in 2.5 km depth slices for the upper and lower crust as illustrated by a traverse A-A', constrained by five numbers of REF seismic stations, taken in ENE-WSW direction across the LGZ. Here most conspicuously, a LVZ, LDZ, a Low Poisson Ratio (σ) and Young's Modulus (E) zones persist across a lateral extent of 120 km at crustal depths of 5 - 17.5 km. Further down the section, the lower extent of LVZ, LDZ, a Low Poisson Ratio (σ) and Young's Modulus (E) dips eastward from 17.5 km to 25 km, whose overall pattern suggests a rarefied crust underneath the region. The Vp and density in depth section illustrate appreciable gradients as they increase both from east and west towards the central area (situated beneath the seismic stations RH01 and RH14). The envisaged LVZ, LDZ, and Low Poisson Ratio (σ) and Young's Modulus (E) zones for the upper to mid-crust under NHR probably owe its origin to a raised geotherm and highly fractured nature of crust producing

alteration in crustal rheology, where the vent axes are reflected on gravity data collected by USGS (Downs et al., 2019).

5.2. Relevance of existing fault systems in NHR and its geothermal favorability

Different approaches have been used in seismic surveys to infer the potentiality of the geothermal fields; examples are the stress-depth distribution (Kusznir et al. 1991), the change in Vp/Vs ratio (Casertano et al., 1980; Kasahara et al., 2020; Lin, 2020; Muluneh et al., 2021) constructed the Yield Strength Envelopes (YSE) to examine the Brittle – Ductile Transition (BDT) by using the information on the geothermal gradient, crustal composition (wet quartzite for the upper crust and granulite for the lower crust) and strain-rate constrained by geophysical observations. Crustal rheological properties also act as meaningful indicators in geothermal resource mapping. The geothermal resource database in a GIS environment has been presented for Saudi Arabia by Aboud et al. (2021). The spatial datasets involve the Curie depth (km), Temperature gradient (°C/km), Heat flow (mW/m²), Fault density, Volcanic field density, and Seismic event density and are useful for identifying areas for geothermal potential.

The Najd Fault System (NFS) is the most conspicuous fault in the whole region, displaying left-lateral shear, which crosses the NHR in the NW-SE direction. Other faults and fractures developed in the area maintain a sympathetic trend to NFS (Figure 13a). No less prosperous are the NE-trending set of secondary faults and fractures in the region which are transverse to NFS (Trippanera et al., 2019); their origin has been ascribed mainly to the Red Sea transforms. The mutually high-angle faults present in NHR provide effective passage for geothermal heat and fluid transmission from deeper to shallower depths. These fault zones usually act as conduits, barriers, or a combined conduit-barrier system for heat and fluid transmission. The heat transmission also depends on the architecture of the fault and rock materials present in the fault zone (Caine et al., 1996). It has been reported by studies elsewhere that the geometrical fracture pattern along a wellbore increases the connection between the borehole and the nearly vertical fracture network associated with a local fault, wherever present (Vidal et al., 2017). An important conclusion derived from their study was to establish a good characterization of zones of fractures in a targeted natural reservoir that may allow an optimal exploitation of geothermal resources. However, no deep geothermal drilling data are available for NHR, save for some shallow-depth geohydrologic boreholes. Al-Shaibani (2003) reported results based only on a handful of shallow-depth geohydrologic boreholes drilled into the Madinah basaltic terrain in NHR. The lithology encountered as well as the stratigraphy based on the drilling for the fractured vesicular basalts for nearly 60m depth is illustrated in Figure 13b. Here, the general groundwater flow is directed to N – NNE, in a direction coincident with the Ayn er Zerqa springs to the south of Al-Madinah city where the sub-basalt flow is through alluvium layers (Al-Shaibani, 2003). Such faults are likely amenable to fluid flow due to high transmissivity in the source material. A conceptual model (Figure 13c) of the fracture system in the Al Madinah basaltic field is prepared where the NFS is intersected by orthogonal normal faults. This fault system is amenable to fluid flow due to high transmissivity in the source material (Table 3 for pumping test data). Mode of heat transfer by local fault systems, streams or springs is generally by conduction (Vidal et al., 2017). A schematic sectional model of the major permeable fracture zone identified from borehole stratigraphy in NHR where fractures in vesicular basalt, in particular within the thick pile of Madinah basalt, are speculated (Figure 13d). These fractures act as a medium of fluid flow and heat transmission. Geothermal drill data are therefore essential to improve our understanding of the transmission of heat by conduction to the surficial crust.

VI. CONCLUSIONS

We examined the potential geothermal prospect of NHR by investigating; (i) crustal rheological parameters derived from REF results, (ii) subsurface configuration of the low resistive zone detected by MT surveys, and (iii) seismic data on the depth horizons for the upper and lower crust based on REF seismic stations by constructing 2.5 km depth slices, (iv) present and analyze the elastic constants computed for the upper and lower crustal columns namely; Vp, Vp/Vs, ρ, σ and AI etc. and (v) gravity and rheological anomalies.

The main results derived from the study in NHR are:

(i) The values for Vp/Vs, ρ, σ and AI are significantly lower below NHR with respect to the surrounding crust due to high heat flow.
(ii) The GLZ over NHR bears a close relationship with the eastern vent axis extending regionally in the NNW-SSE direction and magma chamber.
(iii) Depth slices of rheological parameters along a traverse taken across the zone of GLZ unravels LVZ, LDZ, a Low Poisson Ratio (σ) and Young's Modulus (E) zones at crustal depths of 5 to 17.5 depth beneath the western vent axis which increases to 25 km depth toward the eastern vent axis. This result may be taken to imply a deeper root for the eastern vent axis as compared to the western vent axis.
(iv) It is beyond the purview of the present study to explain the origin of the rarefied crust in the region of the vent axes under northern Harrat Rahat. We can only speculate that it probably owes its origin to partial melting in the crust, related to the Afar plume.
(v) A conceptual geologic model is proposed for heat transfer in the geothermal system of NHR, in particular reference to the vesicular basalt unit in the Al Madinah volcanic field. Orthogonal fractures/faults crossing NHR are envisaged to play a significant role in heat transfer.

ACKNOWLEDGEMENT

Three of us (M.M., S.M. and E.I.) extend our appreciation to the Research Supporting Project number RSP 2023/R325, King Saud University, Riyadh, Saudi Arabia.

Statements & Declarations

Funding

The authors declare that no funds, grants, or other support were received during the preparation of this manuscript.

Competing Interests

The authors have no relevant financial or non-financial interests to disclose.

Author Contributions

All authors contributed to the study conception and design. Material preparation, data collection and analysis were performed by Manoj Mukhopadhyay and Basab Mukhopadhyay. The first draft of the manuscript was written by Manoj Mukhopadhyay and Basab Mukhopadhyay, and all authors commented on previous versions of the manuscript. All authors read and approved the final manuscript.

Data availability

Data used in the analysis of the rheological properties across NHR are already added in Tables 1 to 3 and included in the manuscript.

REFERENCES

1. Al-Amri, A., Abdelrahman, K., Mellors, R., & Harris, D. (2020). Geothermal potential of Harrat Rahat, Northern Arabian Shield: Geological constraints. *Lawrence Livermore National Laboratory, U.S.A., LLNL-JRNL-815125*, 1- 21.
2. Aboud, E., Qaddah, A., Harbi, H., & Alqahtani, F. (2021) Geothermal Resources Database in Saudi Arabia (GRDiSA): GIS model and geothermal favorability map. *Arabian J. Geosci., 14*, 112. https://doi.org/10.1007/s12517-020-06426-z.
3. Aboud, E., Alqahtani, F., Elmasry, N., Abdulfarraj, M., & Osman, H. (2022). Geothermal anomaly detection using potential field geophysical data in Raahat volcanic field, Madinah, Saudi Arabia. *J. Geol. Geophys., 11(4)*, 1026.
4. Aboud, E., Arafa-Hamed, T., Alqahtani, F., Marzouk, H., Elbarbary, S., Abdulfaraj, M., & Elmasry, N. (2023) The geothermal magmatic system at the northern Rahat volcanic field, Saudi Arabia, revealed from 3D magneto telluric inversion. *J. Volcano. Geotherm. Res., 437*, 107794.
5. Al-Dayel, M. (1988). Geothermal resources in Saudi Arabia. *Geothermics 17(2)*, 465–476. https://doi.org/10.1016/0375-6505(88)90076-4.
6. Al-Shaibani, A.M. (2003). Lava fields as potential groundwater sources in Western Saudi Arabia. In Sherif, Singh, & Al-Rashed (Eds.), *Hydrology & Water Resources*. Swets & Zeitinger, Lisse, ISBN 90 5809 548 7.
7. Anderson, D.L. (1989) *Theory of the Earth*. Blackwell Scientific Publications, Boston, USA. http://resolver.caltech.edu/CaltechBOOK:1989.001.
8. Bohannon, R.G., Naeser, C.W., Schmidt, D.L., & Zimmermann, R.A. (1989) The timing of uplift, volcanism, and rifting peripheral to the Red Sea: A case for passive rifting? *Journal of Geophysical Research, 94*, 1683–1701. https://doi.org/10.1029/JB094iB02p01683.
9. Brocher, T.M. (2005). Empirical relations between elastic wave speeds and density in the earth's crust. *Bull. Seism. Soc. Am., 95*, 2081-2092.
10. Brown, G.F. (1980). Physiographic Provinces of the Arabian Peninsula, *U. S. Geological Survey Prof. Paper 560-A, Plate 3, Scale 1: 4 000 000*. Min. Pet. Min. Resources, Kingdom of Saudi Arabia.
11. Caine, J. S., Evans, J. P., & Forster, C. B., (1996). Fault zone architecture and permeability structure. *Geology, 24(11)*, 1025–1028, https://doi.org/10.1130/0091-7613(1996)024<1025:FZAAPS>2.3.CO;2.
12. Camp, V.E., Hooper, P.R., Roobol, M.J., & White, D.L., (1987). The Madinah eruption, Saudi Arabia: magma mixing and simultaneous extrusion of three basaltic chemical types. *Bull. Volcanology 49*, 489–508.
13. Camp, V.E., & Roobol, M.J., (1989). The Arabian continental alkali basalt province: Part I. Evolution of Harrat Rahat, Kingdom of Saudi Arabia. *Geo. Soc. Am. Bull. 101*, 71–95.
14. Camp, V.E., & Roobol, M.J., (1991). Geologic map of the Cenozoic lava field of Harrat Rahat, Kingdom of Saudi Arabia: Ministry of Petroleum and Mineral Resources, Directorate General of Mineral Resources, 1 map sheet, 37 p.
15. Camp, V.E., & Roobol, M.J., (1992). Upwelling asthenosphere beneath Western Saudi Arabia and its regional implications. *J. Geophys. Res. 97*, 15255-15271.
16. Casertano, L., & Del Castillo, A. O., (1980) Vp/Vs ratio and its changes in the Travale geothermal field. In: S. Strub et al., (Eds.), *Advances in European Geothermal Research* © ECSC, EEC, EAEC, Brussels and Luxembourg.

17. Christensen, N.I., (1996) Poisson's ratio and crustal seismology. *J. Geophys. Res., 101*, 3139-3156.
18. Christensen, N. I., & Mooney, W. D., (1995) Seismic velocity structure and composition of the continental crust: A global view. *J. Geophys. Res., 100*, 9761 – 9788.
19. Civilini, F., Mooney, W.D., Savage, M.K., Townend, J., & Zahran, H., (2019). Crustal imaging of northern Harrat Rahat, Saudi Arabia, from ambient noise tomography. *Geophys. J. Int., 219*, 1532–1549. https://doi.org/10.1093/gji/ggz380
20. Coleman, R.G., Gregory, R.T., & Brown, G.F., (1983). Cenozoic volcanic rocks of Saudi Arabia. *U.S. Geological Survey Open-File Report OF-03-83*, 1-82.
21. Chang, S.J., Merino, M., Van der Lee, S., Stein, S., & Stein, C.A. (2011). Mantle flow beneath Arabia offset from the opening Red Sea. *Geophys. Res. Lett. 38*, L04301. https://doi.org/10.1029/2010gl045852.
22. Demange, J., (1984). Drilling for geothermal resources in Harrat Khayber region. *Technical report, Deputy Ministry for mineral resources, Ministry of Petroleum and Mineral Resources*, Riyadh.
23. Diaferia, G., & Cammarano, F., (2017). Seismic signature of the continental crust: What thermodynamics says. An example from the Italian Peninsula. *Tectonics 36*, 3192-3208. https://doi.org/10.1002/2016TC004405.
24. Downs, D.T., Stelten, M. E., Champion, D. E., Dietterich, H. R., Nawab, Z., Zahran, H., Hassan, K. & Shawali, J., (2018). Volcanic history of the northernmost part of the Harrat Rahat volcanic field, Saudi Arabia. *Geosphere, 14*, 1253–1282. https://doi.org/10.1130/GES01625.1
25. Downs, D.T., Robinson, J.E., Stelten, M.E., Champion, D.E., Dietterich, H.R., Sisson, T.W., Zahran, H., Hassan, K. & Shawali, J., (2019). Geologic Map of the Northern Harrat Rahat Volcanic Field, Kingdom of Saudi Arabia. *Scientific Investigations Map 3428, as Saudi Geological Survey Special Report SGS–SP–2019–2*, https://doi.org/10.3133/sim3428
26. Gercek, H., (2007). Poisson's ratio values for rocks. *Int. J. Rock Mechanics & Mining Sci.*, 44, 1-13.
27. Gettings, M. E., Blank Jr., H. R., Mooney, W.D. & Healey, J.H., (1986). Crustal structure of southwestern Saudi Arabia. *J. Geophys. Res. 91*, 6491-6512.
28. Head, M., Hickey, J., Gottsmann, J., & Fournier, N. (2021). Exploring the impact of thermally controlled crustal viscosity on volcanic ground deformation. Journal of Geophysical Research: Solid Earth, 126, e2020JB020724. https://doi.org/10.1029/2020JB020724
29. Heise, W., Bibby, H.M., Caldwell, T.G., Bannister, S.C., Ogawa, Y., Takakura, S., & Uchida, T., (2007). Melt distribution beneath a young continental rift: the Taupo Volcanic Zone, New Zealand. *Geophys. Res. Letters, 34(14)*, L14313. https://doi.org/10.1029/2007GL029629
30. IGA Service GmbH, 2014. Best Practices Guide for Geothermal Exploration. C. Harvey, C. (Eds.), *GmbH, Bochum Univ., Germany*, 1- 196.
31. Italconsultant, (1979). Detailed investigation of the Medinah Region. *Final report, Thematic report no. 7*, Saudi Arabian Ministry of Agriculture and Water, Riyadh.
32. Jakobsson, S.P., Jonasson, K. & Sigurdsson, I.A., (2008). The three igneous rock series of Iceland. *JOKULL, 58,* 117-138.
33. Ji, S., Sun, S., Wang, Q., & Marcotte, D., (2010). Lame' parameters of common rocks in the Earth's crust and upper mantle. *J. Geophys. Res. 115*, B06314. https://dx.doi.org/10.1029/2009JB007134.
34. Kasahara, J., Hasada, Y., & Kuzume, H., (2020). Possibility of high Vp/Vs zone in the geothermal field suggested by the P-to-S conversion. *Proc. 45th Workshop Geoth. Reservoir Eng., Stanford Univ., California, Feb. 10-12, 2020*, SGP-TR-216 1.
35. Kaviani, A., Paul, A., Moradi, A., et al., (2020). Crustal and uppermost mantle shear wave velocity structure beneath the Middle East from surface wave tomography. *Geophys. J. Int. 221*, 1349–1365.
36. Kusznir, N. J., Vita-Finzi, C., Whitmarsh, R.B., England, P., Bott, M.H.P., Govers, R., Cartwright, J. & Murrell, S., (1991). The distribution of stress with depth in the lithosphere: thermos-rheological and geodynamic constraints. *Phil. Trans.: Physical Sci. Eng., 337 (1645), Tectonic Stress in the Lithosphere*, 95-110. URL:https://www.jstor.org.stable/53683

37. Kereszturi, G., Nemeth, K., Moufti, M. R. H., Cappello, A., Murcia, H., Ganci, G., Negro, C. D., Procter, J., & Zahran, H. M. A., (2016). Emplacement conditions of the 1256 AD Al-Madinah lava flow field in Harrat Rahat, Kingdom of Saudi Arabia - Insights from surface morphology and lava flow simulations. *J. Volcano. Geothermal Res. 309*, 14-30.
38. Langenheim, V.E., (2018). Gravity and physical property data of the northern Harrat Rahat, Saudi Arabia. *In: U.S. Geological Survey Data Release*, https://doi.org/10.5066/P9THCSE8.
39. Langenheim, V.E., Ritzinger, B.T., Zahran, H., Shareef, A., & Al-dahri, M., (2019). Crustal structure of the northern Harrat Rahat volcanic field (Saudi Arabia) from gravity and aeromagnetic data. *Tectonophys., 750*, 9-21.
40. Lim, J-A., Chang, S-J., Mai, P.M., & Zahran, H., (2020). Asthenospheric flow of plume material beneath Arabia inferred from S wave travel time tomography. *Journal of Geophysical Research Solid Earth 125*, e2020JB019668. https://doi.org/10.1029/2020JB019668.
41. Lees, J. M. & Wu, H. (2000) Poisson's ratio and porosity at Coso geothermal area, California. Journal of Volcanology and Geothermal Research 95, 157–173.
42. Lin, G., (2020). Spatio temporal variations of in situ Vp/Vs ratio within the Salton Sea Geothermal Field, southern California. *Geothermics, 84*, 101740. https://doi.org/10.1016/j.geothermics. 2019.101740.
43. Mogren, S., Mukhopadhyay, B., Mukhopadhyay, M., Nandi, B.K., & Ibrahim, E. (2021). Spatial distribution of the rheological heterogeneities at crustal depths underneath the Harrat Rahat, western Saudi Arabia and their correspondence to Bouguer anomalies. *Journal of Volcanology and Geothermal Research 419*, 107387.
44. Muluneh, A. A., Keir, D. & Corti, G., (2021). Thermo-rheological properties of the Ethiopian lithosphere and evidence for transient fluid induced lower crustal seismicity beneath the Ethiopian rift. *Front. Earth Sci., 9*, 610165. https://doi.org/10.3389/feart.2021.610165
45. Musacchio, G., Mooney, W.D., Luetgert, J. H., & Christensen, N. I. (1997). Composition of the crust in the Grenville and Appalachian Provinces of North America inferred from VP/Vs ratios. *J. Geophys. Res. 102*, 15225-15241.
46. Murcia, H., Lindsay, J.M., Németh, K., Smith, I.E.M., Cronin, S.J., Moufti, M.R.H., El-Masry, N.N., & Niedermann, S., (2016). Geology and geochemistry of Late Quaternary volcanismin northern Harrat Rahat, Kingdom of Saudi Arabia: Implications for eruption dynamics, regional stratigraphy and magma evolution. In: Németh, K., Carrasco-Núñez, G., ArandaGómez, J.J., Smith, I.E.M. (Eds.), Monogenetic Volcanism. *Geo. Soc. London Spl. Publn. 446*, 173–204. https:// doi .org /10 .1144 /SP446.2.
47. Mukhopadhyay, M., Mukhopadhyay, B., Mogren, S., Nandi, B.K., & Ibrahim, E., (2022). Regional significance of crustal and sub-crustal rheological heterogeneities beneath the Harrat Lunayyir and their continuity into the neighboring harrats, Western Saudi Arabia – Perspectives of the Afar plume activity. *Journal of African Earth Sciences 186*, 104432.
48. Runge, M.G., Bebbington, M.S., Cronin, S.J., Lindsay, J.M., Kenedi, C.L., & Moufti, M.R.H., (2014). Vents to events: Determining an eruption event record from volcanic vent structures for the Harrat Rahat, Saudi Arabia. *Bulletin of Volcanology 76*. https:// doi .org /10 .1007/s00445 -014-0804-z.
49. Runge, M.G., Bebbington, M.S., Cronin, S.J., & Moufti, M.R., (2015). Sensitivity to volcanic boundary. *J. App. Volcanology 4*, 22. https://doi.org/10.1186/s13617.015-0040-z.
50. Rudnick, R. L., & Gao, S., (2014). Composition of the continental crust. In: Holland, H. D., Turekian, K. K. (Eds) *Treatise on Geochemistry, The Crust 3, 1st edition*, Elsevier-Pergamon, 1-64.
51. Schmidt, D.L., & Hadley, D.G., (1985). Stratigraphy of the Miocene Baid formation, southern Red Sea coastal plain, Kingdom of Saudi Arabia. *U. S. Geological Survey OFR 85-241*.
52. Stern, R.J., & Johnson, P., (2010). Continental lithosphere of the Arabian Plate: A geologic, petrologic, and geophysical synthesis. *Earth Sci. Reviews. 101*, 26-67.

53. Stern, R. J., & Johnson, P.R., (2019). Constraining the opening of the Red Sea: Evidence from the Neoproterozoic margins and Cenozoic magmatism for a volcanic rifted margin. In: Rasul, N., Stewart, I. (Eds.), *Geological Setting, Palaeoenvironment and Archaeology of the Red Sea*. Springer, Cham. https://doi.org/10.1007/978-3-319-99408-6_19.
54. Tang, Z., Julia, J., Zahran, H. & Mai, P. M., (2016). The lithospheric shear-wave velocity structure of Saudi Arabia: Young volcanism in an old shield. *Tectonophys., 680*, 8-27. https://dx.doi.org/1.1016/j.tecto.2016.05.004
55. Tang, Z., Mai, P. M., Julià, J. & Zahran, H., (2019). Shear velocity structure beneath Saudi Arabia from the joint inversion of P and S wave receiver functions, and Rayleigh wave group velocity dispersion data. *J. Geophys. Res. Solid Earth 124*, 4767-4787. https://doi.org/10.1029/2018JB017131
56. Telford, W. M., Geldart, L. P., Sheriff, R. E., & Keys, D. A., (1976). *Applied Geophysics*, Cambridge Univ. Press, Cambridge, U.K.
57. Trippanera, D., Ruch, J., Passone, L. & Jonsson, S., (2019). Structural mapping of dike-induced faulting in Harrat Lunayyir (Saudi Arabia) by using high resolution drone imagery. *Frontiers in Earth Sci., 7*, 168. doi: 10.3389/feart.2019.00168.
58. Vidal, J., Genter, A. & Chopin, F., (2017). Permeable fracture zones in the hard rocks of the geothermal reservoir at Rittershoffen, France. *J. Geophys. Res. Solid Earth, 122*, 4864-4887. https://doi.org/10.1002/2017JB014331.

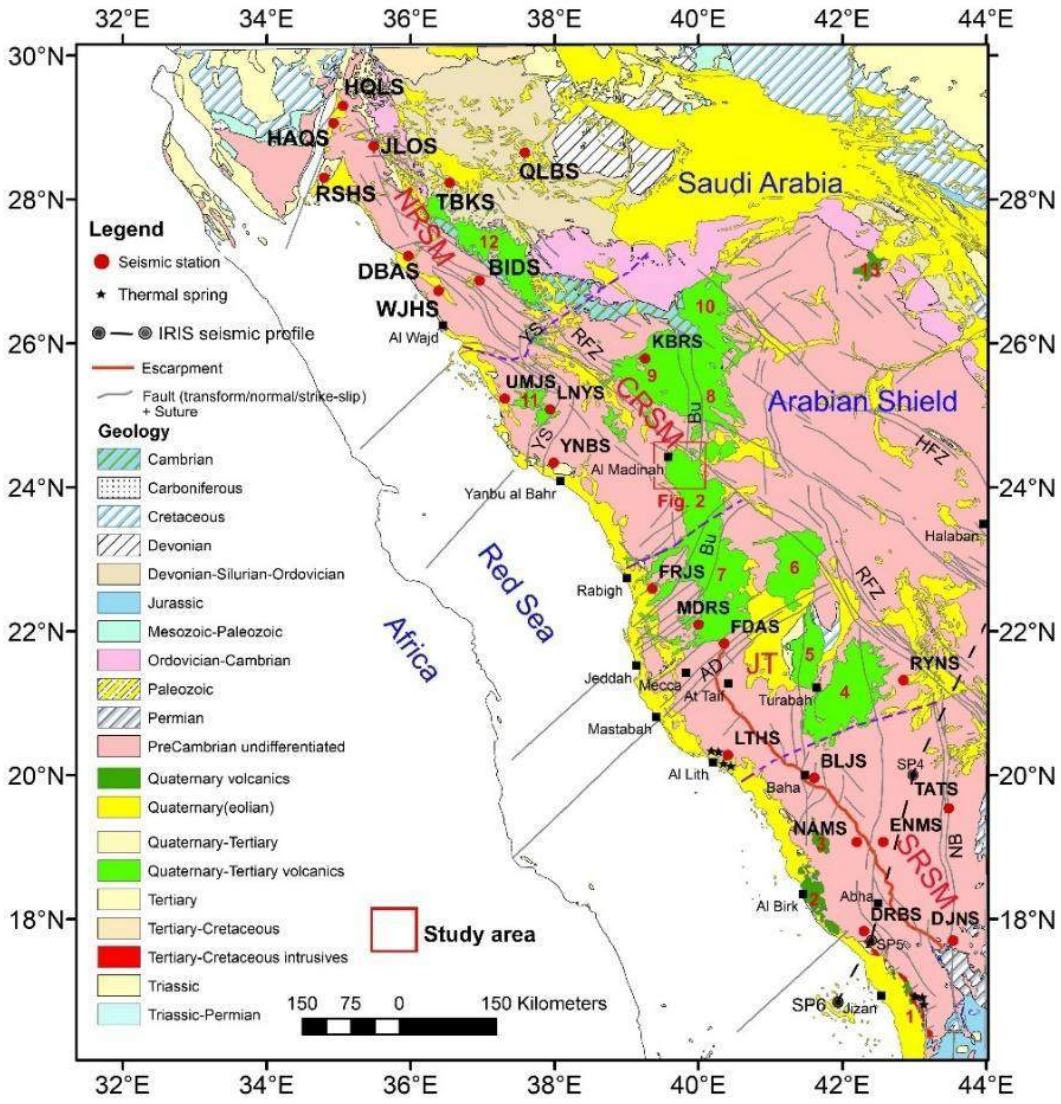

Figure 1: General geological map showing the Arabian Shield with Cenozoic volcanic fields in the Large Igneous Province of Saudi Arabia, adopted from Coleman et al. (1983) and USGS. The Arabian Shield along the Red Sea Margin (AS-RSM) are tectonically subdivided into three segments: North Red Sea Margin (NRSM), Central Red Sea Margin (CRSM) and Jeddah Terrane (JT), and Southern Red Sea Margin (SRSM). The Great Escarpment at the Arabian Shield margin in SW Saudi Arabia is after Schmidt and Hadley (1985). The location of seismic shot points done by USGS with numbers SP 5 to SP 4 (Gettings et al., 1986) is shown. The location of some broadband seismic stations in this terrain after Tang et al. (2016) is plotted. The detailed study area in the Northern Harrat Rahat within CRSM is boxed and its geological map in Figure 2. The harrats (in shades of green) in the Saudi Arabia LIP with their eruption age - 1: Tihama Asir (25-21 Ma), 2: Al Birk (4-0 Ma), 3: As Sirat (30 – 25 Ma), 4: Al Buqum (9-0Ma), 5: Hadan (28 – 25 Ma), 6: Al Kishb (2-0 Ma), 7: Rahat (10 – 0 Ma), 8: Khaybar (5-0 Ma), 9: Kura (11-5 Ma), 10: Ithnayn (3-0) Ma, 11: Lunayyir (1-0 Ma), 12: Uwayrid (9-0 Ma), and 13:Hutaymah (1.8 Ma). AD: Ad Damm Shear Zone, Bu: Bl'rUmq Suture Zone, HFZ: Halaban Fault Zone, RFZ: Rika Fault Zone, NB: Nibita Shear Zone, YS: Yanbu Shear Zone.

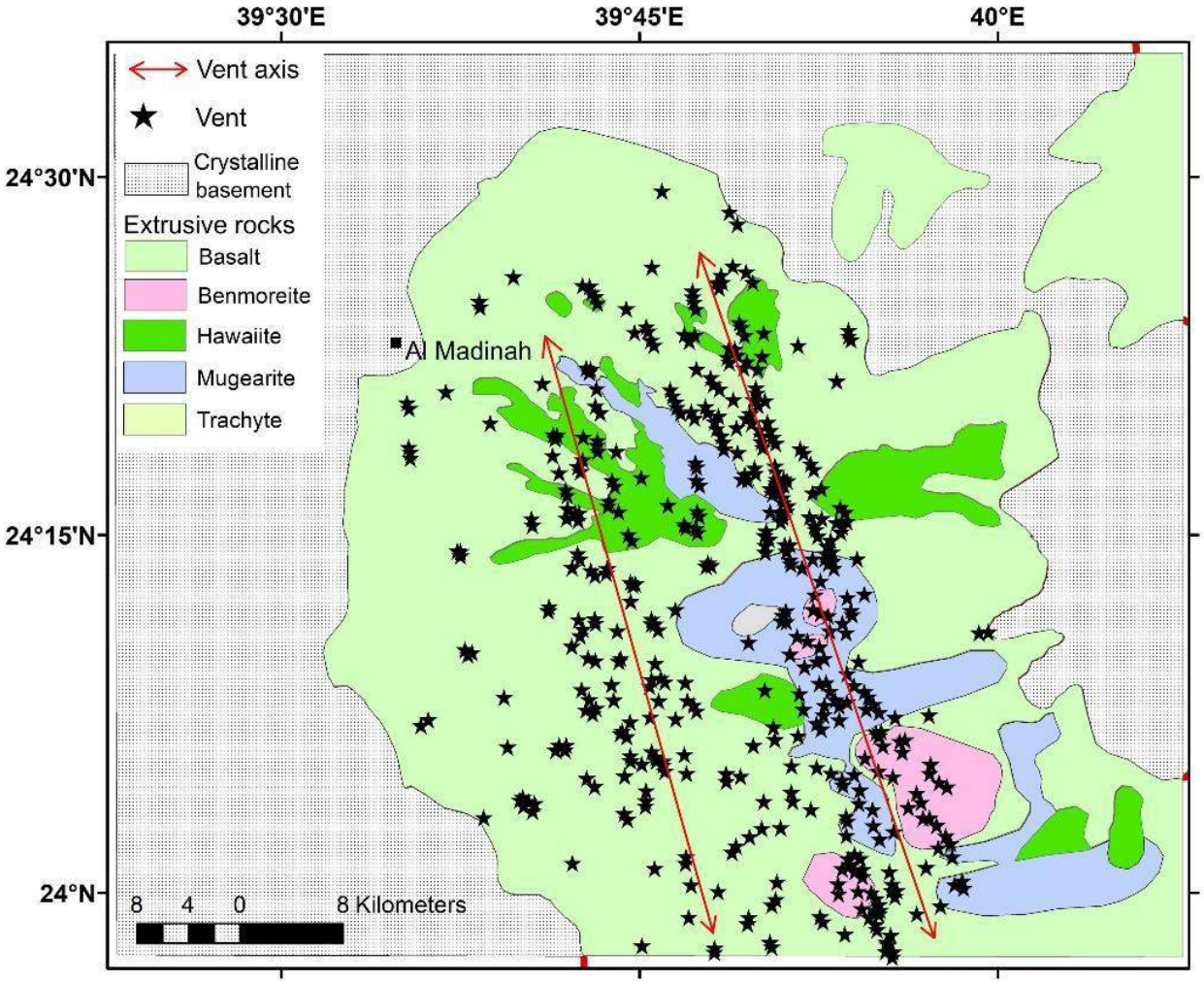

Figure 2: Geological map for Northern Harrat Rahat that forms the largest Cenozoic volcanic field hosted in Saudi Arabia (after Downs et al., 2019). Basalts and other eruptive rock types are shown by different colors and indexed. Red lines with arrows show locations and trends of vent axes across the Northern Harrat Rahat; they maintain a separation by ~10 km.

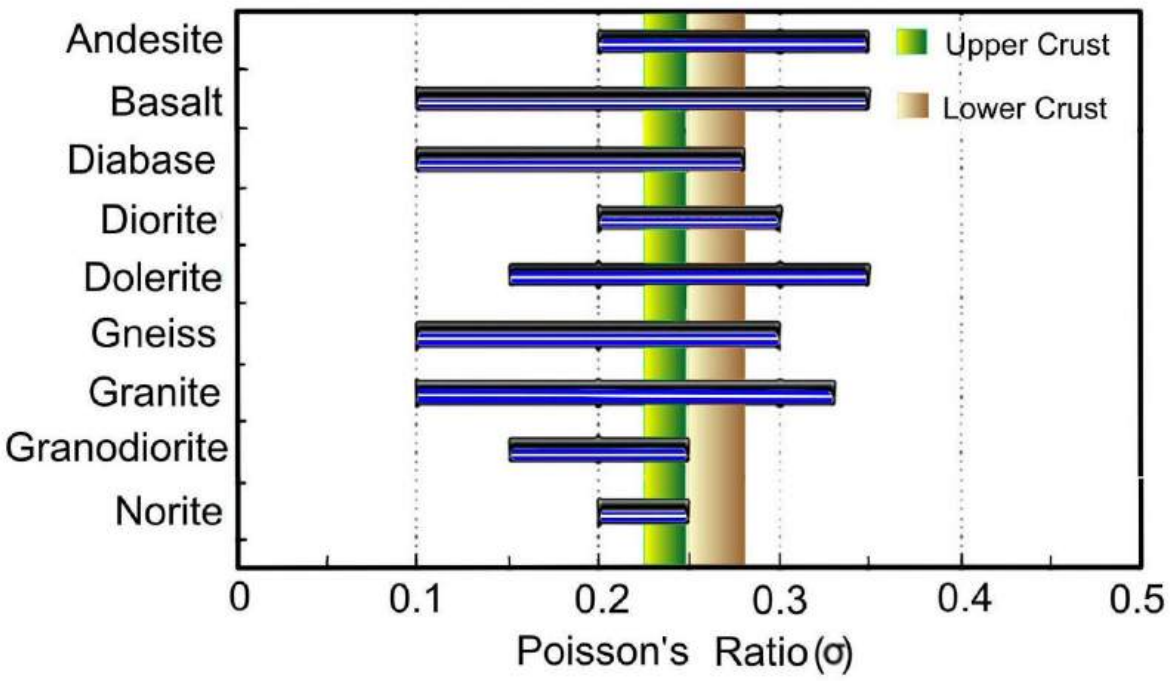

Figure 3: Typical range of values of Poisson's ratio (σ) for common rock types; redrawn after Gercek (2007). The σ values for the upper and lower crust obtained in the Northern Harrat Rahat are superposed on the bar diagram for identification of possible rock type. We infer granodiorite to diorite in the upper crust and a gabbroic lower crust.

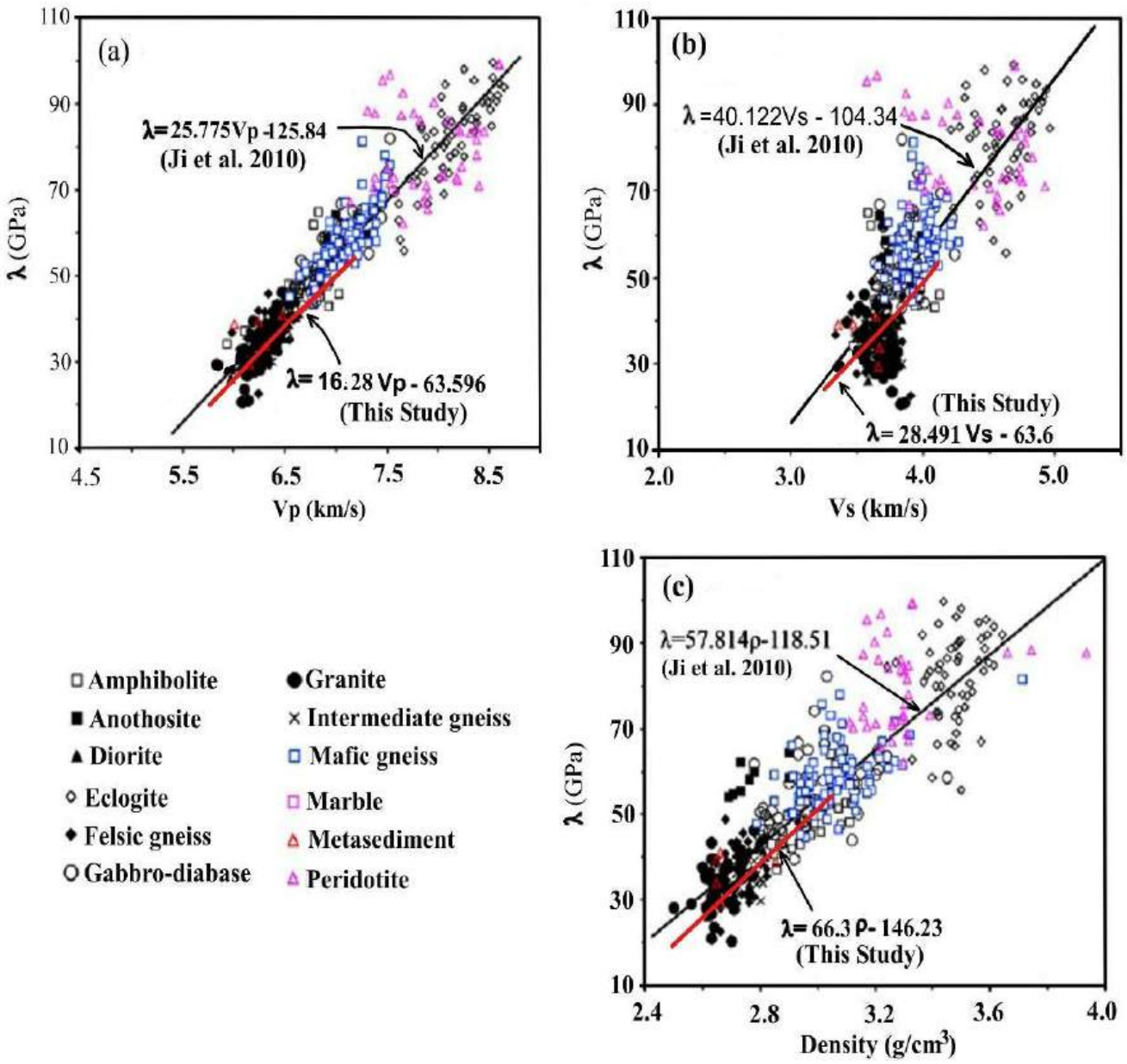

Figure 4: Relationships between Vp, Vs and ρ with λ for crustal rocks at a hydrostatic pressure of 600 MPa for 401 samples reported by Ji et al. (2010). The distribution of the regression relations [(a) Vp - λ, (b) Vs - λ, and (c) ρ - λ] obtained from the Northern Harrat Rahat and the regression and rock types inferred by Ji et al. (2010) are correlated to infer possible rock types below Northern Harrat Rahat. It shows felsic upper crust (with felsic and intermediate gneiss, and diorite) and a mafic lower crust (with mafic gneiss, subordinate amphibolite, gabbro, and diabase rocks).

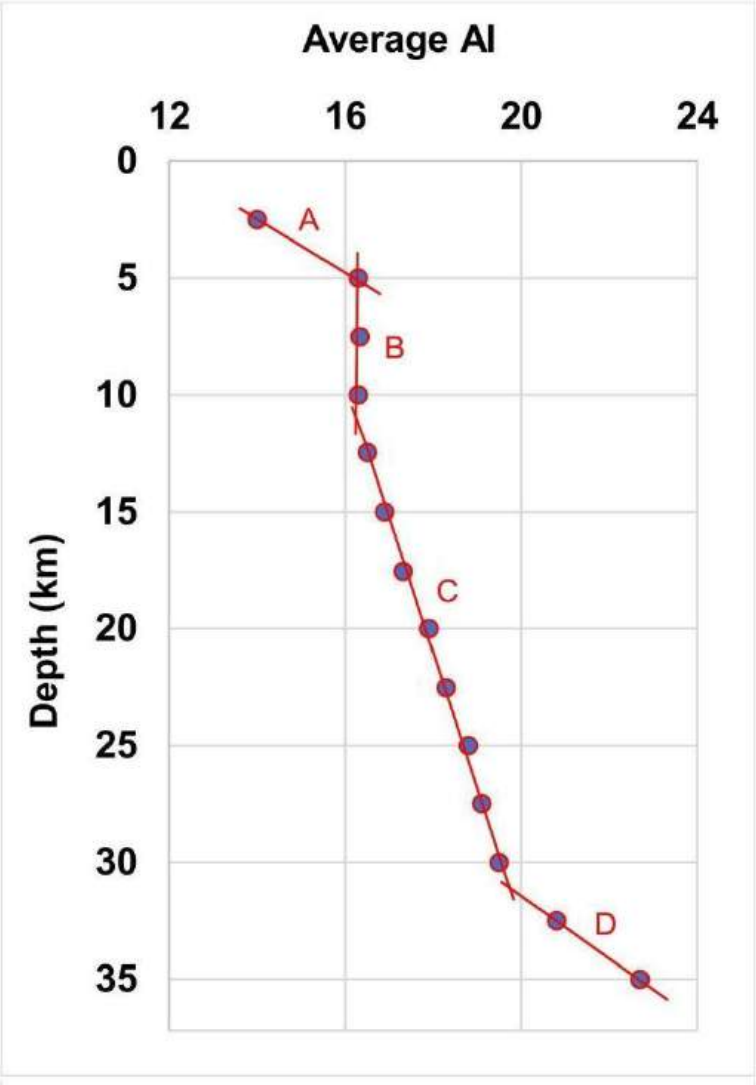

Figure 5: Depth wise plot of the average AI values in the NHR. From the change in slope of the curve, four zones (A to D) are identified. See text for explanation.

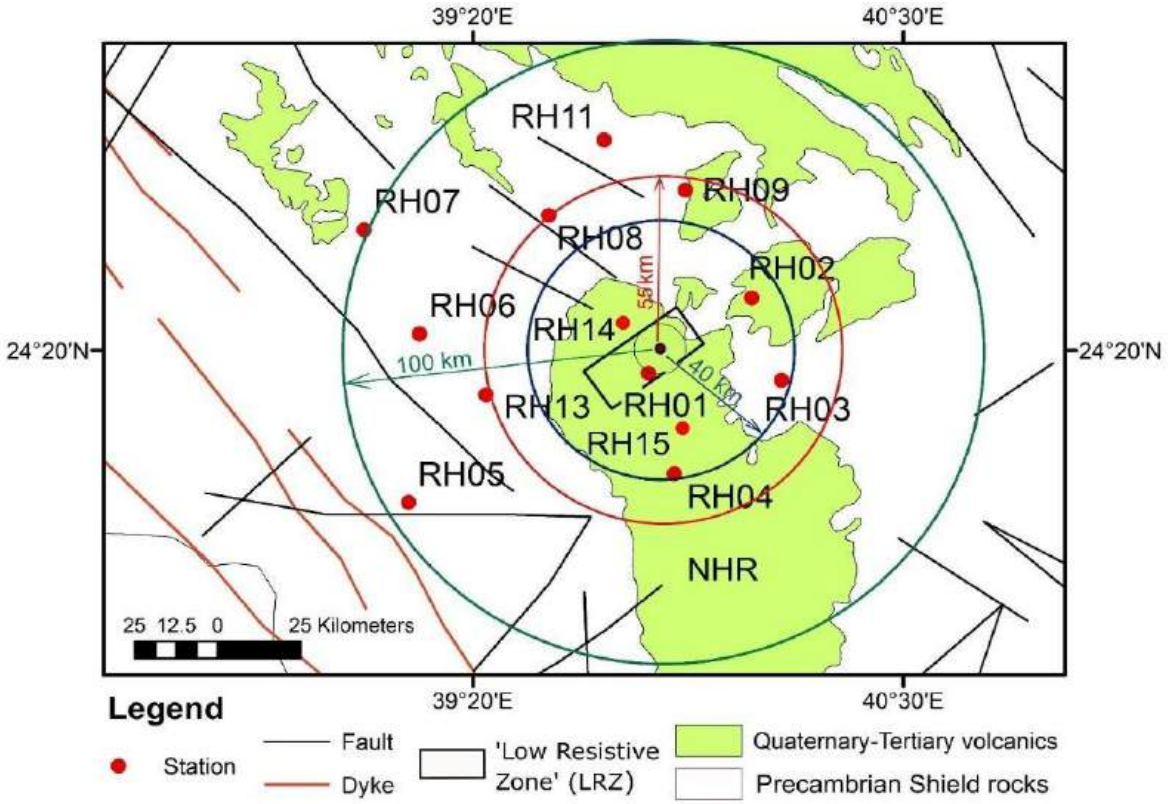

Figure 6: Four concentric circles are drawn circumventing the peak 'Low Resistive Zone' (LRZ) centered at 24°20'N, 39°50'E. Refer text for details. Seismic station RH01 is within a distance of 8 km from the peak LRZ.

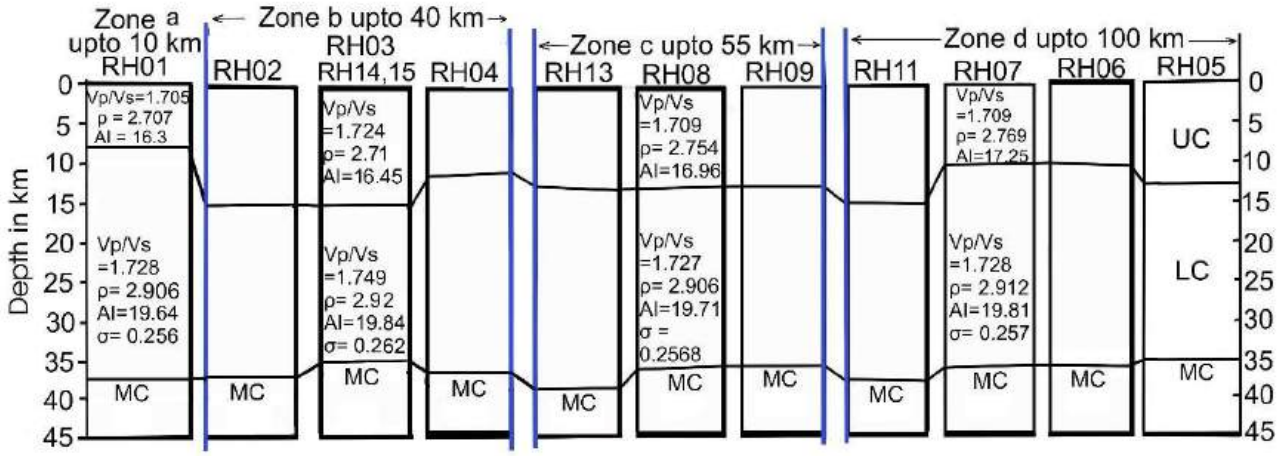

Figure 7: Location of REF seismic stations and the average distribution of rheological parameters within the upper and lower crustal columns within the radial zones a-d in figure 6 circumventing the LRZ discussed in the text. UC Upper crust, LC: Lower crust, MC: Moho.

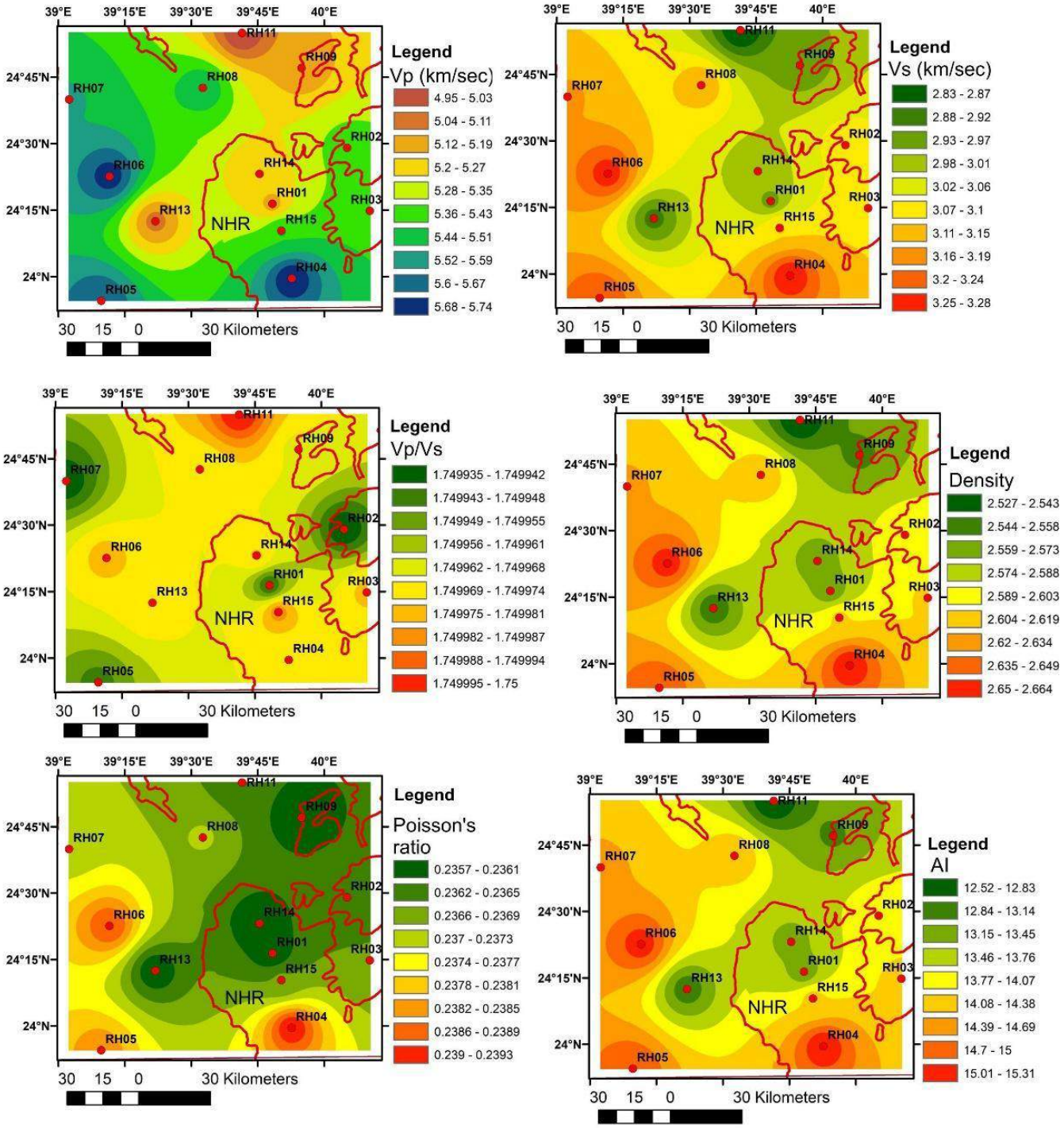

Figure 8: 2.5 km depth slices for selective crustal rheological parameters under the Northern Harrat Rahat (base data after Tang et al., 2019)

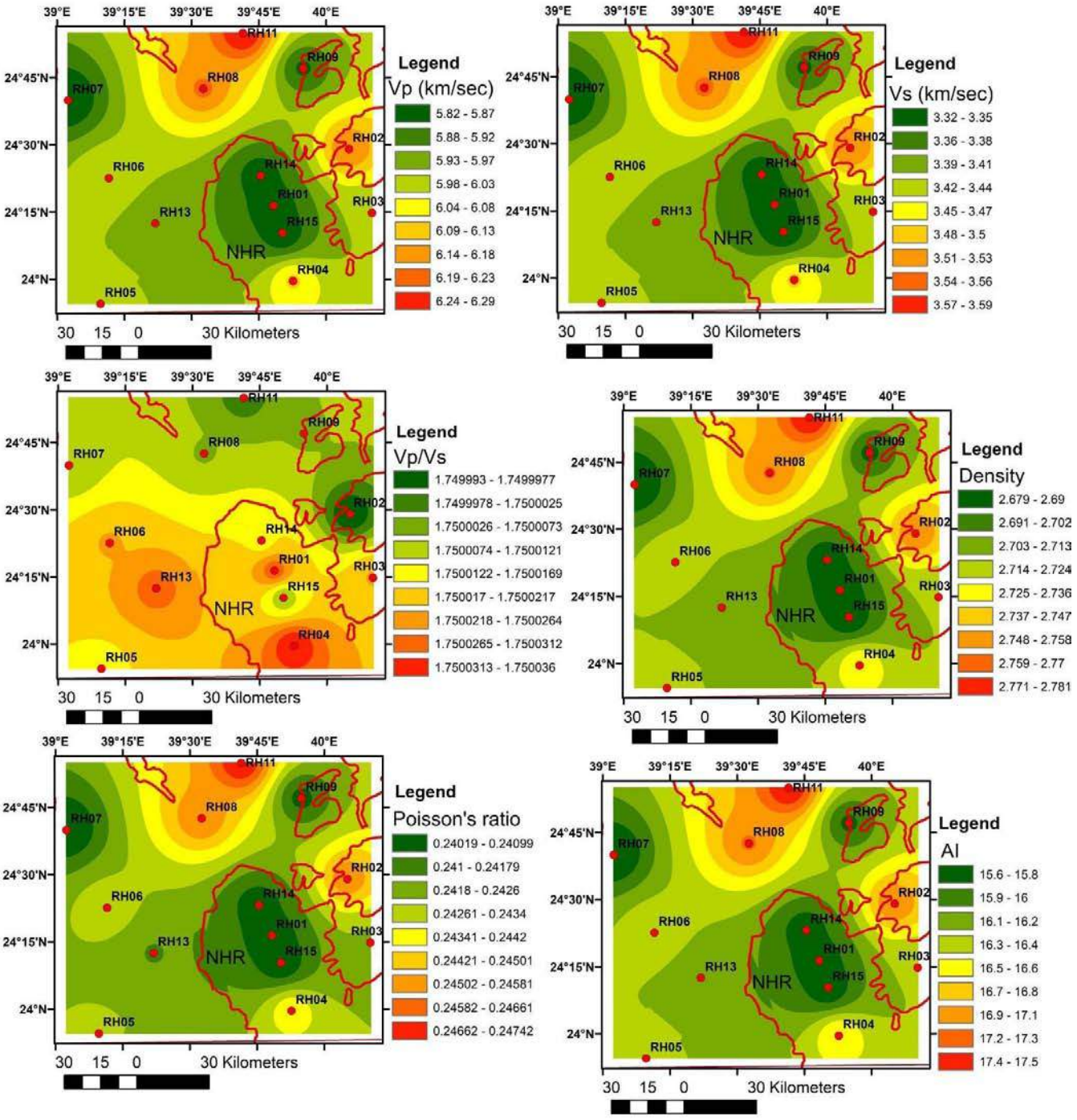

Figure 9: 5 km depth slices for selective crustal rheological parameters under the Northern Harrat Rahat (base data after Tang et al., 2019)

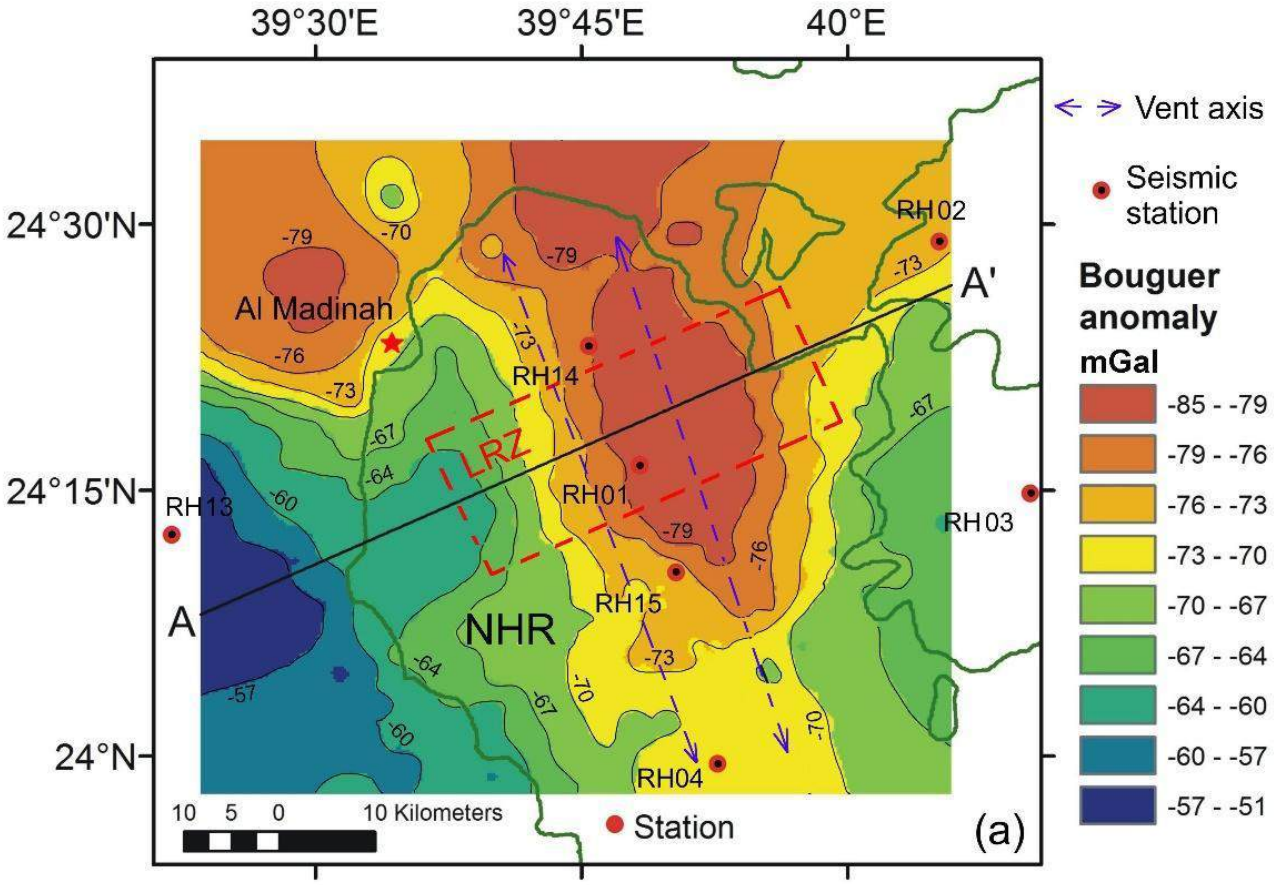

Figure 10: Bouguer anomaly map of Northern Harrat Rahat; redrawn after Langenheim (2018, 2019). The NNW-trending axial gravity low over NHR branches off westward to Al-Madinah. A-A' is a representative traverse illustrated on Figure 11. Red circles, REF seismic stations. Vent axes are also marked. Refer text for discussion.

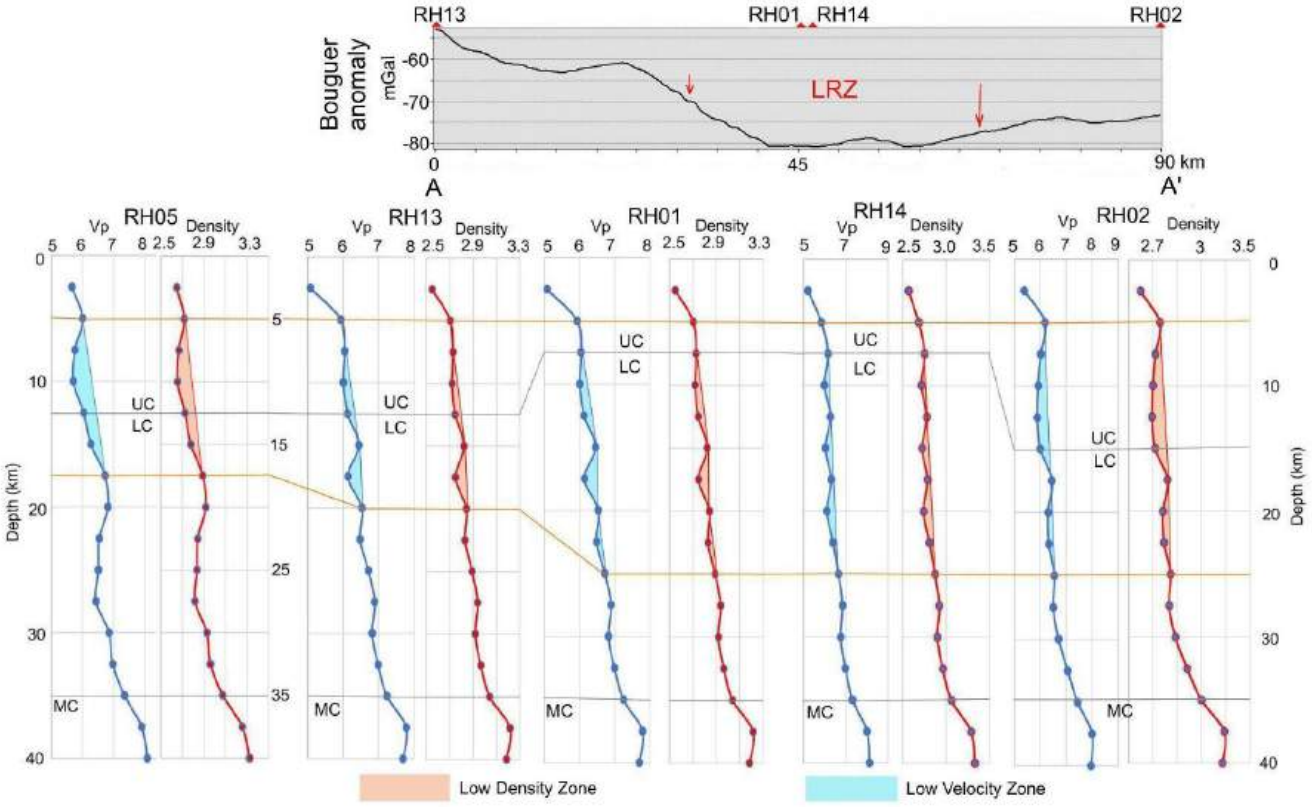

Figure 11: Plot for 2.5 km depth slices for Vp and Density underlying the five numbers of REF seismic stations, namely; RH05, RH13, RH01, RH14 and RH02 in bottom pannel. The gravity profile with gravity low zone (along the traverse A-A' of figure 10) and low resistivity zone (LRZ) are plotted in top pannel. The boundaries between upper crust (UC), lower crust (LC), and Moho (MC) are marked. Low velocity and low density zones are identified in depth section and marked.

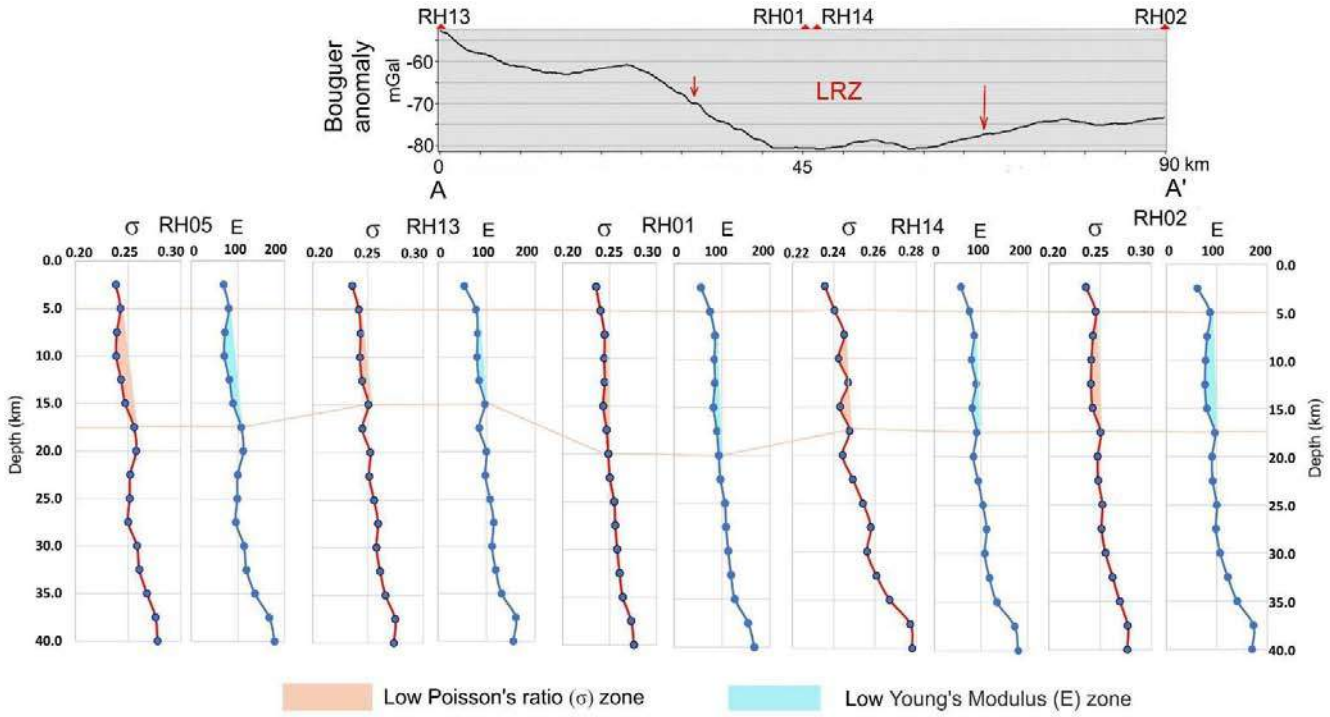

Figure 12: Plot for 2.5 km depth slices for and Poisson Ratio (σ) and Young's Modulus (E) underlying the five numbers of REF seismic stations, namely; RH05, RH13, RH01, RH14 and RH02 in bottom panel. The gravity profile with gravity low zone (along the traverse A-A' of figure 10) and low resistivity zone (LRZ) are plotted in the top panel. Low Poisson Ratio (σ) and low Young's Modulus (E) zones are identified in depth sections and marked.

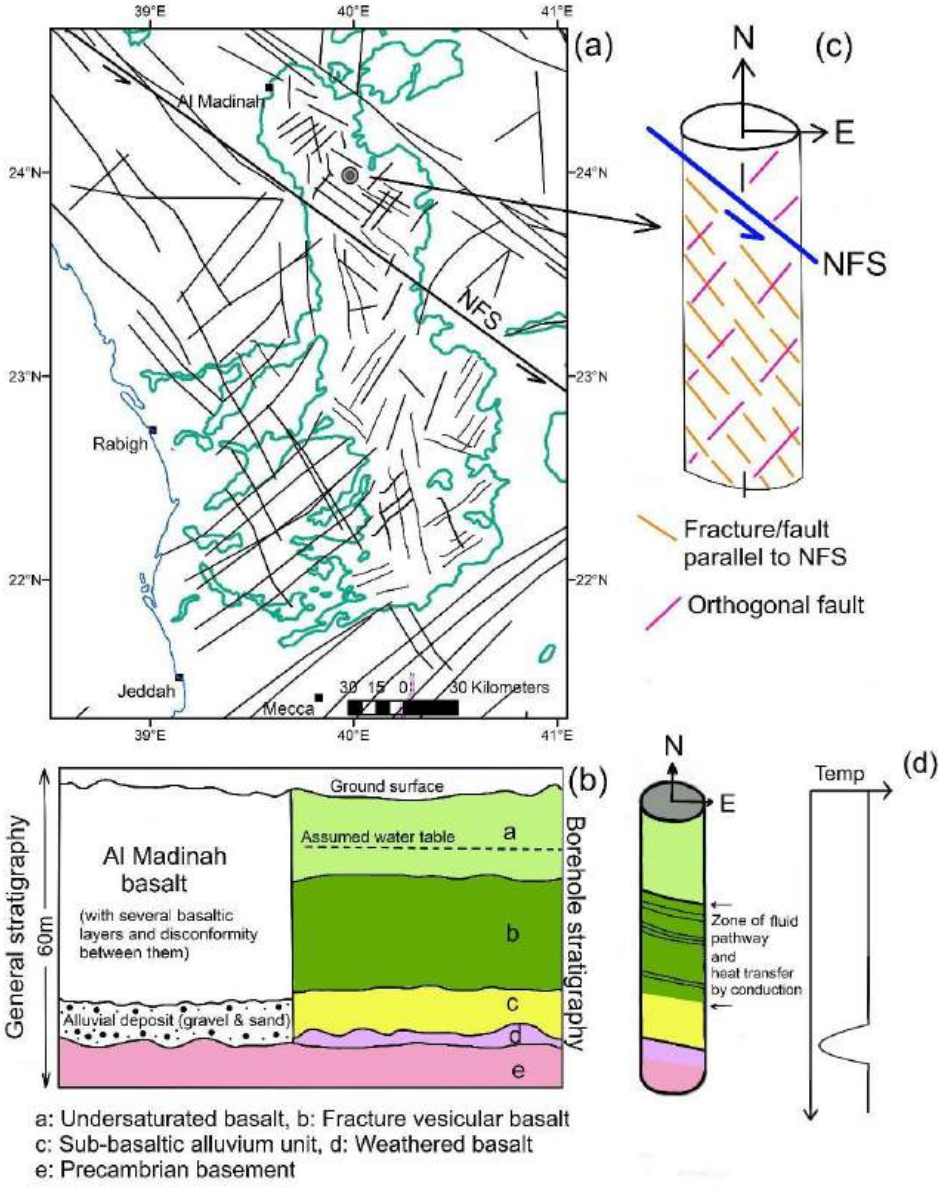

Figure 13: (a) Two dominant patterns of fractures and faulting across the Harrat Rahat and the Al-Madinah – Mecca region further north (adopted from: Coleman et al., 1983; Trippanera et al., 2019). One of them follows the left- lateral Najd Fault System (NFS) and its sympathetic parallel faults, while the other orthogonal normal faults are developed parallel to the Red Sea transforms. (b) Depicts the Borehole location, the general stratigraphy of the region from geological mapping and the borehole stratigraphy in NHR (after Al-Shaibani, 2003), (c) Conceptual model of fractures and faults in Madinah basalt in north part of NHR where the NFS is by far the most fault. The network of the fault system is supposedly amenable for fluid flow, and heat transfer to local streams or spring by conduction, (d) Schematic section of the major permeable fracture zone, including the fractured and vesicular basalt in the Medinah region, serve as fluid pathway, transmitting the heat by conduction and creating a probable temperature profile.

Table 1: The computed elastic constants up to 40 km depth for the 13 seismic broadband stations around Northern Harrat Rahat (REF data source: Tang et al., 2019). Abbreviations are: P-wave velocity, V_P; Shear-wave velocity, V_S; Density (g/cm³), ρ; Lame's Second constant (Shear Modulus), μ; Lame's First constant, λ; Bulk Modulus, K; Young's Modulus, E; and Poisson Ratio, σ; Acoustic impedance, AI; Thickness of upper crust, h_{UC}; thickness of lower crust, h_{LC}.

Seismic Stations	Latitude	Longitude	Depth (Km)	Vp (km/s)	Vs (km/s)	Depth (Km)	Vp/Vs	Density (g/cm³)	Lame's First constant, (λ)	Shear Modulus (μ)	Bulk Modulus (K)	Young's Modulus (E)	Poisson's Ratio (σ)	Acoustic impedance (AI)
RH01	24.273	39.805	2.5	5.1569	2.9469	2.5	1.74994	2.5595	23.6116	22.2270	38.4295	55.9032	0.2357	13.1989
	24.273	39.805	5	5.8325	3.3328	5	1.75003	2.6817	31.6523	29.7874	51.5103	74.9206	0.2404	15.6412
	24.273	39.805	7.5	6.1372	3.5069	7.5	1.75004	2.7468	35.8961	33.7806	58.4163	84.9644	0.2449	16.8574
	24.273	39.805	10	6.1101	3.4914	10	1.75004	2.7407	35.5020	33.4089	57.7743	84.0296	0.2444	16.7460
	24.273	39.805	12.5	6.1426	3.5101	12.5	1.74998	2.7480	35.9708	33.8573	58.5421	85.1556	0.2450	16.8797
	24.273	39.805	15	6.0524	3.4586	15	1.74996	2.7280	34.6666	32.6320	56.4210	82.0733	0.2435	16.5109
	24.273	39.805	17.5	6.2644	3.5796	17.5	1.75003	2.7759	37.7957	35.5691	61.5082	89.4626	0.2470	17.3894
	24.273	39.805	20	6.3623	3.6356	20	1.75000	2.7991	39.3104	36.9980	63.9754	93.0555	0.2488	17.8090
	24.273	39.805	22.5	6.4509	3.6863	22.5	1.74997	2.8208	40.7225	38.3313	66.2764	96.4080	0.2504	18.1967
	24.273	39.805	25	6.6912	3.8236	25	1.74997	2.8825	44.7716	42.1416	72.8657	105.9916	0.2551	19.2872
	24.273	39.805	27.5	6.747	3.8555	27.5	1.74997	2.8974	45.7567	43.0698	74.4696	108.3258	0.2562	19.5489
	24.273	39.805	30	6.8538	3.9164	30	1.75003	2.9267	47.6992	44.8896	77.6253	112.9051	0.2583	20.0587
	24.273	39.805	32.5	6.9845	3.9911	32.5	1.75002	2.9636	50.1600	47.2065	81.6307	118.7323	0.2609	20.6991
	24.273	39.805	35	7.1542	4.0881	35	1.75001	3.0134	53.5099	50.3613	87.0838	126.6665	0.2642	21.5583
	24.273	39.805	37.5	7.6872	4.3927	37.5	1.74999	3.1829	65.2534	61.4162	106.1971	154.4706	0.2733	24.4674
	24.273	39.805	40	7.9109	4.5206	40	1.74997	3.2596	70.7680	66.6124	115.1758	167.5385	0.2762	25.7863
RHo2	24.484	40.086	2.5	5.3884	3.0792	2.5	1.74994	2.5983	26.1694	24.6353	42.5928	61.9602	0.2363	14.0004
	24.484	40.086	5	6.1857	3.5347	5	1.74999	2.7577	36.6080	34.4554	59.5781	86.6604	0.2457	17.0585
	24.484	40.086	7.5	6.0225	3.4414	7.5	1.75001	2.7215	34.2475	32.2314	55.7348	81.0671	0.2430	16.3902
	24.484	40.086	10	5.9246	3.3854	10	1.75004	2.7007	32.8917	30.9524	53.5264	77.8511	0.2416	16.0005
	24.484	40.086	12.5	5.8932	3.3676	12.5	1.74997	2.6942	32.4601	30.5537	52.8291	76.8464	0.2412	15.8772
	24.484	40.086	15	6.009	3.4338	15	1.74996	2.7186	34.0534	32.0548	55.4230	80.6216	0.2428	16.3360
	24.484	40.086	17.5	6.4542	3.688	17.5	1.75005	2.8216	40.7837	38.3778	66.3686	96.5277	0.2505	18.2113
	24.484	40.086	20	6.2997	3.5998	20	1.75001	2.7842	38.3360	36.0793	62.3886	90.7452	0.2477	17.5396
	24.484	40.086	22.5	6.3328	3.6188	22.5	1.74997	2.7921	38.8459	36.5641	63.2217	91.9635	0.2483	17.6816
	24.484	40.086	25	6.5477	3.7416	25	1.74997	2.8451	42.3162	39.8306	68.8697	100.1790	0.2523	18.6290
	24.484	40.086	27.5	6.504	3.7166	27.5	1.74999	2.8341	41.5920	39.1472	67.6899	98.4606	0.2515	18.4327
	24.484	40.086	30	6.7058	3.8318	30	1.75004	2.8864	45.0341	42.3796	73.2869	106.5925	0.2554	19.3554
	24.484	40.086	32.5	7.054	4.0308	32.5	1.75002	2.9837	51.5116	48.4776	83.8297	121.9295	0.2623	21.0472
	24.484	40.086	35	7.4352	4.2486	35	1.75004	3.1003	59.4673	55.9627	96.7754	140.7564	0.2693	23.0515
	24.484	40.086	37.5	7.9956	4.569	37.5	1.74997	3.2894	72.9536	68.6697	118.7330	172.7128	0.2771	26.3011
	24.484	40.086	40	7.9525	4.5443	40	1.74999	3.2742	71.8390	67.6144	116.9148	170.0601	0.2766	26.0381
RHo3	24.247	40.172	2.5	5.4265	3.1009	2.5	1.74998	2.6049	26.6113	25.0479	43.3097	62.9988	0.2365	14.1357

	24.247	40.172	5	5.9842	3.4195	5	1.75002	2.7133	33.7116	31.7263	54.8623	79.7970	0.2425	16.2368
	24.247	40.172	7.5	5.9442	3.3966	7.5	1.75004	2.7048	33.1601	31.2050	53.9632	78.4864	0.2419	16.0779
	24.247	40.172	10	5.9824	3.4185	10	1.75001	2.7129	33.6855	31.7032	54.8208	79.7387	0.2424	16.2296
	24.247	40.172	12.5	5.8823	3.3613	12.5	1.75001	2.6919	32.3157	30.4141	52.5916	76.4961	0.2410	15.8346
	24.247	40.172	15	6.121	3.4978	15	1.74996	2.7431	35.6537	33.5612	58.0276	84.4103	0.2446	16.7907
	24.247	40.172	17.5	6.5729	3.7559	17.5	1.75002	2.8516	42.7435	40.2265	69.5610	101.1765	0.2528	18.7431
	24.247	40.172	20	6.2949	3.597	20	1.75004	2.7831	38.2643	36.0085	62.2697	90.5680	0.2476	17.5191
	24.247	40.172	22.5	6.4532	3.6876	22.5	1.74997	2.8214	40.7603	38.3661	66.3375	96.4957	0.2505	18.2069
	24.247	40.172	25	6.556	3.7463	25	1.74999	2.8472	42.4570	39.9604	69.0970	100.5063	0.2525	18.6665
	24.247	40.172	27.5	6.5314	3.7322	27.5	1.75001	2.8410	42.0481	39.5729	68.4298	99.5323	0.2520	18.5556
	24.247	40.172	30	6.7326	3.8472	30	1.75000	2.8935	45.5038	42.8271	74.0550	107.7167	0.2559	19.4810
	24.247	40.172	32.5	6.9832	3.9903	32.5	1.75004	2.9632	50.1377	47.1816	81.5918	118.6707	0.2609	20.6927
	24.247	40.172	35	7.2938	4.1679	35	1.74999	3.0559	56.4017	53.0850	91.7913	133.5165	0.2668	22.2890
	24.247	40.172	37.5	7.9123	4.5213	37.5	1.75001	3.2601	70.8096	66.6431	115.2378	167.6177	0.2762	25.7947
	24.247	40.172	40	8.0132	4.579	40	1.74999	3.2957	73.4180	69.1018	119.4854	173.8009	0.2772	26.4091
	23.993	39.878	2.5	5.7448	3.2828	2.5	1.74997	2.6642	30.5031	28.7117	49.6440	72.2135	0.2393	15.3054
	23.993	39.878	5	6.0861	3.4777	5	1.75004	2.7354	35.1547	33.0829	57.2098	83.2095	0.2440	16.6479
	23.993	39.878	7.5	6.0445	3.4539	7.5	1.75005	2.7263	34.5613	32.5229	56.2430	81.8013	0.2434	16.4789
	23.993	39.878	10	5.8782	3.3589	10	1.75004	2.6911	32.2626	30.3611	52.5032	76.3637	0.2410	15.8186
	23.993	39.878	12.5	6.0922	3.4813	12.5	1.74998	2.7367	35.2382	33.1678	57.3498	83.4213	0.2441	16.6728
	23.993	39.878	15	6.0217	3.441	15	1.74999	2.7213	34.2340	32.2218	55.7150	81.0424	0.2430	16.3870
	23.993	39.878	17.5	6.3578	3.6329	17.5	1.75006	2.7981	39.2448	36.9287	63.8637	92.8833	0.2487	17.7895
	23.993	39.878	20	6.3504	3.6287	20	1.75005	2.7963	39.1274	36.8200	63.6739	92.6093	0.2486	17.7575
	23.993	39.878	22.5	6.6119	3.7783	22.5	1.74997	2.8616	43.4001	40.8516	70.6342	102.7468	0.2535	18.9209
	23.993	39.878	25	6.6496	3.7998	25	1.74999	2.8715	44.0493	41.4600	71.6890	104.2777	0.2543	19.0943
	23.993	39.878	27.5	6.6728	3.8131	27.5	1.74997	2.8776	44.4497	41.8396	72.3425	105.2317	0.2547	19.2017
	23.993	39.878	30	6.8157	3.8946	30	1.75004	2.9161	47.0020	44.2316	76.4894	111.2505	0.2576	19.8755
	23.993	39.878	32.5	7.0465	4.0265	32.5	1.75003	2.9815	51.3651	48.3387	83.5906	121.5804	0.2621	21.0094
	23.993	39.878	35	7.1083	4.0618	35	1.75004	2.9997	52.5893	49.4898	85.5821	124.4758	0.2633	21.3228
	23.993	39.878	37.5	7.741	4.4235	37.5	1.74997	3.2010	66.5444	62.6358	108.3011	157.5371	0.2740	24.7792
RHo 4	23.993	39.878	40	7.8368	4.4782	40	1.74999	3.2338	68.9029	64.8522	112.1372	163.1124	0.2753	25.3429
	23.909	39.161	2.5	5.6567	3.2325	2.5	1.74995	2.6472	29.3838	27.6602	47.8237	69.5685	0.2383	14.9741
	23.909	39.161	5	6.0022	3.4298	5	1.75001	2.7171	33.9623	31.9630	55.2708	80.3922	0.2427	16.3087
	23.909	39.161	7.5	5.7559	3.289	7.5	1.75005	2.6664	30.6512	28.8439	49.8803	72.5478	0.2394	15.3476
	23.909	39.161	10	5.7016	3.258	10	1.75003	2.6558	29.9549	28.1900	48.7480	70.9028	0.2388	15.1422
	23.909	39.161	12.5	6.0386	3.4507	12.5	1.74996	2.7250	34.4712	32.4473	56.1025	81.6090	0.2433	16.4551
	23.909	39.161	15	6.2725	3.5843	15	1.74999	2.7778	37.9165	35.6870	61.7076	89.7579	0.2472	17.4238
RHo 5	23.909	39.161	17.5	6.7188	3.8392	17.5	1.75005	2.8898	45.2646	42.5946	73.6607	107.1338	0.2556	19.4162
	23.909	39.161	20	6.8201	3.8972	20	1.75000	2.9173	47.0783	44.3090	76.6174	111.4439	0.2576	19.8965
	23.909	39.161	22.5	6.5348	3.7342	22.5	1.74999	2.8418	42.1022	39.6274	68.5202	99.6684	0.2520	18.5709
	23.909	39.161	25	6.5084	3.7191	25	1.74999	2.8352	41.6652	39.2152	67.8084	98.6319	0.2515	18.4524
	23.909	39.161	27.5	6.432	3.6754	27.5	1.75001	2.8161	40.4213	38.0419	65.7824	95.6816	0.2501	18.1134
	23.909	39.161	30	6.8573	3.9184	30	1.75003	2.9276	47.7638	44.9504	77.7304	113.0580	0.2584	20.0756

	23.909	39.161	32.5	6.9719	3.9839	32.5	1.75002	2.9600	49.9183	46.9790	81.2373	118.1600	0.2606	20.6366
	23.909	39.161	35	7.3565	4.2037	35	1.75001	3.0754	57.7438	54.3460	93.9741	136.6888	0.2679	22.6243
	23.909	39.161	37.5	7.9047	4.517	37.5	1.74999	3.2574	70.6135	66.4621	114.9211	167.1618	0.2761	25.7490
	23.909	39.161	40	8.0896	4.6227	40	1.74997	3.3231	75.4436	71.0120	122.7845	178.6045	0.2779	26.8824
	24.377	39.192	2.5	5.71	3.2629	2.5	1.74998	2.6574	30.0582	28.2922	48.9195	71.1586	0.2389	15.1738
	24.377	39.192	5	6.0248	3.4427	5	1.75002	2.7220	34.2804	32.2616	55.7879	81.1434	0.2431	16.3995
	24.377	39.192	7.5	5.7619	3.2924	7.5	1.75006	2.6676	30.7298	28.9164	50.0072	72.7306	0.2395	15.3704
	24.377	39.192	10	6.0221	3.4412	10	1.75000	2.7214	34.2408	32.2266	55.7249	81.0548	0.2430	16.3886
	24.377	39.192	12.5	6.1375	3.5072	12.5	1.74997	2.7468	35.8956	33.7872	58.4202	84.9793	0.2449	16.8587
	24.377	39.192	15	6.0477	3.4559	15	1.74996	2.7270	34.6003	32.5689	56.3126	81.9146	0.2434	16.4919
	24.377	39.192	17.5	6.4011	3.6577	17.5	1.75003	2.8086	39.9280	37.5751	64.9778	94.5080	0.2495	17.9779
	24.377	39.192	20	6.3103	3.6058	20	1.75004	2.7867	38.5021	36.2323	62.6567	91.1309	0.2479	17.5850
	24.377	39.192	22.5	6.5582	3.7476	22.5	1.74997	2.8478	42.4921	39.9960	69.1558	100.5952	0.2525	18.6765
	24.377	39.192	25	6.7434	3.8535	25	1.74994	2.8964	45.6901	43.0107	74.3635	108.1763	0.2561	19.5319
	24.377	39.192	27.5	6.727	3.844	27.5	1.75000	2.8920	45.4046	42.7337	73.8934	107.4817	0.2558	19.4547
	24.377	39.192	30	6.5642	3.7509	30	1.75003	2.8493	42.5983	40.0881	69.3235	100.8288	0.2526	18.7037
	24.377	39.192	32.5	6.9042	3.9452	32.5	1.75003	2.9407	48.6363	45.7715	79.1504	115.1233	0.2593	20.3035
	24.377	39.192	35	7.5219	4.2982	35	1.75001	3.1282	61.4073	57.7929	99.9356	145.3585	0.2707	23.5304
	24.377	39.192	37.5	7.7097	4.4056	37.5	1.74998	3.1904	65.7897	61.9244	107.0723	155.7481	0.2736	24.5974
RHo 6	24.377	39.192	40	7.6089	4.348	40	1.74998	3.1568	63.4043	59.6792	103.1900	150.1010	0.2721	24.0196
	24.666	39.04	2.5	5.5158	3.152	2.5	1.74994	2.6209	27.6607	26.0391	45.0199	65.4908	0.2371	14.4564
	24.666	39.04	5	5.8186	3.3249	5	1.75001	2.6789	31.4670	29.6153	51.2104	74.4872	0.2402	15.5875
	24.666	39.04	7.5	5.9782	3.4161	7.5	1.75001	2.7120	33.6271	31.6483	54.7258	79.6005	0.2424	16.2129
	24.666	39.04	10	6.1985	3.542	10	1.75000	2.7607	36.7992	34.6346	59.8887	87.1112	0.2459	17.1119
	24.666	39.04	12.5	6.2933	3.5962	12.5	1.74999	2.7827	38.2351	35.9876	62.2266	90.5138	0.2475	17.5123
	24.666	39.04	15	6.1608	3.5205	15	1.74998	2.7521	36.2383	34.1091	58.9775	85.7888	0.2453	16.9550
	24.666	39.04	17.5	6.4936	3.7105	17.5	1.75006	2.8314	41.4275	38.9828	67.4158	98.0496	0.2513	18.3863
	24.666	39.04	20	6.4367	3.6781	20	1.75001	2.8173	40.4965	38.1135	65.9052	95.8614	0.2502	18.1341
	24.666	39.04	22.5	6.2562	3.575	22.5	1.74999	2.7740	37.6674	35.4533	61.3027	89.1701	0.2469	17.3546
	24.666	39.04	25	6.4651	3.6944	25	1.74997	2.8243	40.9537	38.5481	66.6521	96.9533	0.2507	18.2595
RHo 7	24.666	39.04	27.5	6.601	3.772	27.5	1.75000	2.8588	43.2175	40.6753	70.3340	102.3044	0.2533	18.8711
	24.666	39.04	30	6.5697	3.7541	30	1.75001	2.8508	42.6884	40.1764	69.4724	101.0500	0.2527	18.7286
	24.666	39.04	32.5	7.4126	4.2357	32.5	1.75003	3.0931	58.9685	55.4943	95.9643	139.5780	0.2689	22.9281
	24.666	39.04	35	7.6028	4.3444	35	1.75002	3.1548	63.2685	59.5423	102.9630	149.7591	0.2720	23.9850
	24.666	39.04	37.5	7.7012	4.4007	37.5	1.74999	3.1876	65.5882	61.7312	106.7420	155.2631	0.2735	24.5482
	24.666	39.04	40	7.7873	4.45	40	1.74996	3.2168	67.6723	63.7010	110.1391	160.2152	0.2747	25.0503
	24.71	39.543	2.5	5.4956	3.1404	2.5	1.74997	2.6173	27.4220	25.8117	44.6296	64.9196	0.2369	14.3834
	24.71	39.543	5	6.1924	3.5385	5	1.75001	2.7593	36.7088	34.5487	59.7410	86.8954	0.2458	17.0865
	24.71	39.543	7.5	6.0157	3.4375	7.5	1.75002	2.7200	34.1523	32.1410	55.5794	80.8401	0.2429	16.3629
	24.71	39.543	10	6.0196	3.4397	10	1.75004	2.7209	34.2082	32.1921	55.6694	80.9690	0.2430	16.3786
	24.71	39.543	12.5	6.1171	3.4955	12.5	1.74999	2.7423	35.5998	33.5064	57.9372	84.2736	0.2445	16.7747
RHo 8	24.71	39.543	15	6.1575	3.5187	15	1.74994	2.7513	36.1864	34.0649	58.8961	85.6767	0.2452	16.9413
	24.71	39.543	17.5	6.0993	3.4853	17.5	1.75001	2.7383	35.3429	33.2631	57.5181	83.6620	0.2442	16.7018

	24.71	39.543	20	6.3125	3.6071	20	1.75002	2.7872	38.5344	36.2652	62.7110	91.2131	0.2479	17.5944
	24.71	39.543	22.5	6.1418	3.5096	22.5	1.75000	2.7478	35.9607	33.8454	58.5241	85.1263	0.2449	16.8764
	24.71	39.543	25	6.5971	3.7698	25	1.74999	2.8578	43.1499	40.6135	70.2253	102.1486	0.2532	18.8533
	24.71	39.543	27.5	6.7617	3.8638	27.5	1.75001	2.9014	46.0239	43.3147	74.9001	108.9436	0.2565	19.6183
	24.71	39.543	30	6.7296	3.8454	30	1.75004	2.8927	45.4544	42.7752	73.9709	107.5874	0.2559	19.4669
	24.71	39.543	32.5	7.0242	4.0138	32.5	1.75001	2.9750	50.9274	47.9297	82.8802	120.5510	0.2617	20.8973
	24.71	39.543	35	7.5902	4.3372	35	1.75002	3.1506	62.9759	59.2669	102.4868	149.0664	0.2718	23.9137
	24.71	39.543	37.5	7.9278	4.5302	37.5	1.74999	3.2655	71.2032	67.0172	115.8809	168.5578	0.2763	25.8883
	24.71	39.543	40	7.8241	4.471	40	1.74997	3.2295	68.5834	64.5562	111.6204	162.3669	0.2751	25.2675
	24.785	39.915	2.5	5.1239	2.928	2.5	1.74997	2.5542	23.2634	21.8974	37.8615	55.0747	0.2357	13.0873
	24.785	39.915	5	5.862	3.3497	5	1.75001	2.6877	32.0433	30.1577	52.1483	75.8514	0.2407	15.7555
	24.785	39.915	7.5	6.1775	3.5299	7.5	1.75005	2.7559	36.4908	34.3386	59.3829	86.3683	0.2455	17.0244
	24.785	39.915	10	5.9486	3.3991	10	1.75005	2.7057	33.2211	31.2616	54.0620	78.6291	0.2419	16.0953
	24.785	39.915	12.5	6.1439	3.5109	12.5	1.74995	2.7483	35.9877	33.8763	58.5716	85.2026	0.2450	16.8851
	24.785	39.915	15	6.1517	3.5153	15	1.74998	2.7500	36.1044	33.9830	58.7595	85.4717	0.2451	16.9173
	24.785	39.915	17.5	6.3049	3.6027	17.5	1.75005	2.7854	38.4191	36.1534	62.5211	90.9327	0.2478	17.5619
	24.785	39.915	20	6.3265	3.6151	20	1.75002	2.7906	38.7518	36.4698	63.0647	91.7276	0.2481	17.6545
	24.785	39.915	22.5	6.2237	3.5564	22.5	1.75000	2.7664	37.1769	34.9900	60.5033	88.0052	0.2463	17.2176
	24.785	39.915	25	6.4664	3.6951	25	1.74999	2.8246	40.9766	38.5671	66.6877	97.0018	0.2507	18.2653
	24.785	39.915	27.5	6.4537	3.6878	27.5	1.75001	2.8215	40.7720	38.3719	66.3531	96.5117	0.2505	18.2091
RH09	24.785	39.915	30	6.6577	3.8043	30	1.75005	2.8736	44.1951	41.5890	71.9208	104.6043	0.2544	19.1317
	24.785	39.915	32.5	6.8318	3.9038	32.5	1.75004	2.9206	47.2961	44.5084	76.9681	111.9467	0.2579	19.9527
	24.785	39.915	35	7.799	4.4565	35	1.75003	3.2208	67.9710	63.9668	110.6151	160.8877	0.2748	25.1192
	24.785	39.915	37.5	8.2863	4.735	37.5	1.75001	3.3951	80.8793	76.1190	131.6248	191.4516	0.2792	28.1329
	24.785	39.915	40	8.2022	4.687	40	1.74999	3.3640	78.5173	73.9012	127.7842	185.8720	0.2787	27.5926
	24.916	39.691	2.5	4.9518	2.8296	2.5	1.75000	2.5274	21.5005	20.2358	34.9910	50.8961	0.2362	12.5151
	24.916	39.691	5	6.286	3.592	5	1.75000	2.7810	38.1240	35.8814	62.0447	90.2471	0.2474	17.4812
	24.916	39.691	7.5	6.403	3.6588	7.5	1.75003	2.8090	39.9577	37.6039	65.0267	94.5803	0.2495	17.9862
	24.916	39.691	10	6.1567	3.5181	10	1.75001	2.7512	36.1801	34.0511	58.8806	85.6439	0.2452	16.9380
	24.916	39.691	12.5	5.9664	3.4094	12.5	1.74999	2.7095	33.4620	31.4951	54.4585	79.2147	0.2422	16.1659
	24.916	39.691	15	6.1366	3.5067	15	1.74996	2.7466	35.8819	33.7751	58.3984	84.9486	0.2449	16.8550
	24.916	39.691	17.5	6.3401	3.6229	17.5	1.75001	2.7938	38.9627	36.6700	63.4091	92.2307	0.2484	17.7131
	24.916	39.691	20	6.2831	3.5903	20	1.75002	2.7803	38.0812	35.8386	61.9733	90.1402	0.2474	17.4688
	24.916	39.691	22.5	6.3088	3.6051	22.5	1.74997	2.7864	38.4725	36.2136	62.6147	91.0816	0.2478	17.5786
	24.916	39.691	25	6.5349	3.7343	25	1.74997	2.8419	42.1021	39.6299	68.5217	99.6740	0.2520	18.5713
	24.916	39.691	27.5	6.6338	3.7908	27.5	1.74997	2.8674	43.7758	41.2043	71.2451	103.6343	0.2540	19.0214
RH11	24.916	39.691	30	6.77	3.8685	30	1.75003	2.9036	46.1746	43.4539	75.1436	109.2942	0.2567	19.6577
	24.916	39.691	32.5	6.9679	3.9816	32.5	1.75003	2.9588	49.8424	46.9066	81.1131	117.9782	0.2606	20.6168
RH13	24.916	39.691	35	7.4854	4.2774	35	1.74999	3.1164	60.5800	57.0187	98.5921	143.4102	0.2701	23.3277
	24.916	39.691	37.5	7.8932	4.5104	37.5	1.75000	3.2534	70.3230	66.1864	114.4468	166.4688	0.2760	25.6798
	24.916	39.691	40	7.9565	4.5466	40	1.74999	3.2756	71.9414	67.7120	117.0823	170.3053	0.2767	26.0624
	24.916	39.691	42.5	8.0438	4.453	42.5	1.80638	3.3066	82.8121	65.5678	126.5236	167.7295	0.2775	26.5978
	24.208	39.365	2.5	5.0814	2.9037	2.5	1.74997	2.5474	22.8191	21.4786	37.1380	54.0215	0.2358	12.9445

	24.208	39.365	5	5.9347	3.3912	5	1.75003	2.7028	33.0288	31.0829	53.7505	78.1789	0.2417	16.0403
	24.208	39.365	7.5	6.047	3.4554	7.5	1.75001	2.7268	34.5941	32.5576	56.2990	81.8877	0.2434	16.4891
	24.208	39.365	10	6.0094	3.4339	10	1.75002	2.7187	34.0638	32.0577	55.4354	80.6306	0.2428	16.3376
	24.208	39.365	12.5	6.1314	3.5037	12.5	1.74998	2.7455	35.8070	33.7031	58.2755	84.7677	0.2448	16.8335
	24.208	39.365	15	6.4481	3.6847	15	1.74997	2.8201	40.6771	38.2886	66.2026	96.3006	0.2504	18.1843
	24.208	39.365	17.5	6.1434	3.5104	17.5	1.75006	2.7482	35.9886	33.8653	58.5652	85.1779	0.2450	16.8830
	24.208	39.365	20	6.532	3.7325	20	1.75003	2.8411	42.0599	39.5814	68.4472	99.5543	0.2520	18.5583
	24.208	39.365	22.5	6.4826	3.7044	22.5	1.74997	2.8287	41.2393	38.8169	67.1170	97.6296	0.2510	18.3373
	24.208	39.365	25	6.7162	3.8379	25	1.74997	2.8891	45.2104	42.5556	73.5805	107.0325	0.2556	19.4041
	24.208	39.365	27.5	6.893	3.9389	27.5	1.74998	2.9376	48.4221	45.5766	78.8063	114.6314	0.2591	20.2489
	24.208	39.365	30	6.8198	3.8969	30	1.75006	2.9173	47.0787	44.3009	76.6124	111.4257	0.2576	19.8951
	24.208	39.365	32.5	6.9897	3.994	32.5	1.75005	2.9651	50.2635	47.2990	81.7958	118.9661	0.2610	20.7250
	24.208	39.365	35	7.2442	4.1395	35	1.75002	3.0406	55.3622	52.1025	90.0969	131.0464	0.2659	22.0269
	24.208	39.365	37.5	7.7864	4.4494	37.5	1.74999	3.2165	67.6550	63.6777	110.1064	160.1585	0.2746	25.0450
	24.208	39.365	40	7.6961	4.3978	40	1.74999	3.1859	65.4653	61.6167	106.5427	154.9748	0.2734	24.5187
	24.386	39.757	2.5	5.1934	2.9677	2.5	1.74997	2.5654	24.0042	22.5941	39.0668	56.8270	0.2357	13.3231
	24.386	39.757	5	5.8363	3.335	5	1.75001	2.6825	31.7016	29.8353	51.5916	75.0407	0.2404	15.6559
	24.386	39.757	7.5	6.151	3.5148	7.5	1.75003	2.7499	36.0979	33.9714	58.7453	85.4439	0.2451	16.9144
	24.386	39.757	10	5.9825	3.4185	10	1.75004	2.7129	33.6890	31.7035	54.8245	79.7400	0.2424	16.2300
	24.386	39.757	12.5	6.2615	3.578	12.5	1.75000	2.7752	37.7492	35.5287	61.4348	89.3600	0.2470	17.3771
	24.386	39.757	15	6.0292	3.4453	15	1.74998	2.7229	34.3393	32.3217	55.8869	81.2933	0.2431	16.4172
	24.386	39.757	17.5	6.3021	3.6011	17.5	1.75005	2.7848	38.3759	36.1127	62.4508	90.8303	0.2477	17.5499
	24.386	39.757	20	6.1057	3.4889	20	1.75004	2.7397	35.4377	33.3491	57.6702	83.8791	0.2443	16.7280
	24.386	39.757	22.5	6.388	3.6503	22.5	1.74999	2.8054	39.7161	37.3807	64.6363	94.0178	0.2493	17.9207
	24.386	39.757	25	6.6444	3.7969	25	1.74995	2.8701	43.9564	41.3771	71.5409	104.0680	0.2542	19.0703
	24.386	39.757	27.5	6.8381	3.9075	27.5	1.74999	2.9223	47.4071	44.6194	77.1530	112.2242	0.2580	19.9830
	24.386	39.757	30	6.7474	3.8556	30	1.75003	2.8975	45.7696	43.0736	74.4851	108.3376	0.2562	19.5508
	24.386	39.757	32.5	6.9764	3.9865	32.5	1.75001	2.9613	50.0031	47.0608	81.3767	118.3653	0.2607	20.6589
	24.386	39.757	35	7.3112	4.1778	35	1.75001	3.0613	56.7733	53.4316	92.3940	134.3891	0.2671	22.3816
RH14	24.386	39.757	37.5	7.9916	4.5666	37.5	1.75001	3.2880	72.8561	68.5679	118.5676	172.4594	0.2770	26.2766
	24.386	39.757	40	8.1105	4.6346	40	1.74999	3.3306	76.0088	71.5403	123.7019	179.9340	0.2781	27.0130
	24.173	39.839	2.5	5.433	3.1046	2.5	1.74998	2.6061	26.6873	25.1188	43.4330	63.1772	0.2365	14.1588
	24.173	39.839	5	5.8207	3.3261	5	1.75001	2.6793	31.4947	29.6414	51.2555	74.5527	0.2402	15.5956
	24.173	39.839	7.5	6.0836	3.4763	7.5	1.75002	2.7348	35.1177	33.0496	57.1505	83.1253	0.2440	16.6377
	24.173	39.839	10	5.9549	3.4028	10	1.75000	2.7071	33.3042	31.3451	54.2007	78.8377	0.2420	16.1202
RH15	24.173	39.839	12.5	6.0276	3.4444	12.5	1.74997	2.7226	34.3162	32.3007	55.8497	81.2403	0.2431	16.4108
	24.173	39.839	15	6.2275	3.5586	15	1.74999	2.7673	37.2330	35.0444	60.5957	88.1416	0.2464	17.2335
	24.173	39.839	17.5	6.3396	3.6226	17.5	1.75001	2.7937	38.9555	36.6623	63.3968	92.2117	0.2484	17.7109
	24.173	39.839	20	6.4545	3.6882	20	1.75004	2.8217	40.7874	38.3830	66.3758	96.5403	0.2505	18.2126
	24.173	39.839	22.5	6.5123	3.7214	22.5	1.74996	2.8361	41.7266	39.2773	67.9112	98.7871	0.2516	18.4699
	24.173	39.839	25	6.4968	3.7125	25	1.74998	2.8322	41.4729	39.0359	67.4966	98.1806	0.2513	18.4005
	24.173	39.839	27.5	6.6146	3.7798	27.5	1.74999	2.8623	43.4480	40.8941	70.7105	102.8543	0.2536	18.9333
	24.173	39.839	30	6.8023	3.887	30	1.75001	2.9125	46.7558	44.0035	76.0912	110.6761	0.2573	19.8114

	24.173	39.839	32.5	6.9219	3.9554	32.5	1.74999	2.9457	48.9650	46.0866	79.6891	115.9144	0.2597	20.3901
	24.173	39.839	35	7.0574	4.0328	35	1.75000	2.9847	51.5757	48.5419	83.9367	122.0902	0.2623	21.0643
	24.173	39.839	37.5	7.7692	4.4396	37.5	1.74998	3.2106	67.2318	63.2817	109.4192	159.1618	0.2744	24.9440
	24.173	39.839	40	8.0257	4.5862	40	1.74997	3.3002	73.7434	69.4130	120.0182	174.5823	0.2773	26.4861

Table 2: The average elastic constants for upper and lower crust in the 13 seismic broadband stations around Northern Harrat Rahat (REF data source: Tang et al., 2019). Abbreviations are: P-wave velocity, V_P; Shear-wave velocity, V_S; Density (g/cm^3), ρ; Lame's Second constant (Shear Modulus), μ; Lame's First constant, λ; Bulk Modulus, K; Young's Modulus, E; and Poisson Ratio, σ; Acoustic impedance, AI; Thickness of upper crust, h_{UC}; thickness of lower crust, h_{LC}.

Station	Latitude	Longitude	Moho(km)	huc	Vp	Vs	Vp/Vs	ρ	λ	μ	K	Bulk Compression (1/K)	E	σ	AI
Upper crust															
RH01	24.27	39.81	34.40	7.50	6.020	3.530	1.705	2.707	30.639	33.732	53.127	0.019	83.519	0.238	16.296
RH02	24.48	40.09	34.80	15.00	6.290	3.680	1.709	2.789	34.805	37.770	59.985	0.017	93.653	0.240	17.543
RH03	24.25	40.17	35.80	15.00	6.240	3.650	1.710	2.771	34.063	36.917	58.674	0.017	91.549	0.240	17.291
RH04	23.99	39.88	35.40	10.00	6.020	3.680	1.636	2.707	24.784	36.659	49.224	0.020	88.106	0.202	16.296
RH05	23.91	39.16	27.20	12.50	6.270	3.660	1.713	2.778	34.785	37.213	59.594	0.017	92.405	0.242	17.418
RH06	24.38	39.19	34.00	10.00	6.290	3.620	1.738	2.760	36.861	36.168	60.973	0.016	90.592	0.252	17.360
RH07	24.67	39.04	32.40	10.00	6.220	3.640	1.709	2.766	33.715	36.648	58.148	0.017	90.857	0.240	17.205
RH08	24.71	39.54	34.80	12.50	6.290	3.670	1.714	2.783	35.139	37.484	60.128	0.017	93.105	0.242	17.505
RH09	24.78	39.91	35.00	12.50	6.130	3.570	1.717	2.748	33.215	35.023	56.564	0.018	87.094	0.243	16.845
RH10	24.58	39.90	34.60	10.00	6.220	3.640	1.709	2.766	33.715	36.648	58.148	0.017	90.857	0.240	17.205
RH11	24.92	39.69	35.40	15.00	6.240	3.650	1.710	2.771	34.063	36.917	58.674	0.017	91.549	0.240	17.291
RH13	24.21	39.37	36.10	12.50	6.060	3.560	1.702	2.731	31.069	34.612	54.143	0.018	85.596	0.237	16.550
RH14	24.39	39.76	35.80	12.50	5.884	3.362	1.750	2.653	31.877	29.987	51.868	0.019	75.425	0.258	15.610
RH15	24.17	39.84	35.70	12.50	5.863	3.350	1.750	2.646	31.566	29.695	51.363	0.019	74.690	0.258	15.513
Lower crust															
Station	Latitude	Longitude	Moho (km)	h_{LC}	Vp	Vs	Vp/Vs	ρ	λ	μ	K	Bulk Compression (1/K)	E	σ	AI
RH01	24.27	39.81	34.40	26.90	7.273	3.910	1.860	3.049	68.045	46.619	99.124	0.010	120.902	0.297	22.177
RH02	24.48	40.09	34.80	19.80	6.974	3.940	1.770	2.961	52.066	45.958	82.704	0.012	116.326	0.266	20.646
RH03	24.25	40.17	35.80	20.80	6.747	3.900	1.730	2.897	43.757	44.070	73.137	0.014	110.096	0.249	19.549
RH04	23.99	39.88	35.40	25.40	6.938	3.920	1.770	2.950	51.363	45.337	81.587	0.012	114.756	0.266	20.471
RH05	23.91	39.16	27.20	14.70	6.940	4.010	1.731	2.951	47.224	47.450	78.857	0.013	118.569	0.249	20.479
RH06	24.38	39.19	34.00	24.00	6.810	3.940	1.728	2.915	44.677	45.244	74.840	0.013	112.968	0.248	19.848
RH07	24.67	39.04	32.40	22.40	6.669	3.900	1.710	2.877	40.432	43.753	69.601	0.014	108.520	0.240	19.184
RH08	24.71	39.54	34.80	22.30	6.829	3.880	1.760	2.920	48.245	43.955	77.548	0.013	110.910	0.262	19.938
RH09	24.78	39.91	35.00	22.50	6.755	3.860	1.750	2.900	45.903	43.203	74.704	0.013	108.661	0.258	19.587
RH10	24.58	39.90	34.60	24.60	6.906	3.880	1.780	2.941	51.737	44.280	81.258	0.012	112.421	0.269	20.314
RH11	24.92	39.69	35.40	20.40	6.730	3.890	1.730	2.893	43.463	43.774	72.645	0.014	109.356	0.249	19.467
RH13	24.21	39.37	36.10	23.60	7.000	4.030	1.737	2.968	49.027	48.204	81.163	0.012	120.713	0.252	20.776
RH14	24.39	39.76	35.80	23.30	6.771	3.847	1.760	2.904	47.169	42.975	75.820	0.013	108.438	0.262	19.661
RH15	24.17	39.84	35.70	23.20	6.910	3.839	1.800	2.942	53.773	43.365	82.683	0.012	110.737	0.277	20.333

Table 3: Hydraulic parameters were estimated from the pumping test data from the boreholes drilled to shallow depths in the Madinah Basaltic Terrain, Northern Harrat Rahat. Source: Al-Shaibani (2003).

Well no	Transmissivity (m^2/s)	Specific Yield	Remarks
ME-T1	$3x10^{-3}$	$8.7x10^{-2}$	Italconsult (1979)
ME-T2	$3.2x10^{-3}$	$2.6x10^{-4}$	Italconsult (1979)
ME-T5	$2.5x10^{-2}$	-	Italconsult (1979)
WSA-301	$2.1x10^{-3}$	-	By driller, reported in Al-Shaibani (2003)
WSA-302	$5.5x10^{-5}$	-	Permeability is locally very low
WSA-303	$9.8x10^{-3}$	-	-
WSA-306	0.15	-	Productive well, highly fractured zone?
WSA-328	$7.0x10^{-2}$	$8.5x10^{-2}$	Al-Shaibani (2003)
BR-14	$1.8x10^{-4}$	$4x10^{-2}$	Reported in Al-Shaibani (2003)

Fostering Social Inclusion in Indian Museums: A Reflective Analysis of Outreach Initiatives for Enhancing Museum Accessibility and Inclusivity

Dr. Sadiya Juhi

ABSTRACT

Museums play a crucial role in non-formal education and sensory engagement enhancing cultural and heritage experiences. They represent a society's cultural legacy, serving as ambassadors that inspire the preservation and promotion of cultural identities. Everyone in society has an equal right to access museums. In recent years, the scope of museum education has widened beyond universal accessibility to offer equitable learning opportunities for everyone, regardless of social, economic, cultural, or educational background. This shift is reflected in ICOM's latest definition of museums, emphasising their role in providing inclusive learning opportunities. Efforts are underway to transform museums into dynamic, accessible, and inclusive spaces that cater to diverse groups, including those historically excluded or marginalized, thereby meeting the varied learning needs of all individuals.

These institutions become particularly relevant in a country like India, where many people lack physical access to museums. The concepts of accessibility, inclusivity, diversity, and sustainability, integral to the new definition of museums, must also shape museum approaches and practices, particularly in India, with its rich heritage and diverse population.

Keywords: NA

Classification: LCC Code: AM7

Language: English

Great Britain Journals Press

LJP Copyright ID: 925615
Print ISSN: 2631-8490
Online ISSN: 2631-8504

London Journal of Research in Science: Natural & Formal

Volume 25 | Issue 2 | Compilation 1.0

Fostering Social Inclusion in Indian Museums: A Reflective Analysis of Outreach Initiatives for Enhancing Museum Accessibility and Inclusivity

Dr. Sadiya Juhi

ABSTRACT

Museums play a crucial role in non-formal education and sensory engagement enhancing cultural and heritage experiences. They represent a society's cultural legacy, serving as ambassadors that inspire the preservation and promotion of cultural identities. Everyone in society has an equal right to access museums. In recent years, the scope of museum education has widened beyond universal accessibility to offer equitable learning opportunities for everyone, regardless of social, economic, cultural, or educational background. This shift is reflected in ICOM's latest definition of museums, emphasising their role in providing inclusive learning opportunities. Efforts are underway to transform museums into dynamic, accessible, and inclusive spaces that cater to diverse groups, including those historically excluded or marginalized, thereby meeting the varied learning needs of all individuals.

These institutions become particularly relevant in a country like India, where many people lack physical access to museums. The concepts of accessibility, inclusivity, diversity, and sustainability, integral to the new definition of museums, must also shape museum approaches and practices, particularly in India, with its rich heritage and diverse population.

The paper outlines the current situational, operational, and engagement structures of museums in India, emphasising the challenges they face and their public perception. It discusses outreach initiatives designed to extend the 'Right to Museums' to everyone through pilot outreach educational programs, specifically targeting those who do not or cannot visit museums. The study delves into the approach, methodology, execution, audience response, and impact of the action research project 'Museum Outreach Initiatives and the Creation of Museum Educational Resources,' conducted by the author. As part of the project, a series of workshops were conceptualised and conducted around a unified theme for diverse Indian audiences across various regions. These workshops, developed as part of the action research project, champion the belief that everyone has the right to cultural life. The paper reflects on the endeavors made by the author to understand the varied needs of diverse Indian audiences and create tailored educational resources and workshop models. It seeks to share these case studies with the broader museum community, aiming to broaden the spectrum of museum inclusivity through outreach initiatives.

I. INTRODUCTION

Museums are one of the largest mediums of non-formal education and cultural enrichment for the culture and heritage sector. They are powerful representations of a society's cultural legacy and life, serving as cultural ambassadors that inspire people to preserve and promote their cultural identity. Everyone in society has an equal right to access museums. Historically, museums were exclusive spaces

London Journal of Research in Science: Natural & Formal

for the privileged, but since becoming public institutions, they have become vital centers for non-formal learning.

In recent years, the scope of museum education has widened from merely providing learning opportunities to ensuring equitable access for all, regardless of social, economic, cultural, or educational background. The ICOM definition of museums[1], adopted in 2022, highlights how museums are adapting their methodologies to be more diverse, accessible, inclusive, and participatory. From the ICOM latest definition of museum, it is clear that museum professionals value the core functions of museums while recognizing significant transformations due to evolving values within both museums and society (Bonilla-Merchav and Brulon Soares 2022). Bonilla-Merchav and Brulon Soares underscore inclusivity in museums, emphasising the necessity for museums to be welcoming to all, accommodating visitors' circumstances, specific needs, and diverse perspectives. This approach highlights the role of museums as accessible and inclusive spaces for people worldwide.

However, in India, the British museum model was inherited without considering the country's unique social, cultural, and economic context. Consequently, museums were established without meaningful engagement with the Indian public, who were often treated as passive recipients. Research indicates that a large portion of the Indian population is still unaware of the true essence and relevance of museums, resulting in fewer visits compared to other historic or non-formal educational spaces. For many, museums are still perceived as elite institutions that feel difficult to relate to or engage with (Venugopal, 2014). Additionally, many mistakenly believe that museums are solely related to history or ancient artifacts and fail to grasp the purpose and diversity of museum collections, often viewing them merely as places for housing old, rare, and exotic objects.

Like museums worldwide, Indian museums are evolving in their roles and functions. Despite this transformation, challenges persist in defining their purpose and refining their operational practices. In India, museums hold immense potential as educational tools within its diverse, multicultural, and multilingual society, with their collection playing a key role in bridging cultural, social, and linguistic barriers. Their role as educational resources is particularly vital in India, where their impact surpasses that of museums in other parts of the world. Museums, as vital repositories of knowledge, play an important role—especially since most are government-run institutions in India. (Venugopal, 2014). Moreover, the inclusion of museums in the State List in the Seventh Schedule[2] of the Constitution of India highlights their significance as institutions of national importance.

India, a vast country spanning 3,287,263 km² with an estimated population of 1.39 billion in 2021[3] (up from 1.21 billion in the 2011 census), has around 1,200 museums (Seth & Sadiya 2023). These museums are not distributed rationally to serve the needs of the geographically diverse population, with some states having many museums, while others have only a few or just one or two. Despite the majority of the population living in rural areas, a significant proportion of museums are located in urban and semi-urban regions. This distribution implies that museums are limited and inadequately

[1] A museum is a not-for-profit, permanent institution in the service of society that researches, collects, conserves, interprets and exhibits tangible and intangible heritage. Open to the public, accessible and inclusive, museums foster diversity and sustainability. They operate and communicate ethically, professionally and with the participation of communities, offering varied experiences for education, enjoyment, reflection and knowledge sharing. (Adopted in the Extraordinary General Assembly of ICOM in Prague, on 24 August 2022)

[2] "Libraries, museums and other similar institutions controlled or financed by the State ... of national importance", Seventh Schedule (Article 246), List II-State List, Point 12

[3] United Nations Statistics Division Data. Accessed June 9, 2024. https://data.un.org/en/iso/in.html

positioned to serve the diverse needs of a society spread across vast geographical areas, from city centers to remote regions. In many states and cities in India, even where museums are numerous, they remain under-visited due to inaccessibility, lack of awareness, or lack of interest. In this context, outreach initiatives become especially crucial, as museums are often inaccessible to many visitors, and many museums go under-visited due to a lack of awareness about their relevance and potential role in cultural education. These initiatives play a vital role in addressing barriers such as uneven distribution, inaccessibility, and limited public understanding, helping museums connect with and engage a wide range of audiences across the country. A tailored strategy is essential to bridging the gap between museums and society, ensuring greater accessibility, awareness, and meaningful engagement.

II. CONNECTING MUSEUMS AND SOCIETY: AN ACTION RESEARCH ON SOCIAL INCLUSION AND OUTREACH IN INDIA

As part of the department's mandate, the author, an Assistant Professor in the Department of Museology at the Indian Institute of Heritage, is conducting an action research project on Museum Education. This project focuses on Museum Outreach initiatives and the Creation of Museum Educational Resources to enhance accessibility and engagment. The primary aim is to turn non-visitors into regular museum-goers and encourage their active participation in museums. It is envisaged that by exploring museums, the target audience will gain a deeper understanding of their cultural heritage, its resonance in contemporary times, and its significance for their future. Furthermore, the project seeks to foster a strong connection between museums and society, enhancing the community's appreciation of its cultural identity.

This initiative addresses key issues in Museum Education and Museology in India, aiming to create pilot programmes and models for museum professionals, provide academic resources for academicians, train Museology students on practically conducting outreach projects, and explore methods to make Indian museums more accessible and inclusive, considering the diverse learning needs of the audience. Indian society's heterogeneity and segmentation across social, cultural, economic, educational, regional, and geographical contexts require tailored educational approaches. The project champions the belief that everyone has the right to cultural education, cultural life, and heritage.Accordingly, this action research project has been conceptualised and categorised according to the diverse needs of its audiences. The project is being executed in three areas as follows:

2.1 Museum Outreach

The project aims to explore museums with audiences who have never visited museums before, particularly targeting students, to increase the utilisation of museums as educational resources among non-visitors. It also seeks to discover innovative approaches of museum outreach and accessibility, extending museum experiences to those who do not come or can't come for various reasons. Sensory/tactile educational kits are conceptualised and designed for this.

The purpose of the program is to popularize museums and generate enough interest to encourage people to visit these institutions. These programs inform potential museum visitors about what museums are, what they offer, why visiting them is beneficial, and how a museum visit can enrich their experience.

- *Outreach to Villages:* As part of the program, the author organized educational workshops on diverse themes such as arts and crafts of India, museum collections, and building memories and connections with objects for rural school students and communities who have never visited museums or cannot access museum services.

– *Outreach to Hospitals:* This program aimed to explore how museums can serve as therapeutic tools for patients, particularly children and their families. As part of this initiative, tailor-made educational workshops were conceptualized and several educational programs and kits were developed for pediatric patients in the critically ill category at one of India's most prominent public hospitals, the All India Institute of Medical Sciences, New Delhi.

2.2 Educational programmes for Special Children

Under this programme, the author conceptualised and conducted tailor-made educational programmes for special children like visually impaired, mentally challenged and marginalised children keeping in consideration their individual needs and expectations.

2.3 Creation of Museum Educational Resources for Students and Educators

As a part of this programme research has been conducted to explore the educational potential of museums and developed non-formal educational resources tailored for various audiences. This includes educational booklets based on museum collections, non-formal learning aids, and customized educational programs. Discovery Boxes have been designed on diverse themes featuring replicas of museum objects. Educational Handbooks have been created to enhance classroom lessons and assist teachers in delivering curriculum content in an engaging manner.

Some of the educational booklets include:

- 'Through the Museum Lens' (in English) and 'Sanghralaye ke Jharoke Se' (in Hindi) focusing on the ancient civilization of India centring around the collection of Indus Valley Civilization collection of the National Museum, New Delhi
- 'Museum Safari' bilingual booklets (English and Hindi) on environmental conservation featuring natural history collection of the State Museum, Lucknow
- 'Aao Chalen Sanghralaye ki Aur'- (Let's visit the museum) introducing the collection of the National Museum, New Delhi
- 'Gandhi For All' highlighting Mahatma Gandhi's principles through the collection at the National Gandhi Museum, New Delhi. These booklets are available in Hindi, English, Urdu, Bengali, Ladakhi, Assamese, and include a Braille edition.

III. MUSEUM OUTREACH: A SELECT EXAMPLE

This section delves into the approach, methodology, execution, and impact of the action research project "Museum Outreach Initiatives and the Creation of Museum Educational Resources", being conducted by the author. As part of the project, a series of workshops titled "Gandhi for All", were designed for diverse Indian audiences across various regions of India. The case study reflects the initiatives in conceptualizing, designing, executing, and assessing audience response and impact for museum outreach programme. It highlights the attempts to understand the varied needs of diverse Indian audiences and to create tailored educational resources and workshop models.

***Theme: 'Gandhi for All' workshop series*:** The series of outreach educational workshops titled 'Gandhi for All' was conducted across India as part of the celebration of the 150th Birth Anniversary of Mahatma Gandhi for diverse audiences. As part of the project, educational resources were conceptualized and designed, portraying the collection of the National Gandhi Museum, New Delhi

The workshop series aimed to convey Mahatma Gandhi's ideas, philosophy, life history, and cultural legacy by bringing symbolic objects associated with him to students and communities across India. This outreach initiative focused on ensuring that Gandhi's cultural heritage, represented by these

objects, reached people who were geographically distant or unable to visit traditional museum spaces. Through engaging and clear presentations, the workshops encouraged reflection on Gandhi's teachings and inspired participants to integrate them into their own lives and perspectives, while also examining how these teachings remained relevant in today's world. Each workshop aimed to ensure that the cultural heritage of Mahatma Gandhi embodied in objects associated with him, made accessible to those who were geographically distant or unable to attend for various reasons.

Approach: In India, there are several museums dedicated to Mahatma Gandhi's teachings, including two in Delhi: Gandhi Smriti Darshan and National Gandhi Museum at Rajghat. For this, replicas from the National Gandhi Museum were used. In numerous workshops within the series, students from the Department of Museology at IIH were engaged and trained in conceptualizing and executing customized museum educational programs tailored to meet the needs and expectations of the target audience.

Target audience: These workshops were conducted for a wide range of audiences, including young children, young adults, artisans, and marginalized groups such as critically ill pediatric patients, children from nomadic villages, rural communities, rural school students, monastery school students, madarsa students, and those with special needs such as mental and visual challenges, as well as university students, totaling over 500 participants.

Regions reached out: The programme was conducted in different parts of India covering eight states and union territories through fifteen workshops conducted over a span of a year. The workshops series conducted across India were tailor-made and diversified in terms of the scope of both their form and content to suit the requirements of the target audience of the various regions.

The key components of the workshop series were:

- *'Gandhi for All' Message:* Emphasizing that everyone, as individuals and communities, possesses qualities that resonate with Gandhiji's principles and philosophy and can carry his legacy forward.
- *Discovery box (Custom-made trunk containing replica objects of Gandhiji):* A special custom-made trunk filled with symbolic items (replica objects) representing Gandhiji's life was designed to help people understand his legacy through museum lens.

- *Photographic Exhibition:* Featuring photographs and audio-visual content depicting significant events and figures from Gandhi's life.
- *Tailor-Made Interactive Activities:* were designed for each workshop, considering the target audience's regional, special, educational, social, and cultural needs.
- *Activity-Based Educational Booklet:* Designed specifically for the workshop series, presenting Gandhiji's story through museum objects**.** Available in multiple languages with a Braille edition includes anecdotes, stories, skits, and interactive games to convey Gandhiji's message with simplicity and ethical depth.

Demonstrating the use of the Educational Booklet

Impact Assessment of the workshop series:

1. The workshop series made an effort to connect with individuals who had either limited or no access to museums.
2. It established a model for utilizing museum objects to raise awareness about the cultural legacy and philosophy of Mahatma Gandhi through museum lens.
3. It triggered a chain reaction as the trunks, booklets and other props left at the respective workshop venues were used for reaching out to many more students, teachers, and other individuals.
4. The cultural legacy of Gandhiji, collected and displayed in museums, reached various corners of the country.

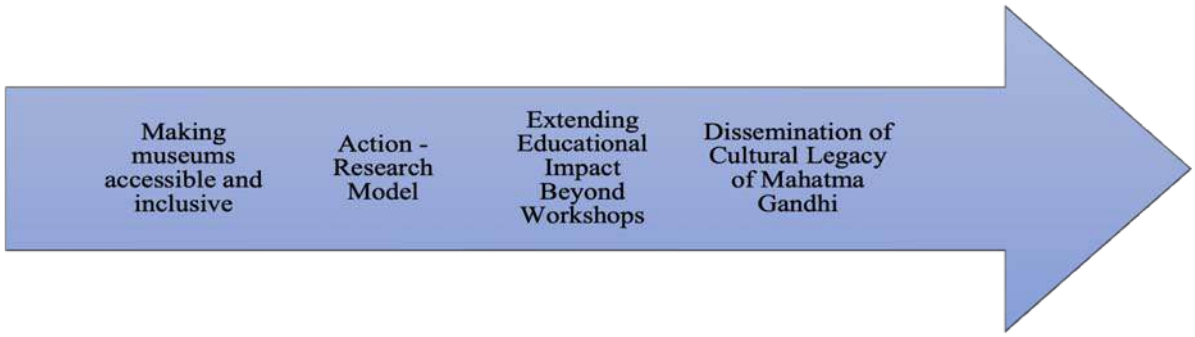

Reflections on tailor-made resources designed for diverse workshops participants:

This section provides insights about custom-designed educational materials that were created specifically for participants in various workshops. It intends to explain the thought process, considerations, and effectiveness of these tailored resources in meeting the diverse needs of the workshop participants.

- *For Students With Special Needs (Visually Impaired And Mentally Challenged Students)*

Two specialised workshops were conducted for students with special needs: one for visually impaired students and another for mentally challenged students. These workshops employed creative and customized tools to ensure that Gandhiji's message and legacy resonated deeply with the participants, aiming to make information and knowledge accessible to children with disabilities, as emphasized by the UN Convention on the Rights of Persons with Disabilities. By asking questions and gathering feedback on the stories, objects, and activities, the students remained actively engaged and interested throughout the process.

- *Workshop for Visually Impaired Student:* The workshop for visually impaired students focused on tactile experiences and verbal communication to convey Gandhiji's ideas and philosophy. The tactile sensation of objects was crucial, with even the trunk featuring three-dimensional embossing to allow students to touch and feel its various features. These students had the opportunity to touch and feel replicas of museum objects, a rare experience not typically available in museums.

  The students were given clay to create tactile models of Gandhi's objects based on their tactile experiences. This activity was greatly enjoyed by the students. A unique feature of the workshop was a Braille booklet that not only documented the references and stories discussed during the sessions but also narrated the story using museum objects.

Tactile exhibition prepared for visually impaired school students


Visually impaired students exploring tactile objects of the discovery trunk


Visually impaired exploring tactile paintings

Students molding tactile models of Gandhi's objects


Sensory experience through props

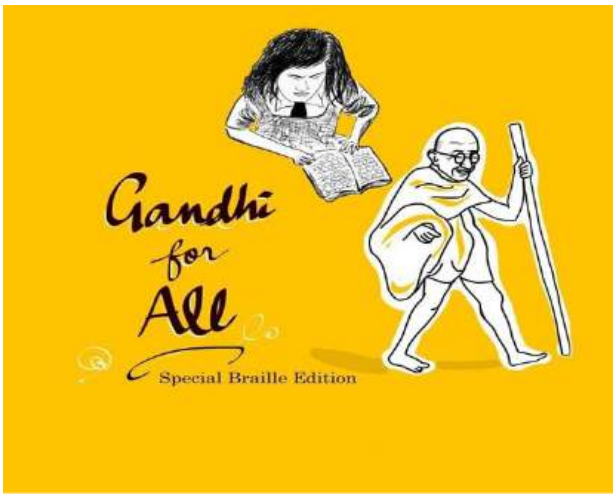

Cover of Braille addition of the Booklet

Students exploring tactile images in the braille edition

- *Workshop for Mentally Challenged Students*

In the workshop for mentally challenged students, interactive games and sensory experiences were used to convey Gandhiji's ideas. These activities simplified complex topics like honesty, discipline, equality, discrimination, and integrity, making them easier to understand and engage with. Hands-on activities, such as creating clay models, helped students connect with the material in a tangible way, enhancing their grasp of Gandhi's message and legacy. This approach not only reinforced their learning but also made the experience enjoyable and meaningful.

Storytelling through images and tactile objects

Enjoying hands-on experience of the replicas

- *For Pediatric Patients, The Workshop Served As A Therapeutic Tool*

The workshop was held for critically ill pediatric patients at the All India Institute of Medical Sciences, a prominent public hospital in India. Through animated skits, the life and principles of Gandhiji were shared in an engaging manner. The children participated enthusiastically in activities such as exploring replica objects, clay modeling, and paper crafting. Interestingly, many were so engrossed in the workshop that they momentarily forgot their pain and they got a chance to express their emotions, feelings and creativity through artistic expressions. For most of these children and their parents, it was their first introduction to museums, sparking a newfound interest in visiting them. The workshop was deeply enjoyed and served as a therapeutic experience for the young patients.

Storytelling through skit

Children immersed in clay modeling activity

Children enjoying hands-on experience of the replicas

- *Glimpses Of Some Engaging Activities Conducted For Students From Various Schools Including Monastery School, Madarsa, Rural Schools Including Rural Communities*

Madarsa students engrossed in reading bookletA rural school student learning the skill of spinning, embodying Gandhi's philosophy of self-reliance

Women from the rural community demonstrating weaving, embodying Gandhi's philosophy of self-reliance

- *Personifying Principles of Gandhiji Through Their Visual, Written and Verbal Expressions*

This process utilizes various forms of expression—such as visual arts, writing, and speech—to internalize and convey Mahatma Gandhi's values and teachings. The conducted workshops made these principles relatable and tangible, encouraging individuals to personally understand and reflect on Gandhiji's philosophy in a meaningful and impactful manner.

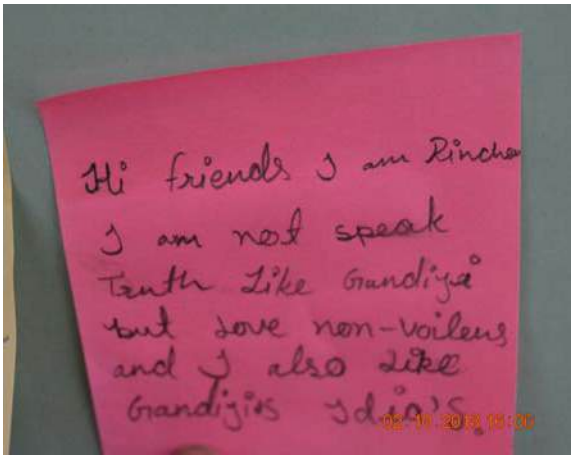

The outreach initiatives under the action research project, conceptualized and designed by the Department of Museology, Indian Institute of Heritage, represent a successful endeavor in enhancing museum accessibility and inclusivity within India's constantly evolving social and cultural landscape. This initiative sparked newfound interest among individuals who had not previously visited museums, transforming them into regular museum-goers and encouraging their active participation in museum activities. It has achieved its objectives of creating pilots and models for museum professionals, providing valuable academic resources for academicians, offering practical training to Museology students in conducting outreach projects, and exploring innovative methods to enhance the accessibility and inclusivity of Indian museums tailored to diverse audiences. These efforts signify significant progress towards fostering a more dynamic and engaging museum environment that embraces cultural diversity and enhances social inclusion.

REFERENCES

1. Bonilla-Merchav, L. and Bruno Brulon Soares. 2022. “Arriving at the Current Museum Definition: A Global Task and a Decentralising Exercise.” *Museum International*, 74:3-4, 134-147.
2. ICOM. 2022. Museum Definition. Accessed on June 5, 2024. https://icom.museum/en resources/standards-guidelines/museum-definition/
3. Seth, Manvi and Juhi Sadiya. 2023. *Directory of Museums in India*. Manak Publication
4. Venugopal, B. 2014. “Re-Imagine Museums and Galleries: UK-India Opportunities and Partnerships.” British Council. 65-66. Accessed June 10, 2024. https://www.britishcouncil.in/ sites/default/files/re-imagine_museums_india-uk.pdf